SAND REPORT
SAND2001-3984
Unlimited Release
Printed May 2002

Improved Materials Aging Diagonostics and Mechanics through 2D Hyper-spectral Imaging Methods and Algorithms

David, M. Haaland, Christine M. Wehlburg, Laura E. Martin, Mark H. Van Benthem, Michael R. Keenan, David K. Melgaard, Edward V. Thomas, Fredrick W. Koehler IV, Mathias Celina

Prepared by
Sandia National Laboratories
Albuquerque, New Mexico 87185 and Livermore, California 94550

Sandia is a multiprogram laboratory operated by Sandia Corporation, a Lockheed Martin Company, for the United States Department of Energy under Contract DE-AC04-94AL85000.

Sandia National Laboratories

Issued by Sandia National Laboratories, operated for the United States Department of Energy by Sandia Corporation.

Available to DOE and DOE contractors from
U.S. Department of Energy
Office of Scientific and Technical Information
P.O. Box 62
Oak Ridge, TN 37831

Telephone: (865)576-8401
Facsimile: (865)576-5728
E-Mail: reports@adonis.osti.gov
Online ordering: http://www.doe.gov/bridge

Available to the public from
U.S. Department of Commerce
National Technical Information Service
5285 Port Royal Rd
Springfield, VA 22161

Telephone: (800)553-6847
Facsimile: (703)605-6900
E-Mail: orders@ntis.fedworld.gov
Online order: http://www.ntis.gov/ordering.htm

SAND2001-3984
Unlimited Release
Printed May 2002

Improved Materials Aging Diagnostics and Mechanisms through 2D Hyperspectral Imaging Methods and Algorithms

David M. Haaland, Christine M. Wehlburg, Laura E. Martin,
Mark H. Van Benthem, and Michael R. Keenan
Information Detection, Extraction, and Analysis

David K. Melgaard
Tribology, Mechanics, and Melting

Edward V. Thomas
Individual Survey Assessment and Statistics

Sandia National Laboratories
P.O. Box 5800
Albuquerque, New Mexico 87185-0886

Fredrick W. Koehler IV
Spectral Dimensions
Olney, MD

Mathias Celina
Queensland University of Technology
Brisbane, Australia

Abstract

The availability of new commercial hyperspectral imaging infrared spectrometers makes possible the quantitative analysis of materials without the need for standards. In the course of achieving this goal, we have developed a new family of augmented classical least-squares (ACLS) algorithms that have important improvements over other quantitative multivariate calibration methods. The new ACLS methods are described and their application to hyperspectral image analysis is presented. Demonstration is given for the use of ACLS methods to improve the quantitative analysis of hyperspectral image data when chromatic aberrations are present in the system. A comparison of several multivariate curve resolution methods to estimate pure-component spectra without standards is presented. Finally, improvements to the multivariate curve resolution methods used to perform quantitative spectral analysis without standards are also presented. This report is a compilation of unpublished works describing these methods. Along with reference published and accepted journal papers, this body of work demonstrates the successful completion of the goals of this project.

Contents

INTRODUCTION

In this three-year research project, we set out to develop new methods of analysis of two-dimensional hyperspectral Fourier transform infrared (FT-IR) images collected from a new generation of commercial FT-IR imaging spectrometers. The goal was to develop and apply new hyperspectral image analysis methods to the investigation of the aging of polymeric materials. We have accomplished this goal and have developed a whole new family of multivariate calibration methods that significantly improve the qualitative and quantitative analysis of spectral data whether the data are from hyperspectral images or from other sources. This report is a compilation of appendices from journal preprints, a patent specification, and another report that were all generated in part or in whole from this Laboratory Directed Research and Development (LDRD) project. Patent applications, published journal papers, and submitted journal papers related to this project are referenced but not included in this report.

Because hyperspectral image data were not available at the beginning of this project, we initiated the development of a new classical least squares/ partial least squares (CLS/PLS) hybrid multivariate analysis algorithm that was to create the basis of our hyperspectral image analyses. This hybrid algorithm was developed and programmed into several software codes. Celeste Drewien documented the implementation of the CLS/PLS hybrid algorithm for parallel processing computers.[1] The theory of the hybrid algorithm and an application to updating multivariate calibration models for the presence of unmodeled sources of near-infrared spectral variation in dilute aqueous solutions has also been published.[2]

In the course of developing the hybrid algorithm, a significant improvement to the original CLS multivariate analysis algorithm[3-5] was developed. The improvement was called prediction-augmented classical least squares (PACLS). The theory and application of the new PACLS algorithm to updating CLS models for new sources of unmodeled spectral variation in the unknown samples has also been published.[6]

The concept of the PACLS algorithm was then further extended to a whole family of generalized multivariate augmented classical least squares (ACLS) methods.[7] Among these algorithms are the concentration-residual augmented CLS (CRACLS) algorithm,[8] spectral-residual augmented CLS (SRACLS), and the scores augmented CLS (SACLS) algorithm. The new augmented methods and the hybrid algorithm have been the subject of two patent applications[9, 10] and two provisional patent applications.[11] The advantage of these new algorithms lies in their ability to rapidly update multivariate calibration models for the presence of unmodeled sources of spectral variation, e.g., for unmodeled chemical species, spectrometer drift, or changes in the spectra due to changes in spectrometers.

The addition of the PACLS method to the hybrid algorithm (PACLS/CLS) has been demonstrated to be effective for converting a constant temperature calibration model into one that corrects for temperature variations in dilute aqueous solutions,[2] for maintaining a calibration in the presence of significant instrument drift,[12] and for transferring quantitative calibrations between spectrometers.[13]

The CRACLS algorithm has also been demonstrated to have comparable prediction ability as the more common partial least squares (PLS) method. However, it has also been demonstrated to achieve greater qualitative information from the calibration data and to rapidly

update the calibration during prediction to maintain calibrations in the presence of significant spectrometer drift for the dilute aqueous solution system. The theoretical development of the CRACLS algorithm and the demonstration of its ability to maintain the calibration in the presence of severe instrument drift has been documented in a paper recently accepted for publication.[8]

A description of all the generalized augmented methods is presented in Appendix A of this report. A portion of this Appendix along with a demonstration of the SRACLS algorithm to rapidly update the calibration when different spectrometers are used in the collection of the unknown samples is presented in a paper that has recently been accepted for publication in Vibrational Spectroscopy.[7]

Appendix B of this report documents the hyperspectral infrared analysis of ink jet printer inks using end-member analysis from commercial software and compares these commercial software results to those obtained from the use of the PACLS algorithm. The PACLS algorithm is shown in Appendix B to be able to correct the quantitative analysis of the ink image spectra for the presence of chromatic aberration in the data. This Appendix serves the basis of a paper to be submitted to Applied Spectroscopy.

Appendix C compares a variety of multivariate curve resolution techniques applied to the quantitative analysis of an aged neoprene polymer sample without the use of calibration standards. It compares SIMPLISMA, constrained alternating least squares, and an errors-in-variables approach to MCR.

Appendix D documents the development of new approaches in the application of equality constraints in the application of multivariate curve resolution (MCR) methods that form the basis of the methods used for performing quantitative analysis of hyperspectral images without the use of calibration standards. The implementation of equality constraints is important for using the augmented CLS methods in quantitative hyperspectral image analysis. A separate report has been prepared that demonstrates the use of MCR with non-negativity and equality constraints to perform quantitative analysis of hyperspectral images of aged neoprene without the use of calibration standards.[14] The ACLS methods in combination with equality constraints added to the MCR analysis demonstrate dramatic improvements in estimating the pure-component spectra and in generating concentration maps of the images for each chemical component present in the image data when significant instrument artifacts contaminate the hyperspectral image data.

This report demonstrates the successful completion of the original goals of our LDRD project. The unanticipated development of an entire family of new calibration algorithms that have high commercial value both in the analysis of hyperspectral images as well as in the analysis of any quantitative spectral data has make the significance of this research far beyond the original goals of the project.

CONCLUSIONS

The publications, submitted publications, and patent applications that arose from this three-year project represent new capabilities in the area of qualitative and quantitative multivariate spectral calibration. The new ACLS and hybrid algorithms represent a family of multivariate calibration algorithms that can be rapidly updated during prediction to accommodate unmodeled sources of spectral variation such as unmodeled chemical species, spectrometer drift, or changes in spectrometers. These new methods have extensive use in the quantitative analysis of hyperspectral image data also. We have demonstrated that the new ACLS methods allows quantitative analysis of infrared spectral image data even when severe chromatic aberrations are present in the system. The general usefulness of these new algorithms has been demonstrated by the successful licensing of the related patents to Thermo Nicolet for use in vibrational spectroscopy.

Multivariate curve resolution methods have been employed to accomplish the quantitative analysis of hyperspectral image data without standards. The standard non-negativity constrained alternating least squares MCR methods have been improved significantly with the implementation of ACLS features in the alternating least squares concept. The incorporation of the ACLS methods have been incorporated into the MCR methods with the use of improved equality constraints added to the alternating least squares iterative procedure. Although these methods have been demonstrated with infrared image data, their application can be extended far beyond this single area of research. The continued and further development of these methods continues with other projects in the areas of remote sensing, kinetic analysis, and the general improvement of quantitative spectral analysis.

REFERENCES

1. Drewien, C., *A parallel prediction-augmented classical least squares/partial least squares hybrid algorithm : CPLS 1.0 code*. 2000, Sandia National Laboratories: Albuquerque.
2. Haaland, D.M. and D.K. Melgaard, *New classical least-squares/partial least-squares hybrid algorithm for spectral analyses.* Applied Spectroscopy, 2001. **55**(1): p. 1-8.
3. Haaland, D.M. and R.G. Easterling, *Improved Sensitivity of Infrared-Spectroscopy by the Application of Least-Squares Methods.* Applied Spectroscopy, 1980. **34**(5): p. 539-548.
4. Haaland, D.M. and R.G. Easterling, *Application of new least-squares methods for the quantitative infrared analysis of multicomponent samples.* Applied Spectroscopy, 1982. **36**(2): p. 665-673.
5. Haaland, D.M., R.G. Easterling, and D.A. Vopicka, *Multivariate Least-Squares Methods Applied to the Quantitative Spectral-Analysis of Multicomponent Samples.* Applied Spectroscopy, 1985. **39**(1): p. 73-83.
6. Haaland, D.M. and D.K. Melgaard, *New prediction-augmented classical least-squares (PACLS) methods: Application to unmodeled interferents.* Applied Spectroscopy, 2000. **54**(9): p. 1303-1312.
7. Haaland, D.M. and D.K. Melgaard, *New Augmented Classical Least Squares Methods for Improved Quantitative Spectral Analyses.* Vibrational Spectroscopy, 2001: p. In Press.
8. Melgaard, D.K., D.M. Haaland, and C.M. Wehlburg, *Concentration Residual Augmented Classical Least Squares (CRACLS): A Multivariate Calibration Method with Advantages over Partial Least Squares.* Applied Spectroscopy, 2001: p. In Press.
9. Haaland, D.M., *Improved Classical Least Squares Multivariate Spectral Analysis*. 2001, Sandia National Laboratories: U.S.A. p. Submitted Patent Application.
10. Haaland, D.M., *Hybrid Least Squares Multivariate Spectral Analysis Methods*. 2001, Sandia National Laboratories: U.S.A. p. Submitted Patent Application, SD6256.
11. Haaland, D.M. and D.K. Melgaard, *A Method of Multivariate Spectral Analysis*. 2001, Sandia National Laboratories: U.S.A. p. Submitted Provisional Application, SD6689.
12. Wehlburg, C.M., et al., *New Techniques for Maintaining Multivariate Quantitative Calibrations of a Near-Infrared Spectrometer.* Applied Spectroscopy, 2001: p. In Press.
13. Wehlburg, C.M., D.M. Haaland, and D.K. Melgaard, *New Hybrid Algorithm for Transferring Intra-Instrument Multivariate Quantitative Calibrations of a Near-Infrared Spectrometer.* Applied Spectroscopy, 2001: p. Submitted.
14. Haaland, D.M., F.W. Koehler IV, and M.H. Van Benthem, *Reducing System Artifacts in Hyperspectral Image Data Analysis with the Use of Estimates of the Error Covariance in the Data*. 2001, Sandia National Laboratories: Albuquerque. p. In Preparation.

Appendix A.

Generalized Augmented Classical Least Squares Methods

David Haaland and David Melgaard
Sandia National Laboratories
Albuquerque, New Mexico 87185-0886

The prediction-augmented classical least squares (PACLS) algorithm [1] provides a basis for rapidly updating a classical least squares (CLS) model [2-4] during prediction of component values of the target unknown sample. PACLS allows models to be updated for the presence of spectrometer drift, changes in spectrometer parts or changes in whole spectrometers, unmodeled chemical or non-chemical spectral components, as well as updating for more generalized changes such as changes in starting materials, the presence of nonlinearities, chromatic aberrations, or stray light, etc. However, the PACLS algorithm is limited by the fact that accurate predictions require all interfering spectral components (including chemical and non-chemical sources of spectral variation) to be explicitly included in the calibration. Alternatively, if one or more spectral interferences were left out of the calibration, then their spectral influence would have to be added during prediction of the unknown sample to correct for their absence in the model. These limitations can be reduced and even eliminated by the development of a new generalized family of algorithms that we call augmented classical least squares (ACLS).[5] This family of algorithms includes one method that has been previously published by Martens and Naes,[6] which they call the extended Beer's law model. The other members of the ACLS family have not been previously published or disclosed. When the new ACLS methods are combined with our proprietary PACLS algorithm, we have a powerful set of new multivariate capabilities such that analyses can be performed with incomplete knowledge of interferences in the calibration data. Thus, the ACLS methods can be used even if an incomplete set of component values is known during the calibration step. The augmented methods can yield accurate predictions even in the presence of unknown sources of spectral variation, nonlinear responses, and non-uniform and correlated errors. Yet, the new algorithm can still use the PACLS capabilities to rapidly update the model during prediction to accommodate unmodeled sources of spectral variation in the unknown sample spectra to be predicted. Below is given the broad ACLS algorithm and specific examples of its implementation.

The standard CLS model is

$$\mathbf{A} = \mathbf{CK} + \mathbf{E_A} \qquad (1)$$

where $\mathbf{A}$ is the set of n objects (e.g., sample spectra) each consisting of p responses, $\mathbf{C}$ is the set of reference values for the n objects with m unique components, $\mathbf{K}$ is the set of p reference responses for the m unique components, and $\mathbf{E_A}$ is the $n \times p$ set of errors and noise not fit by the model. For an incompletely specified and/or nonlinear model, the error matrix $\mathbf{E_A}$ will consist of a set of correlated, non-uniform errors that can be further decomposed into a sum of correlated errors due to unmodeled spectral components, nonlinearities, or system-related correlated errors and uncorrelated random errors

representing system noise and/or spectral variation that is not relevant to prediction. Factor analysis methods can be applied to $\mathbf{E_A}$ to separate these error sources. Thus, $\mathbf{E_A}$ can be described as:

$$\mathbf{E_A} = \mathbf{TP} + \mathbf{E} \quad (2)$$

where **T** and **P** are the set of n x r scores and r x p loading vectors, respectively, obtained from the factor analysis of $\mathbf{E_A}$, and **E** is the set of n x p random errors and spectral variations not useful for prediction. The dimension r is the rank of the $\mathbf{E_A}$ matrix or the number of factors that are required for optimal prediction. Therefore, Eq. 1 can be written

$$\mathbf{A} = \mathbf{CK} + \mathbf{TP} + \mathbf{E} \quad (3)$$

$\mathbf{E_A}$ can be determined from the CLS estimated **K** matrix, i.e.,

$$\mathbf{E_A} = \mathbf{A} - \mathbf{C}\hat{\mathbf{K}} \quad (4)$$

where $\hat{\mathbf{K}}$ is the CLS estimated response of the known pure components. A CLS solution for $\hat{\mathbf{K}}$ can be obtained from

$$\hat{\mathbf{K}} = (\mathbf{C}^T\mathbf{C})^{-1}\mathbf{C}^T\mathbf{A} \approx \mathbf{C}^+\mathbf{A} \quad (5)$$

where C^+ is the generalized inverse. The approximately equals sign is appropriate if only selected factors are used in the generalized inverse. An equals sign would be appropriate for the right-hand side of Eq. (5) if all factors of the generalized inverse are used in the solution.

The rows of the $\hat{\mathbf{K}}$ matrix in Eq. (5) can be augmented directly with all or selected spectral residuals from Eq. (4) to correct the CLS model for unmodeled spectral components. The augmented $\hat{\mathbf{K}}$ matrix can then be used in the augmented CLS prediction step to solve for an augmented C matrix (called $\tilde{\mathbf{C}}$, where the ~ symbol indicates an augmented matrix). The augmented CLS prediction estimate $\hat{\tilde{\mathbf{C}}}$ can be obtained from

$$\hat{\tilde{\mathbf{C}}} = \mathbf{A}\tilde{\hat{\mathbf{K}}}(\tilde{\hat{\mathbf{K}}}\tilde{\hat{\mathbf{K}}}^T)^{-1} \approx \mathbf{A}\tilde{\hat{\mathbf{K}}}^+ \quad (6)$$

Alternatively, Eq. (2) can be factor analyzed by any factor analysis method. Common methods include principal component analysis (PCA), partial least squares (PLS), or principal component regression (PCR). If PLS or PCR are used, then concentration residuals must be included in the calibration process, and the method becomes one of the hybrid method described in SD6256.[7] The factor analysis can use either an orthogonal factor analysis method or any non-orthogonal factor analysis method. Once the factor analysis is completed, the scores, **T,** or the loadings, **P,** can be used to improve the CLS calibration model. If PCA is used as the factor analysis method applied to the calibration spectral residuals, then the eigenvectors, **P** (i.e., the rows of **P**), can augment the rows of the $\hat{\mathbf{K}}$ matrix during the CLS prediction step to improve the prediction ability of the CLS model. The augmented CLS solution for component values then proceeds according to Eq. (6). This procedure represents the extended Beer's law model method previously described by Martens and Naes.[6] We prefer to call this algorithm spectral-residual augmented classical least squares (SRACLS) to differentiate it from other augmented CLS methods. When combined with PACLS augmented by spectral responses obtained from data or information that is independent of the calibration data set, the SRACLS

algorithm can be updated in a PACLS prediction step (see SD6227[8]) for the presence of unmodeled changes in the responses of the prediction samples.

We can also use the scores **T** to correct the CLS model for unknown components. In this case, the columns of **T** can be added to **C** to augment the column dimension of **C**. Recalibrating with this augmented CLS method as in Eq. (7) results in an augmented $\hat{\tilde{\mathbf{K}}}$ matrix that allows the augmented CLS model to have better predictive properties than the original CLS model.

$$\hat{\tilde{\mathbf{K}}} = (\tilde{\mathbf{C}}^{\mathrm{T}}\tilde{\mathbf{C}})^{-1}\tilde{\mathbf{C}}^{\mathrm{T}}\mathbf{A} \approx \tilde{\mathbf{C}}^{+}\mathbf{A} \qquad (7)$$

When augmentation makes use of scores, we call this method scores-augmented classical least squares (SACLS).

The process can be generalized further to augment the column dimension of **C** with selected calibration concentration residuals obtained from the predicted calibration reference values (see Eq. (8)) after CLS calibration and prediction or cross-validated prediction on the calibration samples or true prediction on a set of validation samples.

$$\mathbf{E}_{\mathbf{C}} = \hat{\mathbf{C}} - \mathbf{C} \qquad (8)$$

where $\mathbf{E}_{\mathbf{C}}$ represents the errors for the known component values (e.g., concentration values) after performing the CLS calibration and prediction steps. This method, which we call concentration-residual augmented classical least squares (CRACLS), develops new estimated responses that are then included as new rows of $\hat{\mathbf{K}}$ in an augmented CLS prediction. CRACLS is an iterative method that adds one column of concentration residuals (arbitrarily selected from the errors of one of the components included in the calibration) during each iteration that then generates new residuals to be added to the first augmented $\hat{\tilde{\mathbf{C}}}$ matrix.[9] New component value residuals are then generated and used in a second iteration step. The process is continued until all factors required for optimal prediction are added. In all augmented CLS methods, the optimal number of factors can be determined using the same method for PLS factor selection that has been previously published for PLS and PCR[10]. The component value residuals in this method can be generated from the either the full models or the cross-validated models.

Further generalizing the method, the **C** matrix can be augmented by one or more columns of random numbers to form another augmented CLS method. Random numbers can also be added to augment the $\hat{\mathbf{K}}$ matrix to improve the prediction ability of CLS. In general, any set of vectors of the correct dimension for **T** or **P** can be used to improve the CLS model as long as they each contain some independent information relative to themselves, the original **C** matrix, or initially estimated $\hat{\mathbf{K}}$ matrix, i.e., they cannot be collinear with each other, **C**, or $\hat{\mathbf{K}}$.

The fact that the new augmented CLS methods can be performed either during calibration (augmenting with scores) or during prediction (augmenting with loading vectors) gives us the opportunity to greatly improve the alternating least squares (ALS) multivariate curve resolution (MCR) method for decomposing a series of spectra into their pure-component spectra and concentrations.[11-15] MCR methods are extremely valuable for quantitative

multi-spectral and hyperspectral image analysis, kinetics studies, or any problem where quantitative results are desired when there are no standards or inadequate knowledge of the pure-component spectra or component concentrations. Most often alternating least squares MCR is performed with constraints applied. For example, constraints that have been applied in the literature are non-negativity, closure, unimodality, baseline constraints, etc. For any alternating least-squares multivariate curve resolution method, we can augment the calibration and prediction least-squares steps with information that we want the least-squares fits to ignore, e.g., known or estimated spectral components or any estimate of the error covariance of the system. An estimate of the error covariance can be obtained for example by taking repeat spectra or in the case of spectral imaging, repeat spectral images. Each least-squares calibration step in MCR iteration is augmented by the scores obtained from the factor analysis of the error covariance matrix and each least-squares prediction step is augmented by the loading vectors from the same matrix. Any constraints are applied only to the non-augmented portion of the augmented matrices. In this manner, quantitative analysis of spectral images can proceed without the need for standards even in the presence of large error covariance structure in the data. An example of this new method applied to hyperspectral infrared image analysis without standards is presented in a related report.[16]

REFERENCES

1. Haaland, D.M. and D.K. Melgaard, *New prediction-augmented classical least-squares (PACLS) methods: Application to unmodeled interferents.* Applied Spectroscopy, 2000. **54**(9): p. 1303-1312.
2. Haaland, D.M. and R.G. Easterling, *Improved Sensitivity of Infrared-Spectroscopy by the Application of Least-Squares Methods.* Applied Spectroscopy, 1980. **34**(5): p. 539-548.
3. Haaland, D.M. and R.G. Easterling, *Application of New Least-Squares Methods for the Quantitative Infrared-Analysis of Multicomponent Samples.* Applied Spectroscopy, 1982. **36**(6): p. 665-673.
4. Haaland, D.M., R.G. Easterling, and D.A. Vopicka, *Multivariate Least-Squares Methods Applied to the Quantitative Spectral-Analysis of Multicomponent Samples.* Applied Spectroscopy, 1985. **39**(1): p. 73-83.
5. Haaland, D.M. and D.K. Melgaard, *New Augmented Classical Least Squares Methods for Improved Quantitative Spectral Analyses.* Vibrational Spectroscopy, 2001: p. In Press.
6. Martens, H. and T. Naes, *Multivariate Calibration.* 1989, Chichester: John Wiley & Sons.
7. Haaland, D.M., *Hybrid Least Squares Multivariate Spectral Analysis Methods.* 2001, Sandia National Laboratories: U.S.A. p. Submitted Patent Application, SD6256.
8. Haaland, D.M., *Improved Classical Least Squares Multivariate Spectral Analysis.* 2001, Sandia National Laboratories: U.S.A. p. Submitted Patent Application, SD6227.
9. Melgaard, D.K., D.M. Haaland, and C.M. Wehlburg, *Concentration Residual Augmented Classical Least Squares (CRACLS): A Multivariate Calibration Method with Advantages over Partial Least Squares.* Applied Spectroscopy, 2001: p. In Press.
10. Haaland, D.M. and E.V. Thomas, *Partial Least-Squares Methods for Spectral Analyses .1. Relation to Other Quantitative Calibration Methods and the Extraction of Qualitative Information.* Analytical Chemistry, 1988. **60**(11): p. 1193-1202.
11. Bro, R. and S. DeJong, *A fast non-negativity-constrained least squares algorithm.* Journal of Chemometrics, 1997. **11**(5): p. 393-401.
12. Tauler, R., B. Kowalski, and S. Fleming, *Multivariate Curve Resolution Applied to Spectral Data from Multiple Runs of an Industrial-Process.* Analytical Chemistry, 1993. **65**(15): p. 2040-2047.
13. Saurina, J., S. Hernandezcassou, and R. Tauler, *Multivariate Curve Resolution Applied to Continuous-Flow Spectrophotometric Titrations : Reaction between Amino-Acids and 1 ;2-Naphthoquinone-4-Sulfonic Acid.* Analytical Chemistry, 1995. **67**(20): p. 3722-3726.
14. Casassas, E., I. Marques, and R. Tauler, *Study of Acid-Base Properties of Fulvic-Acids Using Fluorescence Spectrometry and Multivariate Curve Resolution Methods.* Analytica Chimica Acta, 1995. **310**(3): p. 473-484.

15. Tauler, R., et al., *Application of a New Multivariate Curve Resolution Procedure to the Simultaneous Analysis of Several Spectroscopic Titrations of the Copper(Ii)-Polyinosinic Acid System.* Chemometrics and Intelligent Laboratory Systems, 1995. **27**(2): p. 163-174.
16. Haaland, D.M., F.W. Koehler IV, and M.H. Van Benthem, *Reducing System Artifacts in Hyperspectral Image Data Analysis with the Use of Estimates of the Error Covariance in the Data.* 2001, Sandia National Laboratories: Albuquerque. p. In Preparation.

APPENDIX B

Quantitative Analysis of Ink-jet Inks with an FT-IR Imaging Spectrometer

Frederick W. Koehler IV and David M. Haaland
Sandia National Laboratories
Albuquerque, New Mexico 87185-0086

INTRODUCTION

Fourier transform infrared (FT-IR) hyperspectral imaging is a recent development of increasing importance in the analysis of heterogeneous samples. First introduced in the analytical chemistry literature in 1995 by Lewis et al.,[1] this new analytical tool represents the union of a FT-IR step-scan spectrometer, an IR microscope, and most importantly, an IR focal plane array detector. The result is an instrument that has expanded opportunities for the characterization of heterogeneous samples through the collection of near-IR and mid-IR spectroscopic image data.[2-20] The imaging FT-IR system permits rapid collection of thousands of IR spectra across a microscopic or macroscopic spatial region. While there is some sacrifice in the signal-to-noise of the spectra at each pixel relative to traditional IR mapping experiments, the FT-IR imaging spectrometer can collect hyperspectral images in a matter of minutes instead of many hours.

Data collected from the imaging spectrometer can be organized as a three dimensional matrix composed of an infrared spectrum at each pixel to yield one spectral dimension and two spatial dimensions. Because there are hundreds of wavelength channels, this image data set is termed a hyperspectral image. Image maps are easily created using intensities at individual spectral channels or linear combinations of all or selected channels obtained with methods such as principal component analysis (PCA).[21]

Since the introduction of imaging FT-IR spectrometers, several groups have published qualitative results for the characterization of a wide variety of samples. Lewis et al.[1] first published spectral images of resolution targets and surfactant systems. More recent papers have been published that present qualitative and semi-quantitative imaging results for a variety of biological systems.[2,3,5] Koenig et al. [8,12,14-16] have published qualitative and semi-quantitative results of analyses of polymer dispersed liquid crystal systems. Marcott et al. [17-19] have investigated biological, agricultural, and polymer samples combining two-dimensional techniques with FT-IR imaging. Budevska [20] has demonstrated improvements in spatial resolution through the use of a multivariate curve resolution technique.

Previous studies have demonstrated the strong potential of hyperspectral imaging in characterizing spatially heterogeneous samples in the IR, but few have performed accurate quantitative analyses. This trend is not surprising given the rapid commercial development of the first-generation FT-IR hyperspectral imaging systems and the limitations of these early instruments. The first IR imaging systems used refractive optics that introduced chromatic aberrations in the image data. Chromatic aberrations can seriously limit quantitative analysis of the hyperspectral image data set. Quantitative analyses and qualitative interpretation will be

greatly improved if the data are corrected for chromatic aberration.

Given the large amounts of data produced by FT-IR imaging spectrometers, qualitative or quantitative analyses can be enhanced with multivariate data reduction. Software originally developed for satellite remote sensing can play an important role in visualization and qualitative analysis of hyperspectral image data. One software package of note is the Environment for Visualizing Images (ENVI), which is an interactive software environment.[22] By transforming the image data with a noise-adjusted principal component analysis algorithm, i.e., the minimum noise fraction (MNF) transform, the ENVI software allows rapid visualization and mapping of the spectral images while bringing the highest signal-to-noise information in the spectra to the forefront. Combined with routines written in house with Matlab and Grams software, the work in this paper will describe the integration of various multivariate algorithms into a quantitative analysis solution.

Because changes in pathlength and concentration are often confounded in IR spectra, we first describe a new approach to identify the best spectral region to use in normalizing the spectra for variations in the pathlength across the sample image. An additional challenge common in the analysis of heterogeneous samples is the lack of suitable standards to construct traditional quantitative multivariate spectral calibration models. We will demonstrate methods for extracting pure-component spectra from hyperspectral images of heterogeneous samples to be used in developing quantitative composition image maps of the samples. We evaluate the performance of existing and new multivariate algorithms and demonstrate new algorithms that can yield quantitative analyses of heterogeneous samples even in the presence of chromatic aberrations.

FT-IR spectroscopic image data are analyzed for a sample containing a small number of components deposited onto a known substrate in a semi-quantitative manner. The sample was created with microscopic features of pure and binary mixtures of three components by printing a pattern of yellow, magenta, and cyan inks on aluminum foil using an inkjet printer. The apparent simplicity of this sample belies the complex optical and spectroscopic artifacts that will be demonstrated in our quantitative hyperspectral image analysis of the ink sample.

THEORY

Pathlength Variation. When pathlength varies over the imaged area of the sample, concentration information will be confounded with pathlength changes since pathlength and concentration changes are generally indistinguishable. These pathlength variations can be largely corrected if the Beer-Lambert law is closely followed and if a spectral region can be identified that represents only pathlength variations. The identification of the optimal spectral region related to pathlength is critical since spectral variation due to pathlength variations can be greater than those caused by concentration changes. The first requirement in selecting a band for pathlength correction is to identify, if present, a spectral band shared by all IR active species in the heterogeneous sample. Isolating and baseline correcting all the candidate bands in the image spectra facilitates selection of appropriate spectral bands for correcting pathlength variations. The second step in selection of the optimal pathlength-related spectral band is the identification of a band that exhibits primarily multiplicative changes with no significant changes in spectral

shape caused by composition variations. If a spectral band common to all components represents only linear pathlength variation, then only one source of spectral variation will be present in the band above the noise and that spectral variation will have a spectral shape that is the same as the average spectrum for the band. PCA can be used to identify spectral bands that meet this second set of requirements. A necessary, but not sufficient, condition for a multiplicative pathlength effect is that the first eigenvector of the identified band both closely match the shape of the band's average spectrum and account for the vast majority of the spectral variance in the band. The criterion for the amount of spectral variance contained in the first eigenvector is dependent on the amount of noise present in the spectra, the linearity of the system, and the level of quantitative accuracy required. If pathlength variations exist in the sample but a spectral band cannot be found that adequately meets these criteria, then quantitative accuracy will be limited because pathlength and concentration variations are confounded.

Once an appropriate spectral band has been selected for pathlength correction, pathlength correction terms must be determined for each spectrum in the hyperspectral image. Assuming the sample absorbances follow the Beer-Lambert law, the image spectra can be normalized for the measured relative pathlength variations by dividing each spectrum by its estimated relative pathlength. We recommend that classical least squares (CLS) analysis with simultaneous linear baseline fitting[28] be used to estimate the relative pathlength for each spectrum. The mean spectrum of the band is chosen as a low noise representation of the spectral band, and we assign it a relative pathlength of one in the CLS analysis.

PCA, MNF Transform, ENVI and the Pixel-Purity Index. To obtain optimal qualitative and quantitative results in multicomponent systems, multivariate techniques such as principal component analysis and partial least squares (PLS) are often employed to analyze FT-IR spectral data. Multivariate methods use a large number of spectral channels to take advantage of the signal averaging and resolving power inherent in spectral data. The multivariate nature of the spectra and the massive amount of data in hyperspectral FT-IR images allow the characterization of systems with low signal-to-noise ratios and with multiple components whose spectral features overlap. Multivariate data also provide the opportunity to correct systematic spectral artifacts and aberrations introduced by the instrument.

While PCA remains the most common multivariate technique for visualizing and analyzing hyperspectral image data, several assumptions at the heart of PCA have been demonstrated to be problematic for some hyperspectral image data. PCA is a maximum likelihood method when the noise is uncorrelated and has constant variance across the spectrum. However, hyperspectral image data produced from the commercial FT-IR imaging spectrometers displays heteroscedastic and correlated noise.[23] Thus, the magnitude of the noise is wavelength dependent, and the noise is correlated between wavelength channels. When noise is heteroscedastic and correlated, PCA may order factors in a non-optimal fashion. In this case, important sources of spectral variation can become relegated to latter factors where they are often not seen. Additionally, subtle but important differences between factors can become lost.

Investigators working on satellite remote sensing data proposed a solution in the form of a noise-adjusted principal components analysis called the minimum (or sometimes maximum) noise fraction (MNF) transform.[24,25] The MNF algorithm seeks to decorrelate and whiten the spectral

noise before performing PCA. The MNF transform orders factors according to signal-to-noise ratio rather than spectral variance. The mathematical approach outlined by the authors is simple but requires *a priori* knowledge or empirical estimation of the noise covariance of the data. The MNF transform is similar in its goals to the maximum likelihood PCA approach described by Wentzell et al.[26] but is computed differently. The MNF transform first performs an eigen analysis on an estimate of the noise covariance matrix, $\mathbf{V}_n$, of the spectral image resulting in the normalized eigenvector matrix E,

$$\mathbf{E}^T\mathbf{V}_n\mathbf{E} = \mathbf{D}_n$$

where $\mathbf{D}_n$ is the diagonal matrix of eigenvalues. PCA is then performed on $\mathbf{F}^T\mathbf{V}_R\mathbf{F}$, where $\mathbf{F} = \mathbf{E}\mathbf{D}_n^{-1/2}$ and $\mathbf{V}_R$ is the sample covariance matrix. Thus, the MNF transform involves two PCA transforms. The first PCA both whitens and decorrelates the noise. The second PCA transform is then performed on the corrected data that follows the assumptions inherent in PCA.

Several methods are described in the literature for estimating the noise covariance matrix.[24,25] The MNF technique was originally developed for satellite spectral image data where there was no opportunity to collect repeat images. Therefore, a noise covariance estimation technique suitable for single-image spectra was developed.[24,25] It is assumed that the signal in the image is slowly varying while the noise varies from pixel to pixel. Thus, the error covariance matrix can be estimated by a shift difference procedure. In the ENVI software, the noise covariance estimate is obtained by subtracting the spectrum of neighboring pixel to the left from that of the current pixel. The resulting difference spectrum is averaged with the difference spectrum obtained by subtracting the neighboring pixel above. This mean difference is calculated for every pixel, resulting in an estimate of the noise covariance matrix of the spectral image. The ENVI noise covariance estimation assumes the major difference between neighboring pixels is noise; an assumption that may not be valid when distinct boundaries exist in the image. ENVI also allows noise estimates to be imported from other external sources, such as a dark current measurement or from the difference between repeat spectra of the entire image.

ENVI contains several software tools that use MNF scores to obtain pure-component spectra from heterogeneous spectral image data. The pixel-purity index (PPI) isolates the most extreme pixels in the data space and can be used to select specified numbers of spectra representative of the purest (i.e., the most extreme) pixels in the image. The PPI is computed iteratively through the projection of a random unit vector onto the MNF score space. The location of the projection of the scores onto the unit vector is recorded as a purity index value. By retaining only those pixels whose purity index falls above a threshold, one is able to isolate spectra of pixels with the most unique information while eliminating background and mixed pixels.

Finally, ENVI enables the MNF score space to be visualized as it is rotated through the various dimensions in all possible combinations of factors. Thus, by watching numerous rotations, the researcher can observe data clusters and distributions in more than three dimensions. Pixels on the extreme vertices of clusters are separately selected and their spectra averaged. These averaged extreme vertex spectra represent estimates of the pure-component spectra. The accuracy of these estimated pure-component spectra is dependent on the existence of pixels representative of the pure-component species somewhere in the image. ENVI simply allows the analyst to identify the purest pixels in the image and to export them for further use. ENVI also allows mapping of selected vertex clusters to pixels in the original image to provide a visual

distribution of pure pixels throughout the sample image.

Once pure-component spectra are estimated from the image data, CLS methods can be used to obtain concentration estimates for all species represented by the pure-component spectra. Thus, quantitative composition maps of the images can be generated if pure pixels are present in the image. However, we have found that chromatic aberrations present in the FT-IR hyperspectral images can greatly degrade the quantitative CLS analysis of the image data.

Chromatic Aberration. Various aberrations are possible in optical systems where higher order terms detract from the idealized first-order models of Gaussian optics. Of these aberrations, chromatic aberrations can severely impact multivariate qualitative and quantitative analyses since their effects vary as a function of wavelength throughout the IR spectral image. Chromatic aberrations are caused by the wavelength-dependence of the index of refraction of a lens, which in turn changes the focal length of the lens as a function of wavelength. Chromatic aberration can contain both lateral and axial components. The axial component of chromatic aberration changes the location of the focal point as a function of wavelength, and the lateral aberration can change the position of the image as a function of wavelength. Thus, chromatic aberrations can cause changes in the relative intensities of the spectral bands, image shifts, and changes in the magnification of the image that are each wavelength dependent. We will demonstrate that chromatic aberrations can generate significant deviations in the Beer-Lambert law.

Chromatic aberrations are apparent in the image as blurring and spatial shifting of the image. IR radiation "spills" across pixels resulting in spectral mixing which varies as a function of wavelength. Light spills across areas of low absorption onto areas of high absorption reducing the measured absorbance of the higher absorbing pixels in a wavelength dependent manner. This effect is greatest for pixels lying on the boarder between one spatial region and another.

To a multivariate analysis technique, which simply processes the data as a two dimensional stack of data, these changes in the spectra appear to introduce wavelength-dependent changes in spectral intensities that are indistinguishable from chemical changes in the sample. Thus, chromatic aberrations greatly hamper the estimation of pure-component spectra from spectral image data and degrade the multivariate quantitative analysis even if true pure-component spectra are known.

Classical Least Squares and Prediction-Augmented Classical Least Squares. The CLS method is a standard multivariate method for quantitative analysis of spectral data.[27-36] It is a linear least-squares method based on adherence to the Beer-Lambert law. Since the presence of chromatic aberrations is highly detrimental to the quantitative multivariate CLS analysis of the image spectra, new methods are required to correct for wavelength-dependent aberrations. We have recently introduced prediction-augmented classical least squares (PACLS).[37] The PACLS algorithm improves CLS by allowing a calibration model to be corrected during prediction for unmodeled spectral components. If estimates of the unmodeled spectral components can be obtained, PACLS corrects the prediction results for the presence of the unmodeled components. The spectral influences of chromatic aberration are mathematically equivalent to the addition of spectral components to the image data. We can obtain linear estimates of the effect of chromatic aberration on each pure-component spectrum by subtracting the pure pixel spectra from the

chromatic aberrated spectra located at the spatial boundaries of each region of the heterogeneous sample. Once the linear estimates of the spectral shapes of chromatic aberration for each component are obtained, they can be added to the CLS prediction to correct the analysis of the pure components for the presence of the chromatic aberration. In addition to composition maps of the pure components obtained with the PACLS analysis, quantitative maps of the magnitude of the chromatic aberrations for each component can also be generated.

EXPERIMENTAL

BioRad Stingray FT-IR Spectrometer. Spectra were collected at the BioRad facility during evaluation of the BioRad Stingray (BioRad Laboratories, Cambridge, Massachusetts) FT-IR imaging system. The system included the BioRad FTS-6000 step-scan FT-IR bench and the Biorad UMA-500 IR microscope. Detectors included a single-point mercury-cadmium-telluride (MCT) detector and a 64 x 64 pixel MCT focal plane array (FPA) detector (Santa Barbara Focalplane, Goleta, California). A single-element ZnSe lens transferred the output of the microscope image from the UMA-500 to the FPA detector. Single-beam image spectra were collected in reflectance using the microscope with a spot size of approximately 400 μm x 400 μm. The step-scan system used a stepping rate of 2.5 Hz with 80 frames coadded for each spectrum. Triangular apodization and Mertz phase correction were applied to the interferograms. Spectra at a nominal resolution of 16 cm^{-1} were collected with an undersampling rate (UDR) of 4 to yield a maximum digitized frequency of 3904 cm^{-1}. Spectra were truncated to the sensitive range of the detector, i.e., 900 to 3900 cm^{-1}. A glass microscope slide vapor-deposited with gold was used as a background for both the point and image spectra. Final reflection-absorption spectra were obtained by ratioing each sample single-beam spectrum by the corresponding gold reflection single-beam spectrum followed by taking the negative log of the ratio. Collection of high-quality single-point microscope spectra of the center of each of the three pure components on the sample was obtained with the single-point MCT detector. For these data collections, the UDR were set to 2 and 128 scans were coadded. Norton-Beer medium apodization and Mertz phase correction were applied to the interferograms collected at a nominal resolution of four wavenumbers.

Chromatic Aberration Characterization. To characterize chromatic aberration in the imaging spectrometer, an xacto blade was used to block a portion of the IR image. For this study, single-beam image data were collected in macro-mode (spot size of 4 mm by 4 mm) with 16 cm^{-1} spectral resolution and an under sampling ratio of 4. A 2.5 Hz stepping rate was used with 80 frames coadded for each interferogram point.

Inkjet Sample. To evaluate the FT-IR imaging spectrometer and the algorithms developed for data analysis, a simple, reproducible, and at least semi-quantitative sample was needed. The difficulty in sample selection was exaggerated by the small image size, 400 μm by 400 μm. We generated an appropriate sample by printing ink spots on an aluminum foil with the use of an inkjet printer. For the observed color of the printed ink spots to be correct, the programmed colors of the inkjet spots should be at least semi-quantitative in the mixture of the three complementary color inks: yellow, magenta, and cyan. Therefore, a strip of commonly available Reynolds Wrap kitchen grade aluminum foil was taped to paper and fed through a Hewlett

Packard DeskJet 722C printer. The printer printed a pattern of single-pixel spots specially designed in Adobe PhotoShop. The magnified pattern is shown in Figure 1. The pattern contains each pure ink as well as the three 50:50 binary mixtures of the pure inks. In practice, the inkjet printer rarely gets all the colored ink drops for each of the six spots perfectly aligned on a microscopic scale. Therefore, a large matrix of these patterns was printed, and a microscope was used to identify a group that visually had optimal mixing and spatial characteristics. The area around this group was cut out and 3M-brand spray-on glue was used to fasten the sample onto a glass microscope slide. A visible image of the pattern collected on the FT-IR imaging microscope spectrometer is shown in Figure 2. The visible image is slightly translated relative to the image collected in the IR. However, distinct yellow, magenta and cyan spots are visible along with their binary mixtures of yellow + magenta (red), yellow + cyan (green), and magenta + cyan (blue). Rolling marks are also visible on the aluminum substrate, indicative of the commercial aluminum foil that was used.

Data Analysis. The BioRad-supplied WinIR Pro/ImageIR software was used for data acquisition and initial spectral processing. Image spectra were exported to Grams/32 SPC format for use with Sandia-developed chemometrics software. The Sandia software was used to isolate spectral regions and separately baseline correct each spectral region of each spectrum before final analysis. Our software was also used in the eigen analysis determination of the best pathlength-correction band and in the creation of CLS and PACLS calibration and prediction models used in estimating relative pathlength correction terms and relative concentrations of the species of interest. ENVI version 3.2 (RSI, Inc., Boulder, Colorado) was used for visualizing the data and isolating spectra most representative of the pure-component spectra. Matlab version 5.3 (The Mathworks, Inc., Natick, Massachusetts) was used to plot the results. Calculations were performed on a Dell Precision 610, dual processor Intel 500MHz Pentium II Xeon system with 512MB of RAM running Microsoft Windows NT4.0.

RESULTS AND DISCUSSION

Chromatic Aberration Characterization. An investigation was performed to demonstrate the chromatic aberration present in spectra collected from the imaging system. To minimize the effects of diffraction, a hyperspectral image of the xacto blade was obtained in macroscopic mode with a spot size of 4 mm by 4mm. In the absence of chromatic aberration and diffraction, the IR radiation should be completely blocked at all IR wavelengths for all pixels obscured by the blade. However, with chromatic aberration present, IR radiation at low energy (long wavelength) will be out of focus and blurred compared to high-energy radiation if the high-energy portion of the IR beam is focused sharply on the edge of the xacto blade. Thus, pixels in locations where the blade edge has blocked the radiation at short wavelengths will have some transmission at longer wavelengths.

This trend is clearly seen in Figures 3A and 3B where images of the IR transmission of the xacto blade are shown for the 3657 and 957 cm^{-1} bands, which are near the extreme ends of the spectral range. The outline of the xacto blade is clearly sharper in the short-wavelength image than in the long-wavelength image. In addition, Figure 3C shows a profile of the transmission intensity across row 15 for pixels in columns 22 through 34 that span the transition across the

edge of the xacto blade. Clearly the transition is significantly sharper for the short-wavelength, demonstrating the dramatic effects of chromatic aberration.

As can be seen in Figure 3A and B, not only does the image blur at long wavelength, it also appears to spatially shift. This effect is most likely due to the lateral component of the chromatic aberration caused by a tilt in the image plane relative to the sample. The xacto blade image clearly demonstrates a portion of the chromatic aberration problem for the imaging FT-IR system, and suggests that qualitative and certainly quantitative analyses will require corrections for these effects in order to produce useful results with high fidelity for the samples being measured.

Spectral Analysis. Following the chromatic aberration study, experiments were performed to evaluate a quantitative analysis methodology for FT-IR image data obtained from a heterogeneous sample. Samples of pure and binary mixtures of inks on an aluminum substrate were used to test analysis methods on simple microscale samples.

The inks dispensed by the HP printer are standard commercial products shipped with the printer. In order to be useful for this study, the individual inks must contain chemical species with IR spectral bands that uniquely differentiate them from each other. High-quality IR spectra were collected using the single-point detector imaged on the three pure ink spots. The resulting yellow, magenta, and cyan spectra are shown in Figure 4. Spectral bands characteristic of the O-H stretch, C-H stretch, as well as peaks throughout the fingerprint region are clear. Unfortunately, most of the same IR bands are shared in common by all three inks. The clearest differences between the spectral features present in the inks can be seen in the O-H stretching region, where yellow has a narrower band shape and the peak maximum is shifted. In addition, intensity and shape differences are clear in the 1300 to 1450 cm^{-1} region where, again, yellow has a characteristically strong absorbance followed by magenta and finally cyan. Differentiation between magenta and cyan is limited to this 1300 to 1450 cm^{-1} region, since their C-H and O-H stretching bands are very similar. While the degree of differentiation for yellow spectral features relative to the other inks is adequate for this study, the degree of overlap for the IR bands produced by the magenta and cyan ink spots suggests that they are in fact chemically very similar. Discussions with the manufacturer verified that the IR features apparent at this spectral resolution originate primarily from the binders, and that magenta and cyan share a common binder that differs only in pH.

Using the MCT array detector, 4096 (64 x 64) spectra were collected in a single image of the ink sample. For clarity, Figure 5 contains representative absorbance spectra from every fiftieth pixel spanning the image. There is a large background offset in many pixels. Examination of the sample and background single-beam spectra revealed that the background image varied spatially in a systematic manner consistent with the gold mirror background slide being tilted relative to the image plane. The non-absorbing features of the sample single-beam sample spectra did not have this systematic variation indicating that it was placed parallel to the image plane. Compared to spectra collected with the single point detector, the image spectra have a lower signal-to-noise ratio due to the small size of each pixel in the FPA detector and the lower amount

of signal averaging. Nevertheless, the strong IR bands in the 1300 to 1450 cm^{-1} region, C-H

stretch region, and O-H stretch region are clearly present in the image spectra of the ink sample.

The effect of chromatic aberration in the image spectra is readily apparent upon close inspection of pixels from the center and edge of individual ink spots as well as in the relative intensity of long wavelength spectral bands in some mixture ink spots. Figure 6 demonstrates the edge versus center pixel chromatic effect as well as the way in which Beer's Law is no longer followed for spectra from the green ink spot. In this case, the lowest energy region from the green spot clearly illustrates a non-additive effect when compared to the yellow and cyan pure-component spectra that make up the green mixture. Positive linear combinations of the yellow and cyan ink spectra cannot yield the relative intensities observed in the green spot presented in Figure 6. Note that relative to the OH stretching vibration, the lower energy band of the green spot is lower in intensity than either the yellow or cyan bands of which it is composed. The spatial location of this latter chromatic aberration suggests that lateral chromatic effects are present across the dimensions of the imaged sample

Pathlength Correction and Windowing. The first step to quantitative analysis requires the determination of a spectral band to be used to characterize the relative pathlength for each pixel in the image. An inspection of the spectral bands yielded three bands that did not appear to visually display spectral shape changes as a function of ink composition. The mean spectrum and first eigenvector for each of the three regions after separate linear baseline corrections are shown in Figure 7. The first band lies between 930 and 970 cm^{-1} and has a first eigenvector explaining only 87% of the total variance in band absorbance suggesting that shape changes are present in this particular ink band. In addition, the mean spectrum of the band does not closely resemble the shape of the first eigenvector further suggesting that this band changes shape with position and is not the best candidate for pathlength correction. The second band was a stronger peak between 1003 and 1070 cm^{-1}. This region better fulfilled our requirements for a candidate pathlength correction band since the first eigenvector explained over 96% of the variation in the band. However, the third peak in the C-H stretching region equally fulfilled our requirements and had a more regular baseline overall. In addition, since this third band is centered in a higher energy, shorter wavelength region, it is less affected by chromatic aberration compared to either of the other two longer wavelength regions. Therefore, this third band was selected for use as a monitor of the relative pathlength of the sample.

The relative pathlength correction factors for each pixel were determined by the use of a standard multivariate CLS prediction of the C-H stretching region for each pixel. The CLS prediction included the mean spectrum of the pathlength band and offset and linear spectral terms in the model to simultaneously fit the pathlength and a linear baseline. Relative pathlengths determined for each pixel are shown in Figure 8. Regions of the image where ink was present are clearly seen, and generally the pathlengths are consistent across all the inks except the red ink. The center of the red spot demonstrates a striking increase in the relative pathlength indicative of a particularly heavy application of ink for this spot.

Following the CLS estimation of relative pathlength terms, pathlengths with values below 0.1 (primarily from the background aluminum foil pixels) were set to a value of one to prevent values near zero from inappropriately inflating the intensities of the pathlength-corrected spectra. The spectrum from each pixel was divided by the corresponding pathlength to normalize the

spectra for pathlength and remove this source of variation from the spectra. Following pathlength correction, the FT-IR image spectra were further processed to isolate and baseline correct the three main bands used in the quantitative analysis. The results of this preprocessing are shown in Figure 9, which demonstrates the same representative subset of spectra as shown in Figure 5.

MNF Transform and Chromatic Aberration. Once the image spectra were windowed to isolate bands of interest and preprocessed to remove linear baseline and pathlength variations, ENVI was used to perform the MNF transform on the ink spectra as the first step in determining pure-component spectra. Initially, only the left half of the image was analyzed with the MNF transform since this was where the pure ink pixels were located. Since repeat images were not available, the shift-difference method of ENVI was used to estimate the noise covariance matrix of the spectral image. Two different noise covariance matrices were calculated and used to obtain MNF scores. In the first case, the entire spatial region of the spectral image was used in estimating the noise covariance. However, since there are sharp boundaries between different spatial regions in the sample (i.e. inks spots and the background), a second calculation of the covariance estimate was performed using the central spatial region consisting only of background pixels including columns 26 to 32 and rows 1 to 64. Starting with scores from the first MNF calculation, the pixel purity index (PPI) was determined after 100,000 iterations using a threshold of 1.5 in order to select a subset of spectra from the approximately 2000 total pixels that contain the most unique information. The resulting 760 pixels that were selected were used for plotting and further study discussed below.

Ordinary PCA scores as well as MNF scores computed using each of the two covariance estimation methods were plotted for factors one, two, and three as shown in Figure 10 for the 760 selected pixels. Although scores in each case were calculated using the spectra from the left half of the image, for clarity only the 760 scores for pixels selected by the PPI calculation shown. PCA scores (Figure 10A) contain only two distinct clusters of pixels, a cluster containing scores from yellow ink spot pixels and a second cluster with magenta and cyan scores mixed together. Figure 10B with MNF scores computed using only a central background spatial region for the noise covariance estimation yields a similar result. However, Figure 10C shows three distinct clusters, one for each of the pure inks when the MNF transform was computed using the entire left half of the image. If pseudo-color images are constructed from these latter MNF scores by mapping the intensity of the first, second and third factor to red, green, and blue, each of the three ink spot regions have unique contrast. If PCA or the second MNF technique is used, the resulting pseudo-color image shows no contrast differentiating magenta and cyan due to the fact that these PCA or MNF scores do not differentiate magenta and cyan spectra.

In order to comprehend the results presented above, it is important to understand the MNF transform and the effect of using a shift difference spectrum for estimating the noise covariance matrix. One goal of the MNF transform is to correct the eigenvector decomposition of the spectral data in the image for the detrimental effects of non-uniform and correlated noise. If the spatial variations of the image are slowly varying, the shift difference calculation performed by ENVI should provide a reasonable estimate of the error covariance matrix used to correct the MNF scores for non-uniform and correlated noise sources. However, for an image with sharp spatial boundaries, the ENVI shift difference estimate of the error covariance can be dominated

by spectral differences on opposing sides of the boundaries. In this case, the error covariance estimate can contain spectral signal of the analytes that the MNF transform treats as correlated error that is to be ignored. For spectra from an image without chromatic aberration, we might expect full image MNF transformed scores to yield poor results when the spectral differences used to compute the error covariance estimate are dominated by spectral features at the edges of the homogeneous regions in the image. The MNF transform attempts to isolate the signal that is orthogonal to the error covariance, but the error covariance estimate from the shift difference of the entire set of image spectra will be dominated by the contrast between the boundaries of the aluminum and ink spots. However, in our case, the spectra found at these boundaries are strongly affected by chromatic aberration. Thus, the shift-difference approach using the entire image to estimate the error covariance is dominated by chromatic aberration, and the MNF transform actually aids in removing the effects of chromatic aberration in the MNF scores. Since these scores minimize the chromatic aberration, distinct clusters for each of the three inks are observed. Using only homogeneous Al regions in the image to estimate the noise covariance matrix, little benefit is derived from the MNF transform over the PCA transform and unique clusters of scores are not apparent for all of these species. In spectral images not dominated by chromatic aberration, care must be taken that the noise covariance estimate truly represents the noise in the data and is not dominated by spectral features of the analytes. If analyte spectral features due to sharp compositional boundaries in the image dominate the noise covariance estimate, then the MNF transform will treat the analyte features as correlated noise and will simply serve to eliminate the true analyte spectral features. Poor predictions might then be expected.

Pure-Component Determination and Prediction Results. MNF scores that were computed with the full image noise covariance estimate were used in an interactive analysis in ENVI to isolate pure-component spectra. By viewing and rotating the projection of the MNF scores from multiple dimensions (10 in this case) onto a two-dimensional plot, we were able to identify and select distinct clusters of scores for each ink as well as pixels on the borders of inks affected by chromatic aberration. By noting the location of pixels corresponding to the scores selected in each cluster, it was possible to assign each cluster to specific ink spots. Pure-component spectra were generated by obtaining the mean of each ink spectrum and aberration cluster and are shown in Figure 10. Pairs of spectra, one for pure ink and a second representative of the spectra affected by chromatic aberration, are shown. Once again, the yellow pure components have distinct features while the magenta and cyan are similar.

The mean spectra representing the pure-component inks were then used in a CLS prediction step to obtain relative concentration terms for each component across the entire pathlength-corrected image data set. Concentration image maps for each component were then created where intensity at each pixel is mapped to relative concentration. Results of these predictions for the case where only the three ink pure-component spectra were used in the CLS prediction are shown in Figure 10. Prediction results of yellow (Figure 10A) show strong selectivity for the pure yellow ink spot, with no false prediction in either the magenta or cyan pure ink spots. With the binary mixture spots, the yellow component of the red spot was predicted with values matching the expected result of approximately half the value of the yellow pure ink spot. However, the predictions for the yellow component of the green spot were uniformly low and below expectation. Examination of the spectra at these points demonstrated bands in the 1350

cm^{-1} region that clearly did not show a linear mixing of yellow and magenta spectra as demonstrated in Fig. 6. Instead spectral features in this range were of low intensity and most closely resembled magenta features. It is likely that the CLS predictions are contaminated by chromatic aberration varying across the sample if lateral components of chromatic aberration are present in the image. CLS prediction results for the magenta pure ink component (Figure 11B) once again demonstrated strong prediction for the pure magenta spot as well as the red binary mixture. However, the blue spot is under predicted and some predicted magenta concentration is apparent in the green region where there should be no magenta present. Prediction results for cyan (Figure 11C) indicate strong prediction for the pure cyan ink spot, but also some predicted concentration on the border of the magenta pure spot. This false prediction on magenta using the cyan pure component is due to the fact that the cyan pure closely resembles magenta when the long wavelength 1340 cm^{-1} magenta band is diminished by chromatic aberration. The green binary mixture prediction results for cyan again show diminished concentration for this component, however cyan prediction results are strong for the blue mixtures spot.

Since the magenta and cyan pure-component spectra are nearly identical (i.e., highly collinear), it was very difficult to separately quantify these two components in mixture spectra. Therefore, we used the pure magenta spectrum as representative of both the magenta and cyan pure spectra in further analyses. We then applied the yellow and magenta pure spectra in a CLS prediction to obtain quantitative results that represent the concentrations of the yellow dye and the sum of the magenta and cyan. PACLS models were also constructed using the yellow and magenta pure-component spectra and difference spectra which represent linear approximations of the chromatic aberration for yellow and magenta spots (i.e., difference of mean edge spectra and mean center spectra calculated separately for the yellow and the magenta inks).

The two-component CLS prediction results are shown in Figure 12A for yellow and 12B for the combined magenta and cyan component. The four component PACLS predictions including correction for chromatic aberration are shown in Figure 12C for yellow and D for combined magenta and cyan. Figure 12E and 13F show PACLS predictions for the yellow chromatic aberration component and the combined magenta and cyan chromatic aberration component, respectively. Figure 12C results when compared to Figure 12A demonstrate improved predictions for yellow where the borders of the yellow pure ink are predicted more correctly when the chromatic aberration pure spectra were included in the predictions. Prediction results for the red and blue ink spots are also somewhat better for the case where chromatic aberration pure-component spectra were included in the analysis. By including the chromatic aberration components in the PACLS prediction step, this previously unmodeled spectral change is now explained within the model thereby correcting the prediction results for the pure ink components.

In addition to clear improvements in the yellow component predictions, Figure 12B shows much higher predicted concentrations for the combined magenta-cyan concentrations. By combining the highly collinear magenta and cyan pure components into one component, the PACLS prediction results now much more closely match the expected concentrations. In the case of the blue spot (50% magenta, 50% cyan), the predicted concentration now closely matches that of the pure magenta and cyan spots, as expected. For the red and green spots, in each case their predicted results are approximately half that of the other ink spots, due to the fact that half their composition is yellow ink. These concentration predictions further improve when the spectral

shapes representing chromatic aberration pure components are included in the PACLS model as shown in Fig. 12D. Once again, edges of the pure-component ink spots for both magenta and cyan are more correctly predicted once the chromatic aberration component is included in the model.

Figure 12E and 13F represent the prediction results of the yellow and magenta-cyan chromatic aberration components, respectively. These results clearly show the edge effects where chromatic aberration is the strongest. The prediction results for the edges of the ink spots were also markedly improved through the inclusion of the chromatic aberration components in the PACLS predictions.

CONCLUSIONS

By printing pure and binary mixture spots on an aluminum foil with an inkjet printer, we have been able to generate a simple semi-quantitative micro sample for testing various quantitative analysis methods applied to FT-IR spectral image data. Since the sample exhibited appreciable pathlength variations over the area of the image, a new method for selecting the appropriate spectral band for pathlength normalization was devised. A necessary condition for a spectral absorption band to represent primarily pathlength information was that the first eigenvector of the baseline-corrected band from the ink spectra in the image contain almost all of the spectral variance and that it closely resemble the average spectrum. Pathlength correction factors for the identified path-related band were determined with the use of a CLS prediction step that included the average spectral band and linear baseline spectral components in the CLS model.

Once the spectra were pathlength corrected, a variety of quantitative analysis tools were applied to the spectral images. However, refractive optics in the FT-IR imaging system generated wavelength-dependent chromatic aberrations that were found to be detrimental to some quantitative analysis methods. The MNF transform using the ENVI error covariance estimate calculated from the shift difference of the spectra in the image was more effective than PCA at separating the three pure ink spectra. The pixel purity index was applied to the MNF transformed data to identify those spectra that represented the purest spectra in the spectral image. These purest spectra mapped to the centers of the pure ink spots on the Al sample. Standard CLS models using linear baseline spectral components and the three pure ink spectra identified during the PPI analysis failed to yield the expected concentration maps for the ink spots on the sample. This failure was a result of the similarity of the magenta and cyan pure-component spectra and the presence of wavelength-dependant chromatic aberration effects in the spectra. The first problem was minimized by using the magenta pure spectrum as a representation of both the magenta and cyan dyes and predicting the sum of the magenta and cyan component concentrations in the spectral image. The chromatic aberration effects were corrected by obtaining linear estimates of the chromatic aberration of the pure ink spectra and adding these estimated chromatic spectra to the PACLS analysis of the image. PACLS was shown to be an effective multivariate tool that could minimize the detrimental effects of chromatic aberration on the concentration maps of the pure inks and improve both the quantitative accuracy of the predictions and the spatial resolution of the concentration maps. Diffraction effects in the spectral image are analogous in nature to chromatic aberration in that

they are similarly dependent on wavelength. Thus, we would suggest that the PACLS algorithm could also be used to improve the spatial resolution of composition maps derived from diffraction-limited spectral images.

The MNF transform was an effective method in the analysis of these data since the shift difference estimate of the error covariance matrix resulted in MNF scores that were forced to ignore the detrimental effects of chromatic aberration. We speculate that the application of the MNF transform using shift difference estimates of the error covariance matrix might actually degrade the quality of the quantitative composition maps obtained from spectral image data that does not have wavelength-dependent chromatic aberrations or diffraction effects present. Since new FT-IR imaging spectrometers are now sold without the presence of refractive optics that generate chromatic aberration, the positive experience of researchers applying the MNF transform may not carry over to these new instruments.

ACKNOWLEDGEMENTS

The authors would like to acknowledge Norman Wright of Bio-Rad Laboratories for aiding in the collection of the data while we were evaluating imaging spectrometers at Bio-Rad Laboratories. We would also like to acknowledge Fredrick Haiback and Michael Strunk at the University of New Mexico for their aid in generating the ink sample used in this work. Finally, David Melgaard is acknowledged for programming the Array Basic chemometrics software used in some of the analyses presented in the paper.

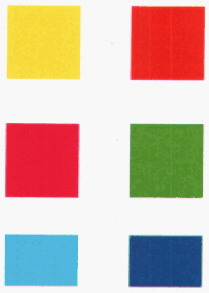

Figure 1. Pattern of ink spots created in Photoshop to be printed on the aluminum foil substrate. Yellow, magenta and cyan spots from top to bottom on the left represent the pure inks. Red, green and blue from top to bottom on the right represent 50% binary mixtures of each of the pure inks.

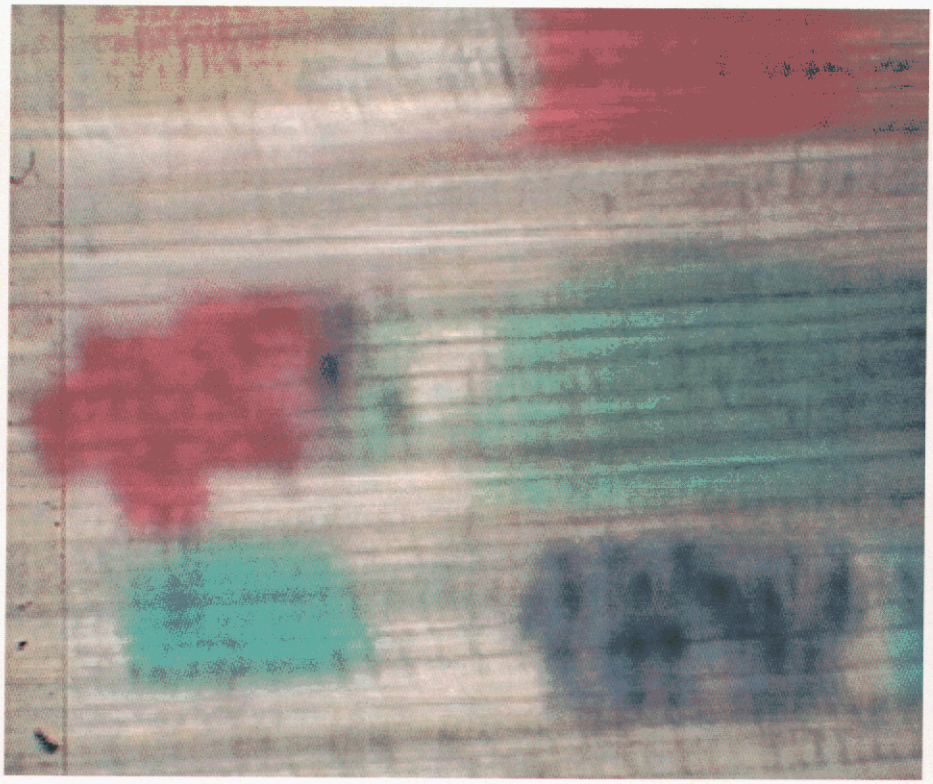

Figure 2. Visible image (slightly offset and tilted) of the actual ink spots used in the IR image data collection and analysis. In each of the mixture spots, the red, green, and blue color is apparent indicative of the fact that the ink droplets from each of the pure inks mixed correctly in each case. Note the clear rolling marks indicative of the commercial aluminum foil used as a substrate for the reflectance measurement.

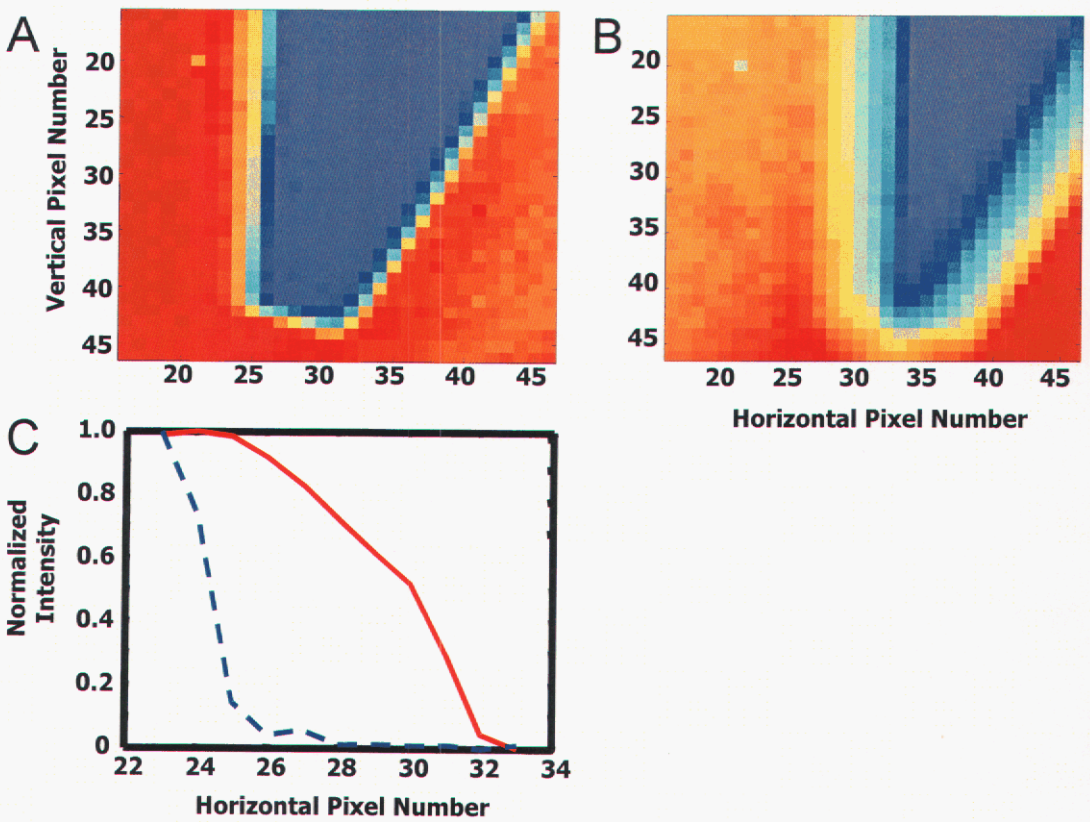

Figure 3. IR transmission intensity image with an xacto blade in the field of view at A) 3657 cm^{-1} and B) 957 cm^{-1}. Note the blurring of the edge and shifting of the image of the xacto at the longer wavelength. C) Normalized intensity at 957 cm-1 (solid line) and 3657 cm^{-1} (dashed line) across row 30 from columns 23 to 33.

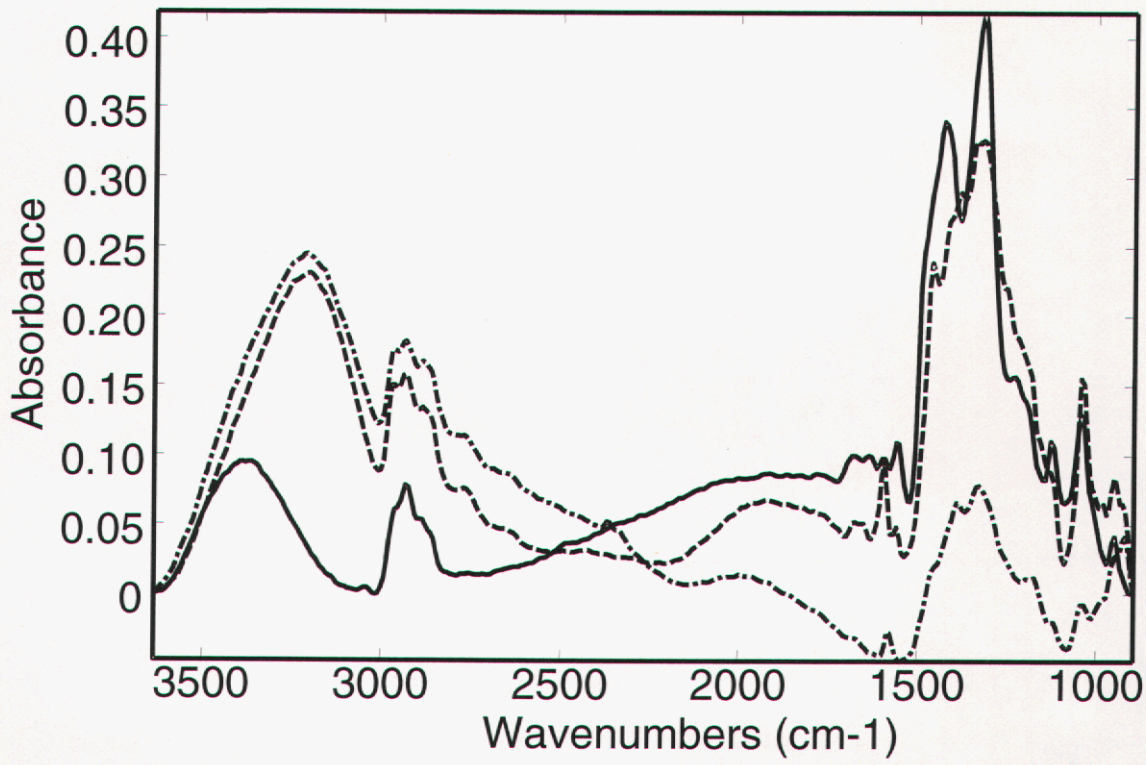

Figure 4. IR refectance spectra collected with a single-point MCT detector for yellow (solid line), magenta (dashed line) and cyan (line with dashes and dots) pure ink spots.

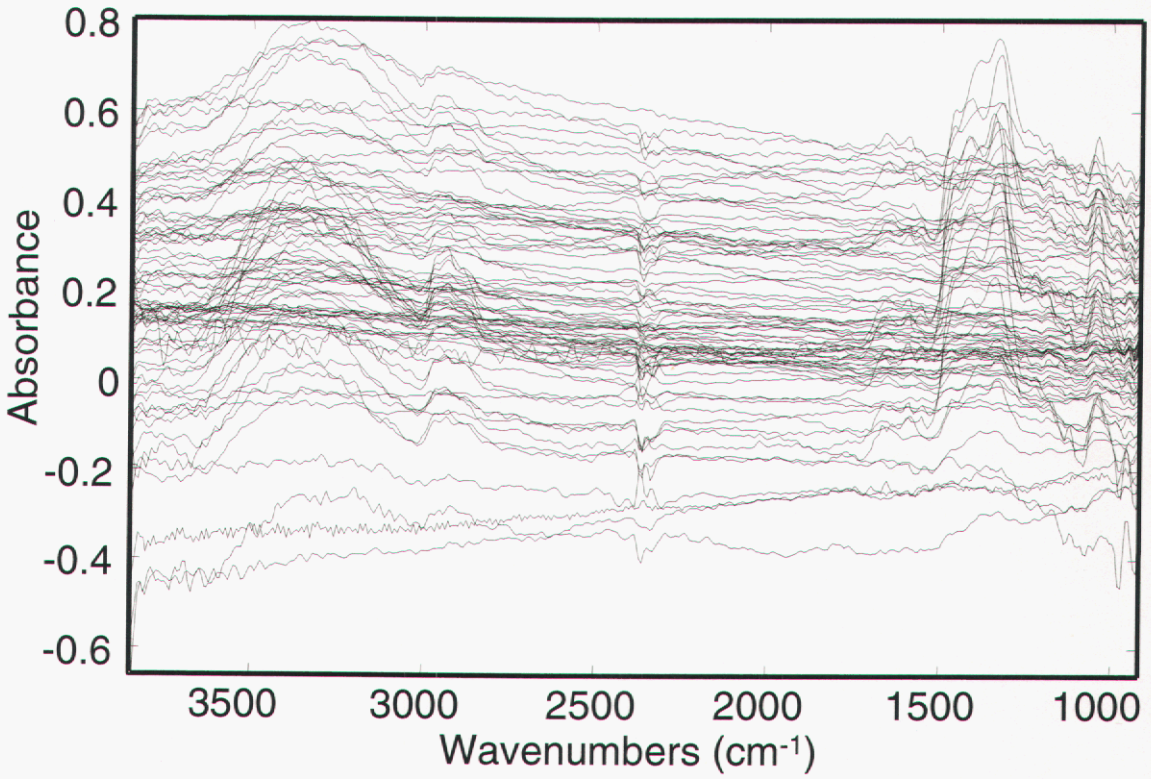

Figure 5. Representative absorbance spectra (1 out of every fifty) collected with the 64x64 pixel MCT focal plane array detector.

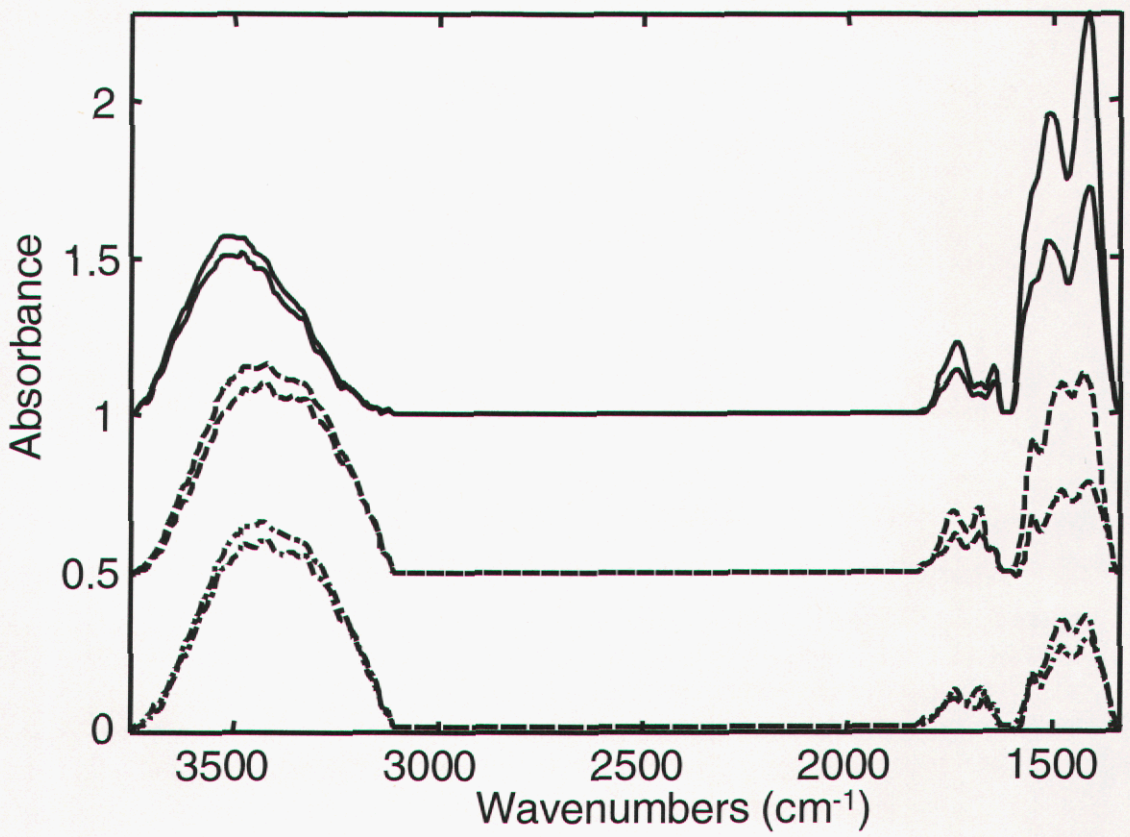

Figure 6. Windowed and linear baseline corrected spectra from the center and edge of the yellow ink spot (solid line), center and edge of the cyan ink spot (dashed line), and center and edge of the green (50% yellow, 50% cyan) ink spot (line with dashes and dots).

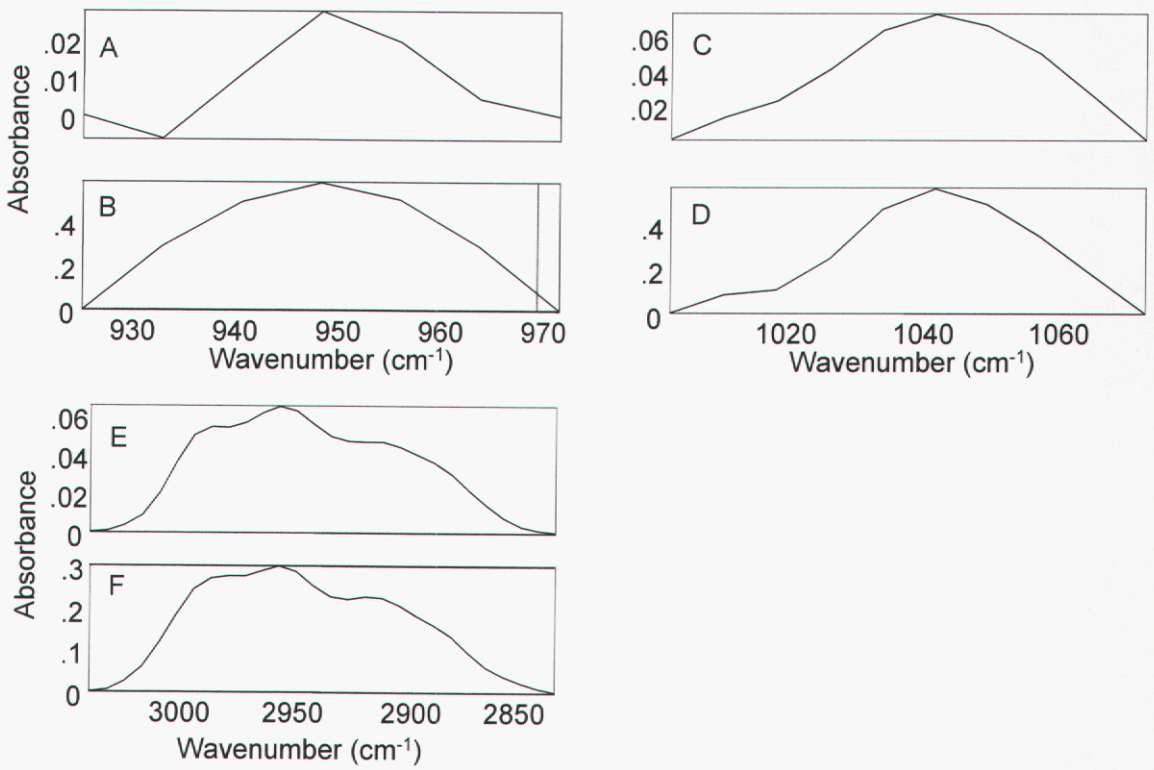

Figure 7. A) Average and B) first eigenvector for the 930-970cm^{-1} region. Eigenvector explains 87% of the total variance in that band. C) Average and D) first eigenvector for the 1003-1070cm^{-1} region. Eigenvector explains 96% of the variance in that band. E) Average and F) first eigenvector for the C-H stretch region between 2785-3016 cm^{-1}. Eigenvector describes 97% of the variance in that band.

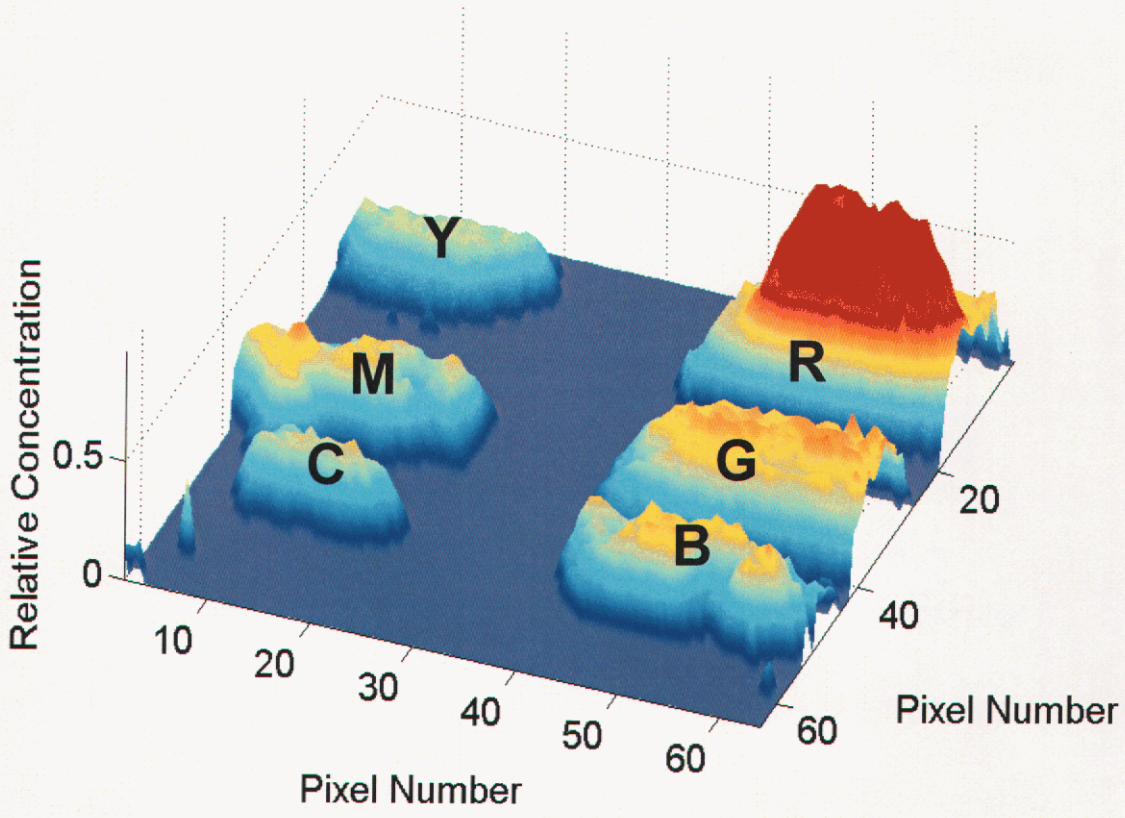

Figure 8. Pathlength correction terms computed using CLS from the mean of the C-H stretch region plotted as a 3 dimensional image.

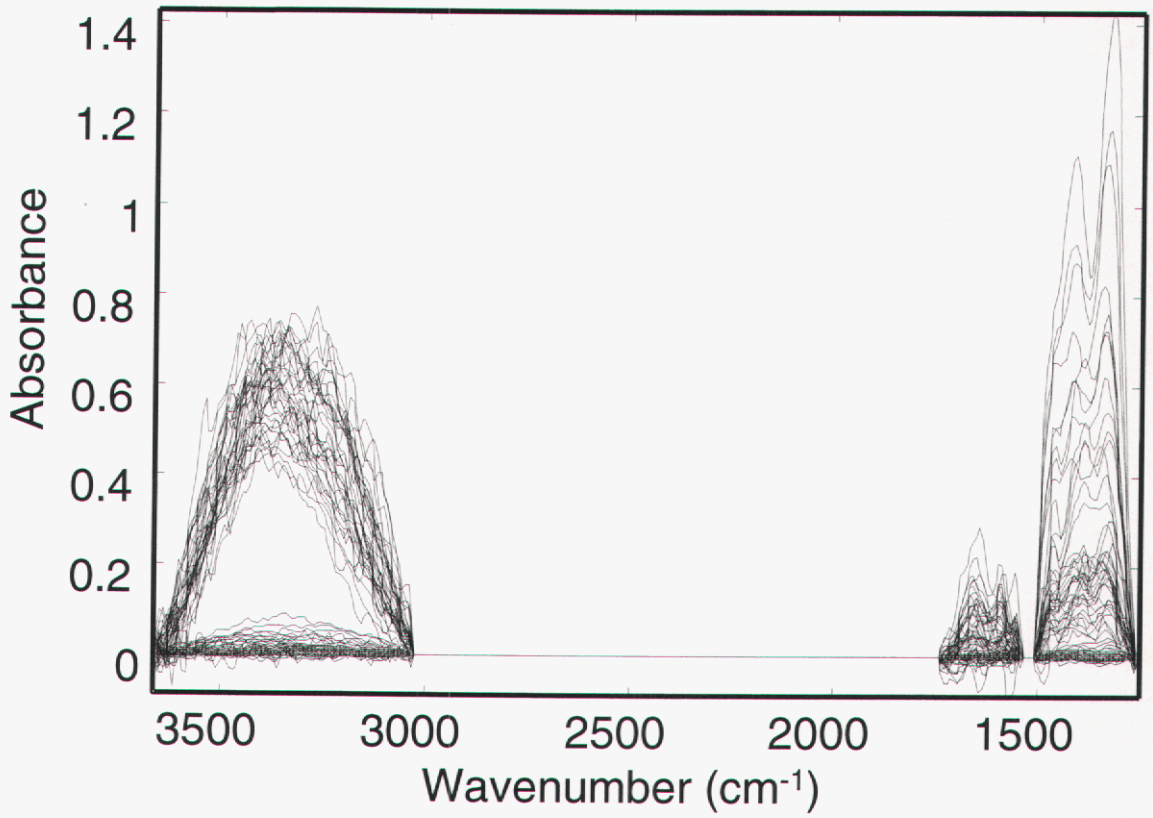

Figure 9. Results of applying pathlength correction to the windowed, baseline corrected absorbance spectra. Every fiftieth spectrum plotted for clarity.

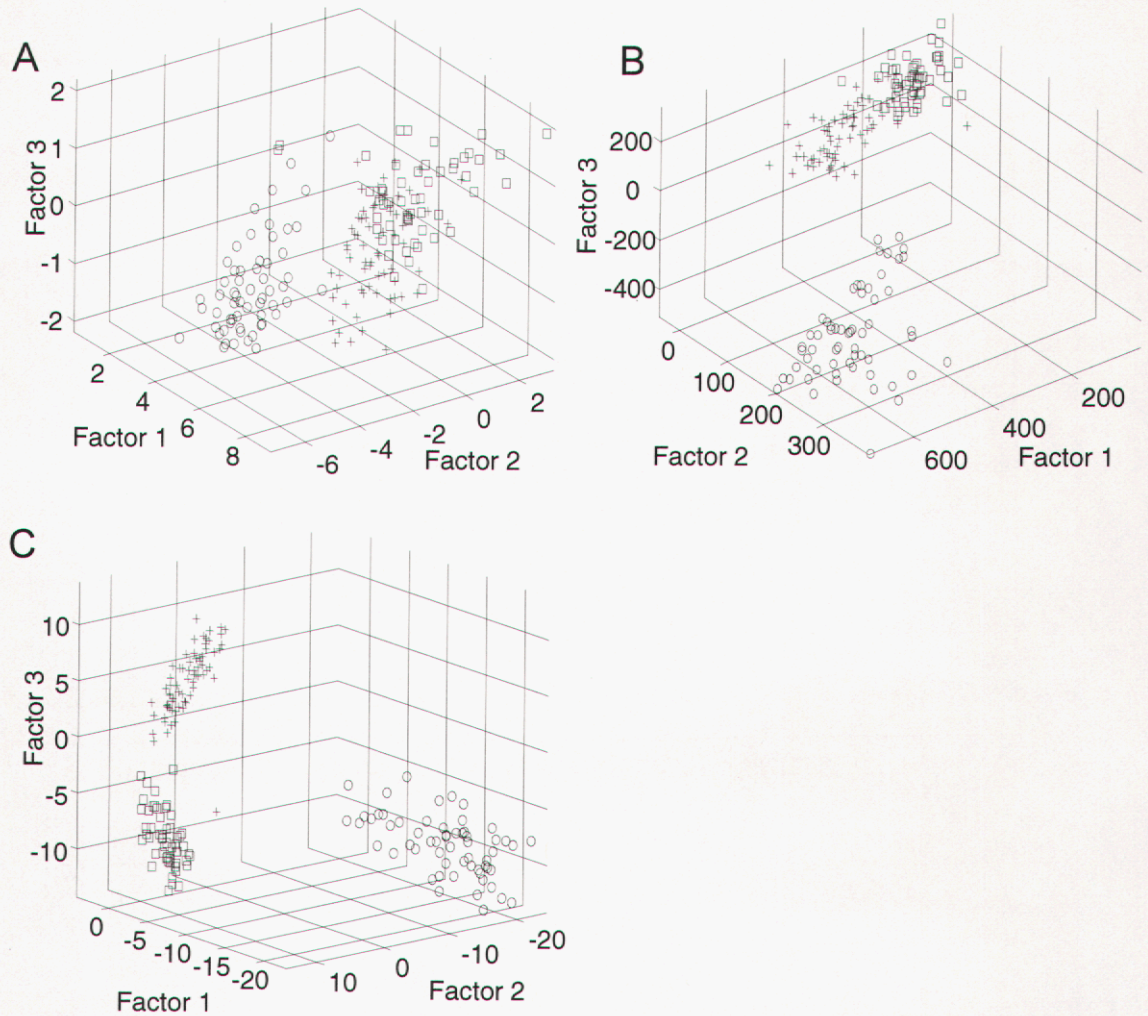

Figure 10. A subset of pixels were isolated using PPI on MNF transformed spectra. The spectra from these pixels were then used in calculating scores with three different techniques. A) PCA scores for factors 1 through 3. B) MNF scores 1 through 3 computed using a central background region of the image to compute the noise covariance estimate. C) MNF scores for factors 1 through 3 computing using the entire image data cube to estimate the noise covariance matrix.

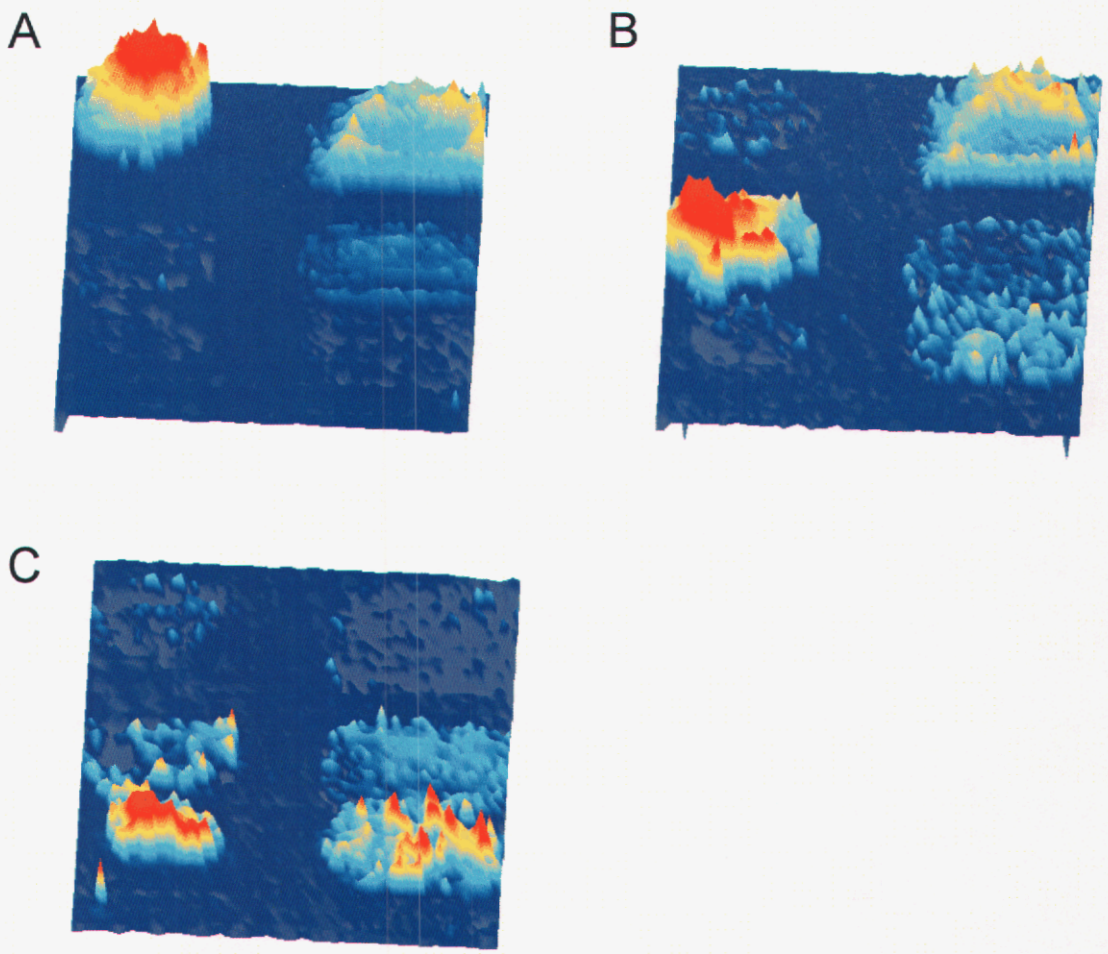

Figure 11. CLS prediction results for pathlength corrected spectra A) yellow component, B) magenta component and C) cyan component.

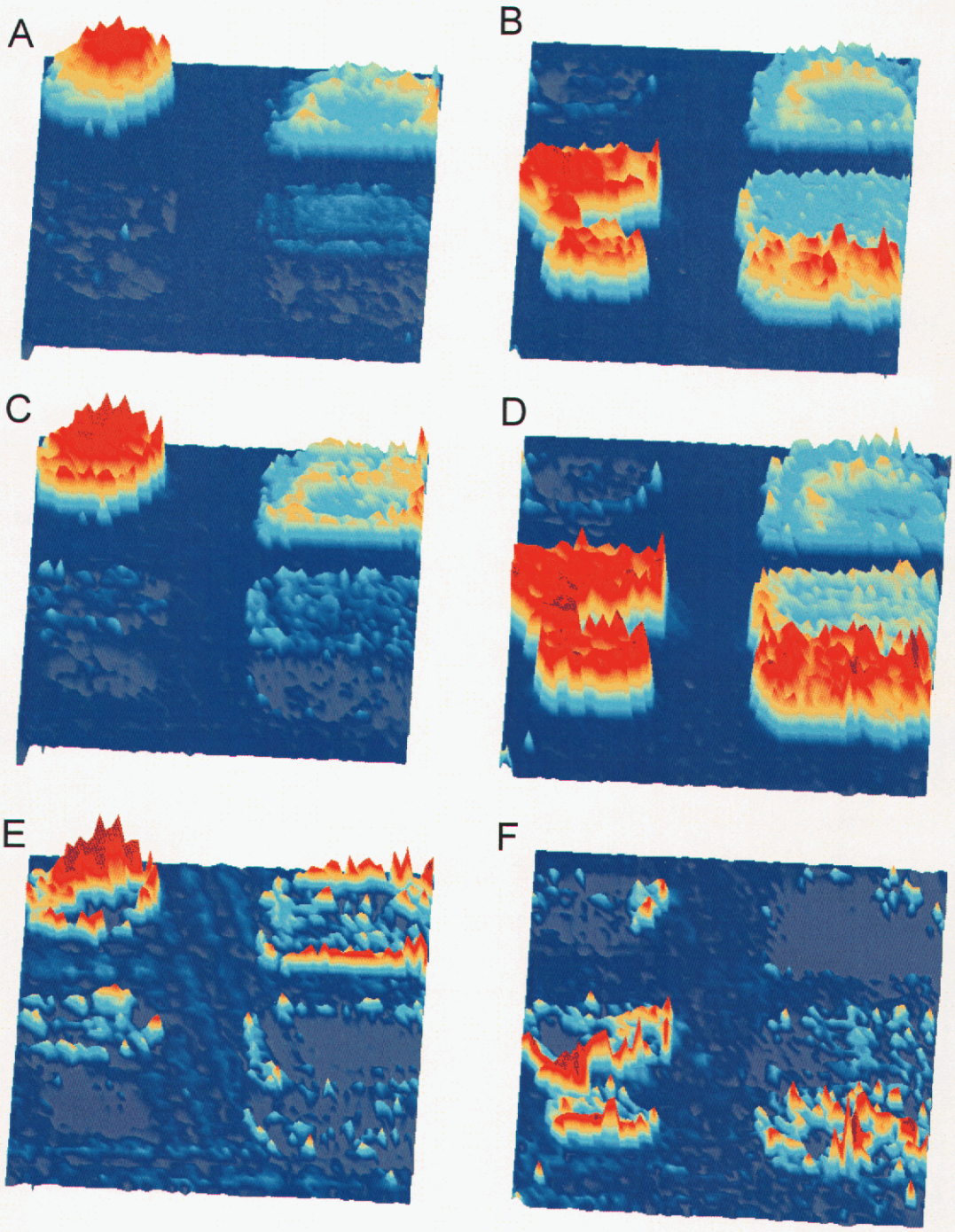

Figure 12. CLS prediction results for pathlength corrected spectra using A) the yellow pure component and B) the combined magenta and cyan pure component. C) Represents PACLS prediction results for the yellow component D) for the combined magenta and cyan component where a chromatic aberration component was included in the model. PACLS prediction results for the chromatic aberration terms for E) yellow and F) combined magenta and cyan.

REFERENCES

[1] E. N. Lewis, P. J. Treado, R. C. Reeder, G. M. Story, A. E. Dowrey, C. Marcott, and I. W. Levin, Anal. Chem. **67**, 3377 (1995).

[2] E. N. Lewis, A. M. Gorbach, C. Marcott. I. W. Levin, Appl. Spectrosc. **50**, 263 (1996).

[3] E. N. Lewis, L. H. Kidder, I. W. Levin, V. F. Kalasinsky, J. P. Hanig, D. S. Lester, Annals of the New York Academy of Sciences **820**, 234 (1997).

[4] E. N. Lewis, L. H. Kidder, J. F. Arens, M. C. Peck, I. W. Levin, Appl. Spec. **51**, 563 (1997).

[5] E. N. Lewis, I. W. Levin, R. A. Crocombe, Mikrochim. Acta **S14**, 589 (1997).

[6] L. H. Kidder, V. F. Kalasinsky, J. L. Luke, I. W. Levin, E. N. Lewis, Nature Medicine **3**, 235 (1997).

[7] L. H. Kidder, I. W. Levin, E. N. Lewis, V. D. Kleiman, E. J. Heilwil, Opt. Lett. **22**, 742 (1997).

[8] C. M. Snively, J. L. Koenig, Macromolecules **32**, 3753 (1998).

[9] C. Marcott, R. C. Reeder, E. P. Paschalis, D. N. Tatakis, A. L. Boskey, R. Mendelsohn, Cellular and Molecular Biology **44**, 109 (1998).

[10] P. Colarusso, L. Kidder, I. W. Levin, J. C. Fraser, J. F. Arens, E. N. Lewis, Appl. Spectrosc. **52**, 106A (1998).

[11] R. Bhargava, S. Q. Wang, J. L. Koenig, Appl. Spectrosc. **52**, 323 (1998).

[12] C. M. Snively, J. L. Koenig, Macromolecules **31**, 3753 (1998).

[13] L. H. Kidder, P. Colarusso, S. A. Stewart, I. W. Levin, N. M. Appel, D. S. Lester, P. G. Pentchev, E. N. Lewis, J. Biomedical Optics **4**, 7 (1999).

[14] R. Bhargava, S. Wang, J. L. Koenig, Macromolecules **32**, 2748 (1999).

[15] R. Bhargava, S. Wang, J. L. Koenig, Appl. Spectrosc. **54**, 1690 (2000).

[16] R. Bhargava, B. G. Wall, J. L. Koenig, Appl. Spectrosc. **54**, 470 (2000).

[17] C. Marcott, G. M. Story, A. E. Dowrey, R. C. Reeder, I. Noda, Mikrochim. Acta **S14**, 157 (1997).

[18] C. Marcott, R. C. Reeder, E. P. Paschalis, D. N. Tatakis, A. L. Boskey, R. Mendelsohn, Cellular and Molecular Biology **44**, 109 (1998).

[19] C. Marcott, R. C. Reeder, J. A. Sweat, D. D. Panzer, D. L. Wetzel, Vib. Spectrosc. **19**, 123 (1999).

[20] B. O. Budevska, Vib. Spectrosc. **24**, 37 (2000).

[21] P. Geladi, P. Hahn, *Multivariate Image Analysis* (John Wiley and Sons, Chichester, 1998).

[22] ENVI 3.1 (Research Systems, Boulder, Colorado).

[23] R. Bhargava, S. Q. Wang, J. L. Koenig, Appl. Spectrosc. **54**, 486 (2000).

[24] A. A. Green, M. Berman, P. Switzer, M. D. Craig, IEEE Trans. Geosci. Remote Sensing **16**, 65 (1988).

[25] J. B. Lee, A. S. Woodyatt, M. Berman, IEEE Trans. Geosci. Remote Sensing **28**, 295 (1990).

[26] P. D. Wentzell, D. T. Andrews, D. C. Hamilton, K. Faber, B. R. Kowalski, J. Chemometrics **11**, 339 (1997).

[27] M. K. Antoon, J. H. Koenig, J. L. Koenig, Appl. Spectrosc. **31**, 518 (1977).

[28] D. M. Haaland, R. G. Easterling, Appl. Spectrosc. **34**, 539 (1980).
[29] D. M. Haaland, R. G. Easterling, Appl. Spectrosc. **36**, 665 (1982).
[30] D. M. Haaland, R. G. Easterling, D. A. Vopicka, Appl. Spectrosc. **39**, 73 (1985).
[31] D. M. Haaland, "Multivariate Calibration Methods Applied to Quantitative FT-IR Analyses," in *Practical Fourier Transform Infrared Spectroscopy*, J. R. Ferraro and K. Krishnan, Eds., (Academic Press, New York, 1989), Chap. 8, pp. 396-468.
[32] D. M. Haaland, "Methods to Include Beer's Law Nonlinearities in Quantitative Spectral Analysis," in *Computerized Quantitative Infrared Analysis*, ASTM Special Technical Publication, G. L. McClure, Ed., STP, Vol. **934**, American Society of Testing Materials, Philadelphia, Pennsylvania, 1987, pp. 78-94.
[33] D. M. Haaland, "Multivariate Calibration Methods Applied to the Quantitative Analysis of Infrared Spectra," in *Computer-Enhanced Analytical Spectroscopy*, Vol. **3**, P. C. Jurs, Ed., (Plenum Press, New York, 1992).
[34] P. Saarinen, J. Kauppinen, Appl. Spectrosc. **45,** 953 (1991).
[35] P. Jaakkola, J. D. Tate, M. Paakkunainen, J. Kauppinen, P. Saarinen, Appl. Spectrosc. **51**, 1159 (1997).
[36] M. Martens, T. Naes, *Multivariate Calibration* (John Wiley and Sons, Chichester, 1989) Chap. 3.6, pp. 166-213.
[37] D. M. Haaland and D. K. Melgaard, Appl. Spectrosc. **54**, 1303 (2000).
[38] D. M. Haaland, R. G. Easterling, Appl. Spectrosc. **34**, 539 (1980).
[29] D. M. Haaland, R. G. Easterling, Appl. Spectrosc. **36**, 665 (1982).
[30] D. M. Haaland, R. G. Easterling, D. A. Vopicka, Appl. Spectrosc. **39**, 73 (1985).
[31] D. M. Haaland, "Multivariate Calibration Methods Applied to Quantitative FT-IR Analyses," in *Practical Fourier Transform Infrared Spectroscopy*, J. R. Ferraro and K. Krishnan, Eds., (Academic Press, New York, 1989), Chap. 8, pp. 396-468.
[32] D. M. Haaland, "Methods to Include Beer's Law Nonlinearities in Quantitative Spectral Analysis," in *Computerized Quantitative Infrared Analysis*, ASTM Special Technical Publication, G. L. McClure, Ed., STP, Vol. **934**, American Society of Testing Materials, Philadelphia, Pennsylvania, 1987, pp. 78-94.
[33] D. M. Haaland, "Multivariate Calibration Methods Applied to the Quantitative Analysis of Infrared Spectra," in *Computer-Enhanced Analytical Spectroscopy*, Vol. **3**, P. C. Jurs, Ed., (Plenum Press, New York, 1992).
[34] P. Saarinen, J. Kauppinen, Appl. Spectrosc. **45,** 953 (1991).
[35] P. Jaakkola, J. D. Tate, M. Paakkunainen, J. Kauppinen, P. Saarinen, Appl. Spectrosc. **51**, 1159 (1997).
[36] M. Martens, T. Naes, *Multivariate Calibration* (John Wiley and Sons, Chichester, 1989) Chap. 3.6, pp. 166-213.
[37] D. M. Haaland and D. K. Melgaard, Appl. Spectrosc. **54**, 1303 (2000).

APPENDIX C.

MULTIVARIATE CURVE RESOLUTION VIA AN ERRORS-IN-VARIABLES MODEL

Edward V. Thomas
Sandia National Laboratories
Albuquerque, NM 87185-0829, U.S.A.

SUMMARY

A new procedure has been developed for multivariate curve resolution. This method assumes that initial estimates of the pure-component spectra are available along with representative spectra from the chemical system. The method re-estimates the pure-component spectra by using the initial estimates, the representative spectra and an errors-in-variables model. Estimates of the component concentrations associated with the representative spectra are also obtained. The errors-in-variables model takes into account the uncertainty of the initial estimates of the pure-component spectra relative to the measurement error of the representative spectra. A family of refined pure-component estimates can be obtained by varying the assumed relative uncertainty of the initial estimates. This method is also well suited to be used in a bootstrap format such that reasonable estimates of the uncertainty in the refined pure-component spectra can be obtained through re-sampling. The method is illustrated with synthetic data and with real data from a hyperspectral image.

KEY WORDS: Bootstrap, Hyperspectral Imaging

1. INTRODUCTION

The purpose of curve resolution methods is to decompose a bilinear data matrix into dimensions that have physical and chemical meaning (see [1], [2], and [3]). Here, the intent is to estimate the pure-component spectra of a system from a *representative* data set without knowledge of the specific components in the system. It is assumed that the number of components is known. In addition, the method that is presented here assumes that some initial estimates of the pure component spectral shapes are available. The relative concentration of any component across samples in the data set can be estimated.

The proposed method re-estimates the pure-component spectra by using the initial estimates, the representative spectra and an errors-in-variables model. The errors-in-variables model takes into account the uncertainty of the initial estimates of the pure-component spectra relative to the measurement error of the representative spectra. The errors-in-variable modeling assumes a certain error structure, which may or not be accurate. Strictly speaking, inferences derived from the errors-in-variables modeling depend on the assumed error structure being accurate. However, even if the assumed error structure is not totally accurate, the errors-in-variables model can be useful.

The remainder of this paper is as follows. First, the underlying theory of the method is presented. Following the theoretical discussion, the method is illustrated in two hyperspectral imaging contexts (one with synthetic data where truth is known and the other with laboratory data). A MATLAB script implementing the method is presented to the reader in an appendix.

2. THEORY

The basis for the proposed method is the use of an errors-in-variables model to represent the prediction phase during multivariate calibration (see [4], [5], and [6]). To begin, assume that there are $n \geq 1$ independent measured spectra that are representative of the system with p components and q wavelengths. We consider the idealized causal model $\boldsymbol{Y}_0 = \boldsymbol{B}_0 \cdot \boldsymbol{X}_0$, where $\boldsymbol{X}_0$ represents the $p \times n$ matrix of component concentrations, $\boldsymbol{B}_0$ represents the $q \times p$ matrix of true pure component spectra, and $\boldsymbol{Y}_0$ represents the unobserved set of idealized spectra (measured without error) corresponding to the component concentrations in $\boldsymbol{X}_0$. Collectively, the measured spectra are denoted by $\boldsymbol{Y}$, where $\boldsymbol{Y} = \boldsymbol{Y}_0 + \boldsymbol{\Delta Y}$ with $\boldsymbol{\Delta Y}$ representing the spectral measurement error. We also assume that there exists a prior estimate of $\boldsymbol{B}_0$ given by $\boldsymbol{B}$. The relationship between $\boldsymbol{B}_0$ and $\boldsymbol{B}$ is given by $\boldsymbol{B} = \boldsymbol{B}_0 + \boldsymbol{\Delta B}$, where $\boldsymbol{\Delta B}$ represents the error in estimating $\boldsymbol{B}_0$.

The proposed method uses $\boldsymbol{B}$, $\boldsymbol{Y}$, and the assumed distribution of the errors in $\boldsymbol{B}$ and $\boldsymbol{Y}$ ($\boldsymbol{\Delta B}$ and $\boldsymbol{\Delta Y}$) to construct an improved estimate of $\boldsymbol{B}_0$. For purposes of developing this method we will make some additional assumptions regarding the relative uncertainties in $\boldsymbol{B}$ and $\boldsymbol{Y}$.

In order to proceed it is useful to cast this process into the framework of a linear functional model where errors in both $\boldsymbol{Y}$ and $\boldsymbol{B}$ are considered and where $\boldsymbol{X}_0$ and $\boldsymbol{B}_0$ are considered as parameters to be estimated (see [7]). The errors in $\boldsymbol{Y}$ in $\boldsymbol{B}$ are grouped together in the $q \times (n+p)$ matrix $\boldsymbol{E} = [\boldsymbol{\Delta Y}\ \boldsymbol{\Delta B}]$. We assume that the rows of $\boldsymbol{E}$ are independent and identically distributed multivariate normal with mean zero and covariance $\boldsymbol{\Sigma} = \sigma^2 \boldsymbol{\Omega}$. It is assumed that $\boldsymbol{\Sigma}$ is known to within a scalar factor (see [4], [5], and [6]). Let the tth row of each of $\boldsymbol{Y}$, $\boldsymbol{Y}_0$, $\boldsymbol{B}$, and $\boldsymbol{B}_0$ be given by $\boldsymbol{y}_t$, $\boldsymbol{y}_{0t}$, $\boldsymbol{b}_t$, and $\boldsymbol{b}_{0t}$, respectively.

Given the assumed distribution of the errors, the maximum likelihood estimates (MLEs) of $\boldsymbol{X}_0$ and $\boldsymbol{B}_0$ are obtained by maximizing the log likelihood,

$$-\frac{q}{2} \cdot \log\left|2\pi\,\sigma^2\,\boldsymbol{\Omega}\right| - \left(2\sigma^2\right)^{-1} \sum_{t=1}^{q} \left(\left(\boldsymbol{y}_t, \boldsymbol{b}_t\right) - \left(\boldsymbol{y}_{0t}, \boldsymbol{b}_{0_t}\right)\right) \boldsymbol{\Omega}^{-1} \left(\left(\boldsymbol{y}_t, \boldsymbol{b}_t\right) - \left(\boldsymbol{y}_{0t}, \boldsymbol{b}_{0_t}\right)\right)^T,$$

with respect to $\boldsymbol{X}_0$ and $\boldsymbol{B}_0$ (see [7], Chapter 4). Let $\lambda_1 \geq \lambda_2 \geq \ldots \geq \lambda_{p+n}$ be the eigenvalues of $\boldsymbol{\Omega}^{-1/2}\,\boldsymbol{M}\,\boldsymbol{\Omega}^{-1/2}$ and let $\boldsymbol{G} = [\boldsymbol{G}_1\ \boldsymbol{G}_2]$ be the matrix of corresponding orthonormal

eigenvectors such that $\Omega^{-1/2} M \Omega^{-1/2} G_2 = G_2 \Lambda$, where $M = q^{-1} \sum_{t=1}^{q} S_t^T S_t$, $S_t = (y_t\ b_t)$, $\Lambda = \text{diag}(\lambda_{p+1}, \lambda_{p+2}, \ldots, \lambda_{p+n})$, and $\Omega^{-1/2}$ is the matrix square root of Ω^{-1}. Further, let $D = \Omega^{-1/2} G_2$.

The maximum likelihood estimator of X_0 is $\tilde{X}_0 = -D_{pn} D_{nn}^{-1}$, where D_{nn} consists of the first n rows of D, while D_{pn} consists of the last p rows of D. $\tilde{X}_0$ is the estimate of component concentrations associated with the n independent spectra.

The maximum likelihood estimator of B_0, $\tilde{B}_0$, is given by the last p columns of $S \cdot \left(I_{n+p} - D \cdot D^T \cdot \Omega\right)$, where S_t is the t^{th} row of S. The columns of $\tilde{B}_0$ are the re-estimated pure-component spectra.

In practice, one might have initial estimates of the pure-component spectra, B, that are inaccurate in terms of scale, yet are accurate in terms of shape. In such cases, there is a scale ambiguity that will affect both $\tilde{X}_0$ and $\tilde{B}_0$. Thus, the estimated concentrations of a given component across a row of $\tilde{X}_0$ should be considered on a relative basis only. Furthermore, the columns of $\tilde{B}_0$ will represent only the *shapes* of the pure component spectra.

For a fixed set of observables (Y and B), the estimation procedure depends entirely on the selection of Ω, which summarizes the assumed relative uncertainties of the elements within Y and B. In general, Ω has the form, $\Omega = \begin{bmatrix} \Omega_{YY} & \Omega_{YB} \\ \Omega_{BY} & \Omega_{BB} \end{bmatrix}$. If we assume no correlation between the elements of ΔY and ΔB, then Ω reduces to $\Omega = \begin{bmatrix} \Omega_{YY} & 0 \\ 0 & \Omega_{BB} \end{bmatrix}$, where Ω_{YY} is nxn and Ω_{BB} is pxp. In general, this method will allow Ω_{YY} and Ω_{BB} to take the form of any regular covariance matrix. One possibility (that we will use here) is to let $\Omega_{YY} = I_n$ and $\Omega_{BB} = k \cdot I_p$, in which case $\Omega = \begin{bmatrix} I_n & 0 \\ 0 & k \cdot I_p \end{bmatrix}$. In the illustrative examples, families of pure-component spectra are developed by varying k. It is assumed that the variance of each row of E (i.e. wavelength) has an identical error structure. Furthermore, it is assumed that the rows of E are independent. It may be necessary to transform Y (see [4]) in order to produce E with these characteristics. Note also that Ω might also have a special structure when B is obtained from a separate calibration study (see [4], [5], and [6]).

Suppose that the initial estimates of the pure-component spectra, $\boldsymbol{B}$, are accurate in terms of scale and the distributional assumptions regarding $\boldsymbol{E}$ are accurate. Then, the errors-in-variables estimation procedure described above will lead to valid inferences concerning $\boldsymbol{X}_0$ and $\boldsymbol{B}_0$ (see [4], [5], [6], and [7]). In fact, it can be shown that the estimates of $\boldsymbol{X}_0$ and $\boldsymbol{B}_0$ will converge to their respective true values without the assumption of normality (see [7]). In practice, it is unlikely that we will have perfect knowledge of $\boldsymbol{\Omega}$. Nevertheless, the proposed estimation method can provide useful estimates of $\boldsymbol{X}_0$ and $\boldsymbol{B}_0$.

To summarize, the proposed method consists of estimating the pure component spectra associated with a chemical system where there are viable prior estimates of the pure component spectra. The prior estimates could be based on subject-matter knowledge, an earlier calibration experiment, or from a preliminary analysis of the current data ($\boldsymbol{Y}$) using a method like SIMPLISMA [3]. One must also provide some assessment of the uncertainties of the prior estimates relative to the noise in $\boldsymbol{Y}$. The final estimates of the pure-component spectra depend on the quality of the prior estimates as well as estimates of the relative uncertainties of $\boldsymbol{Y}$ and $\boldsymbol{B}$. It is implicitly assumed that that the dimension of the chemical system is known and represented by the column dimension (p) of $\boldsymbol{B}$. The proposed method does not involve *non-negativity* constraints. As is the case of applying other existing curve resolution methods, the proposed method is sensitive to the correlation pattern among components in $\boldsymbol{X}$ as well as similarities among the pure-component shapes. Appendix 1 contains a MATLAB SCRIPT for performing this MLE-based Curve Resolution

3. ILLUSTRATIVE EXAMPLES

Here, the proposed method will be applied in two different situations. In the first situation, we simulate a hyperspectral image with known spectral shapes and Beer's Law. The second situation involves a hyperspectral image of an aged neoprene specimen.

3.1 Simulated Hyperspectral Image

For this example, we constructed a hyperspectral image consisting of the mixture spectra of three components that vary spatially in concentration over a surface. The image consists of a 16x16 array of pixels with 100 spectral channels. The signal portion of the image ($\boldsymbol{Y}_0$) is assumed to follow Beer's Law. The observed image ($\boldsymbol{Y}$) consists of this signal plus independent Gaussian errors with mean zero and standard deviation of $1\text{x}10^{-6}$. Figure 1 presents the true pure-component spectra ($\boldsymbol{B}_0$) that are used in this simulation. Figure 2 presents the initial estimates of these pure-component spectra (possibly obtained by an earlier calibration experiment with low signal to noise). Figure 3 presents the spatial distribution of the concentrations ($\boldsymbol{X}_0$) of each of the three components (labeled A, B, and C). By construction, the pairwise correlation of component concentrations is zero. For this simulation it is known that $\boldsymbol{\Omega} = \begin{bmatrix} \boldsymbol{I}_n & \boldsymbol{0} \\ \boldsymbol{0} & k \cdot \boldsymbol{I}_p \end{bmatrix}$, where $k = 5$.

The procedure described in Section 2 was applied to the simulated hyperspectral image by using $\boldsymbol{\Omega} = \begin{bmatrix} \boldsymbol{I}_n & \boldsymbol{0} \\ \boldsymbol{0} & 5 \cdot \boldsymbol{I}_p \end{bmatrix}$. Figure 4 presents the final pure-component estimates (columns of $\widetilde{\boldsymbol{B}}_0$). Figure 5 presents the difference between these estimates and the true pure component spectra. Note that this figure shows some "non-white-noise" error structure that is a consequence of $\boldsymbol{\Delta B}$ and $\boldsymbol{\Delta Y}$ interacting with $\boldsymbol{X}_0$ and $\boldsymbol{B}_0$ in a complex way. Note that something comparable to curves in Figure 4 could not be obtained by simply "smoothing" the curves in Figure 2. For example, underlying sharp features of the "true curves" would tend to be under-estimated as both the signal and noise would be smoothed.

Figures 6 and 7 present a 3D perspective of the estimated concentrations and associated errors for each component. The errors displayed in Figure 7 are a consequence of the errors in $\widetilde{\boldsymbol{B}}_0$.

In this particular simulation context the effect of perturbing k within the range from .5 to 50 on the final pure-component estimates is minimal. In the limit as $k \to 0$, the final pure component estimates are unchanged from the initial estimates since the data in $\boldsymbol{Y}$ have zero relative weight in influencing the final estimates. Conversely, as $k \to \infty$ more and more emphasis is given to $\boldsymbol{Y}$. Another way to look at it is as follows. In the limit as $k \to 0$, a particular realization of $\boldsymbol{\Delta Y}$ has no effect on $\widetilde{\boldsymbol{B}}_0$. On the other hand, as $k \to \infty$ a particular realization of $\boldsymbol{\Delta Y}$ can have an enormous effect on $\widetilde{\boldsymbol{B}}_0$. In practice, if one does not have a good idea for an appropriate value of k, it may to do the analysis with a range of values for k.

Uncorrelated rows of $\boldsymbol{X}_0$ are helpful for estimating $\boldsymbol{B}_0$. In cases where the components are correlated, there will be some negative effect on performance. To demonstrate this, consider a slight modification of the earlier simulation such that $\boldsymbol{B}_0$, $\boldsymbol{\Delta B}$, and $\boldsymbol{\Delta Y}$ are unchanged. The third row of $\boldsymbol{X}_0$ is modified such that the levels of components B and C are highly correlated over the image surface (see Figure 8). The signal portion of the image ($\boldsymbol{Y}_0$) is defined by $\boldsymbol{B}_0$ and the new version of $\boldsymbol{X}_0$. Upon applying the MLE procedure to $\boldsymbol{B}$ and the resulting $\boldsymbol{Y}$ (i.e. $\boldsymbol{Y} = \boldsymbol{Y}_0 + \boldsymbol{\Delta Y}$) with the appropriate value of k (k=5), the final pure component estimates illustrated in Figure 9 were obtained. Note the inverse correlation between the fine structures of the green curve (component B) and the red curve (component C). This symptom, directly a consequence of the correlation across rows of $\boldsymbol{X}_0$, is a problem for any curve resolution method. That is, the correlation of components across the image confounds the estimated pure component spectra of the involved components. In general, there isn't a way around this difficulty without experimental control of the component levels across spectra used for curve resolution.

3.2 Aged Neoprene Image

In this example, the sample consists of a microtomed section of aged neoprene that was produced as part of a polymer aging study. The spectral image covers a 4mm by 4mm region and consists of 4096 pixels (or spectra). The image was reduced to 1454 spectra. The spectra ('spectra6np' obtained from Fred Koehler) were windowed and baseline corrected. After windowing, the spectral dimension was reduced to 194. For this purpose it was assumed that there are three fundamental sources of spectral variation. Note, however, that it is clear (via an analysis of the distribution of the eigenvalues of $Y^T Y$) that there are many other sources of variation. Two standard curve resolution methods (MCR [1] and SIMPLISMA [3]) were then applied to the spectral. The resulting curves ('purspec6np' for Simplisma and 's6npnn' for MCR obtained from Fred Koehler) were used as the initial estimates of the pure components for the proposed MLE method. Note that (like in the case of the proposed method) MCR requires an initial estimate of the pure components, whereas SIMPLISMA does not. In the case of MCR, the initial estimates were supplied by SIMPLISMA.

The proposed MLE method was implemented in the following ways. First, in order to hasten the computation associated with applying the proposed method, the image was reduced to100 spectra by randomly sampling the available 1454 spectra. The output pure component estimates from SIMPLISMA or MCR were used as the initial estimates of the pure component spectra were for the MLE method. For the first implementation of the MLE with these spectra we let $\boldsymbol{\Omega} = \begin{bmatrix} \boldsymbol{I}_n & \boldsymbol{0} \\ \boldsymbol{0} & k \cdot \boldsymbol{I}_p \end{bmatrix}$, with $k = 1$. Figures 10,11, and 12 exhibit the estimates of the pure components (averaged over 10 independent realizations of sample spectra) obtained by both versions of the MLE along with the pure components obtained SIMPLISMA and MCR. It is interesting to note that the MLE estimates (given SIMPLISMA as initial estimates) are significantly different than the SIMPLISMA estimates. The MLE estimates (given MCR as initial estimates) are relatively close to the MCR estimates. This suggests a *close kinship* between the MCR and MLE procedures. On the other hand, there are some notable differences between MCR and MLE (given SIMPLISMA). This comparison is interesting since both methods start with the SIMPLISMA estimates.

It is also interesting to consider the effects of using different values for k in this context since we really don't have solid information regarding the uncertainties in the spectra relative to those in the initial estimates. Figures 13-15 provide some idea regarding the sensitivity of the resulting estimates to the value of k. In these cases, the results pertain to the situation where the MLE method was used with the same set of 100 random spectra and when SIMPLISMA provided the initial pure component estimates for values of k spanning 2 decades (k = .1, 1, 10). Note that there are only minor changes in the pure component estimates across theses different conditions for k.

For large values of k, the final estimates may depend more significantly on the particular realization of $\Delta \boldsymbol{Y}$. To see this consider the case where three different random sets of 100

spectra are used with the MLE method with $k = 10$. Figures 16-18 illustrate the variability in the MLE estimates over these three different random sets. Thus, at least in this context, the variability induced by varying the set of spectra is more important than the choice of k.

This re-sampling process could be extended to establish "bootstrap confidence limits" for the pure component spectra. Figures 19 and 20 illustrate the approach. MLE estimates of the three components were obtained for each of one hundred different random sets of 100 spectra. The estimates associated with the first component are displayed in Figure 19. For each channel the 100 estimates were sorted and the 5^{th} smallest and largest values were saved. These 5^{th} and 95^{th} percentiles of the estimated pure component spectra delimit 90% bootstrap confidence intervals for the "true" pure component and are displayed in Figure 21. Of course, this inference is subject to the validity of a number of assumptions: such as an underlying linear model and an appropriate value for k.

4. CONCLUSIONS

The proposed method for curve resolution requires representative spectra of the chemical system, knowledge of the dimension of the chemical system, a preliminary estimate of the underlying pure components, as well some knowledge about the relative uncertainty of the preliminary estimates. With this method one can easily produce a family of pure component estimates by varying the relative uncertainty parameter k. Through the covariance matrix, $\boldsymbol{\Omega}$, this method allows for a very flexible characterization of the relative uncertainties of the preliminary estimates that is not fully discussed here. Finally, as is the case with any other curve resolution method, the proposed method produces estimates that depend on the correlation of components across the 'representative spectra.'

5. REFERENCES

1. R. Tauler, B. Kowalski, and S. Fleming, *Anal. Chem.*, **65**, 2040 (1993).
2. R. Tauler, A. Smilde, and B. Kowalski, *J. Chemometrics*, **9**, 31 (1995).
3. W. Windig and J. Guilment, *Anal. Chem.*, **63**, 1425 (1991).
4. E. V. Thomas, *Technometrics*, **33**, 405-413 (1991).
5. E. V. Thomas, in *Recent Advances in Total Least Squares Techniques and Errors-in-Variables Modeling*, ed. by S. Van Huffel, p. 359, SIAM, Philadelphia (1997).
6. E. V. Thomas, 'Simultaneous inference in multivariate calibration', *Sandia National Laboratories Technical Report SAND94-2642* (1994).
7. W. A. Fuller, *Measurement Error Models*, John Wiley, New York (1987).

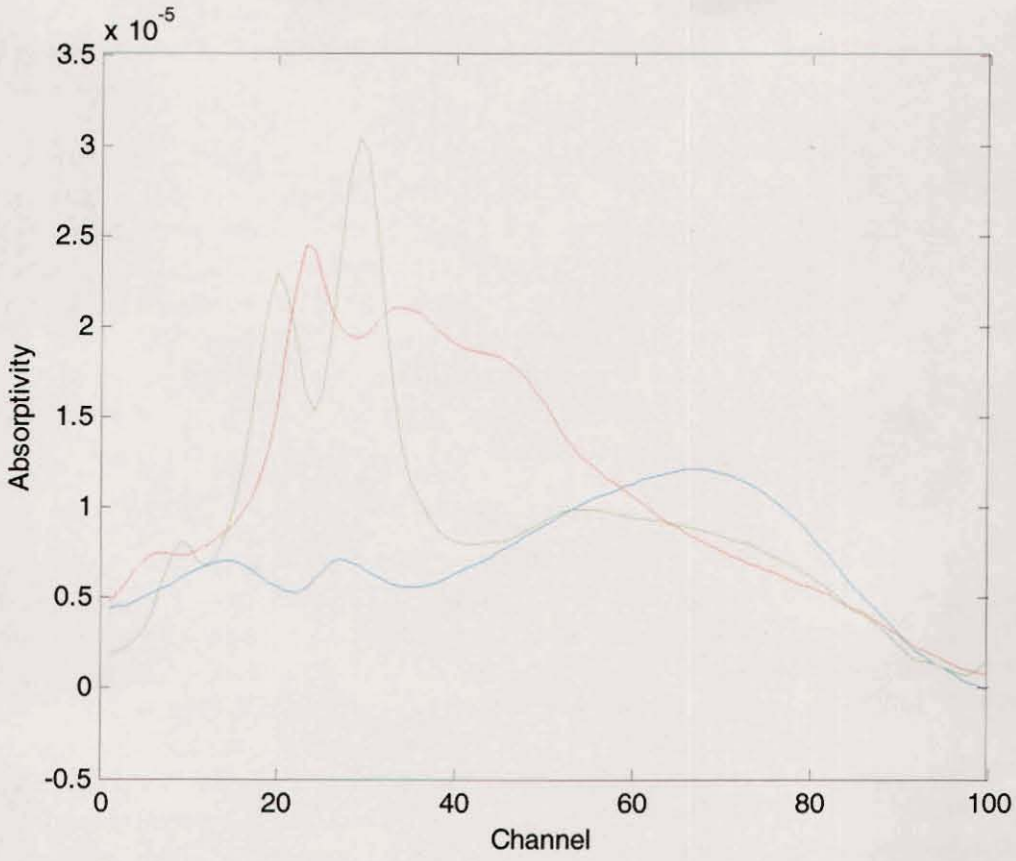

Figure 1 – True Pure Component Spectra

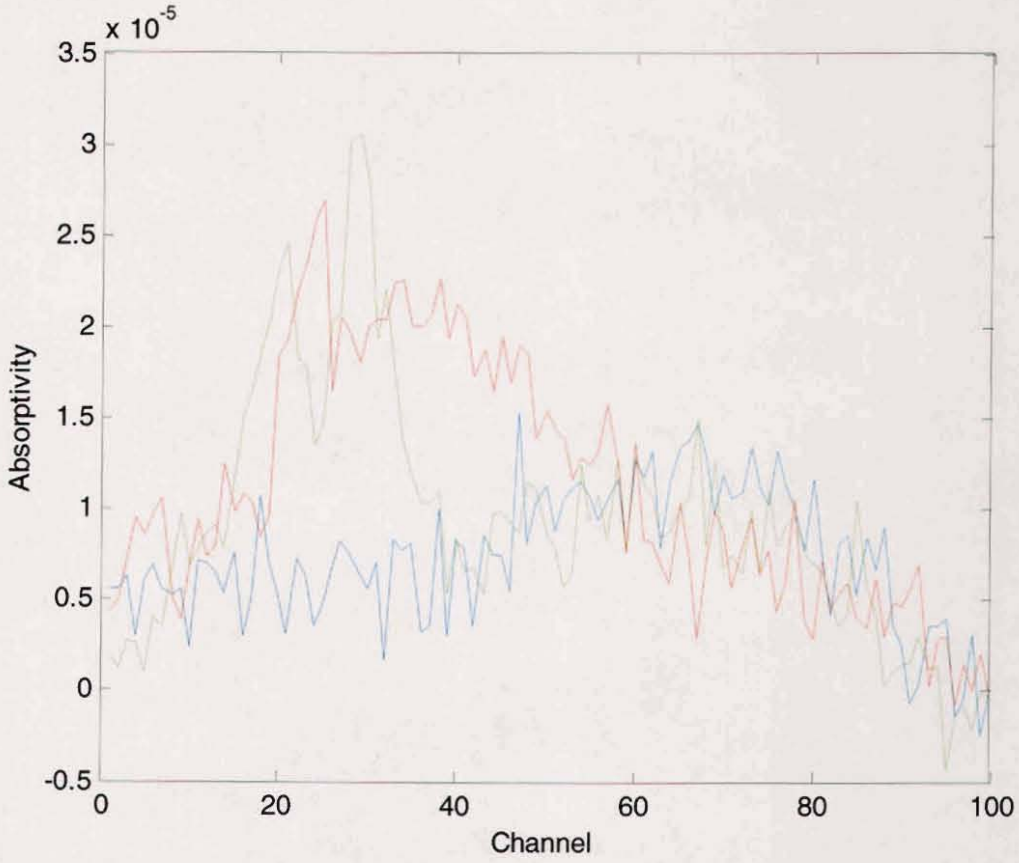

Figure 2 – Initial Estimates of Pure Component Spectra

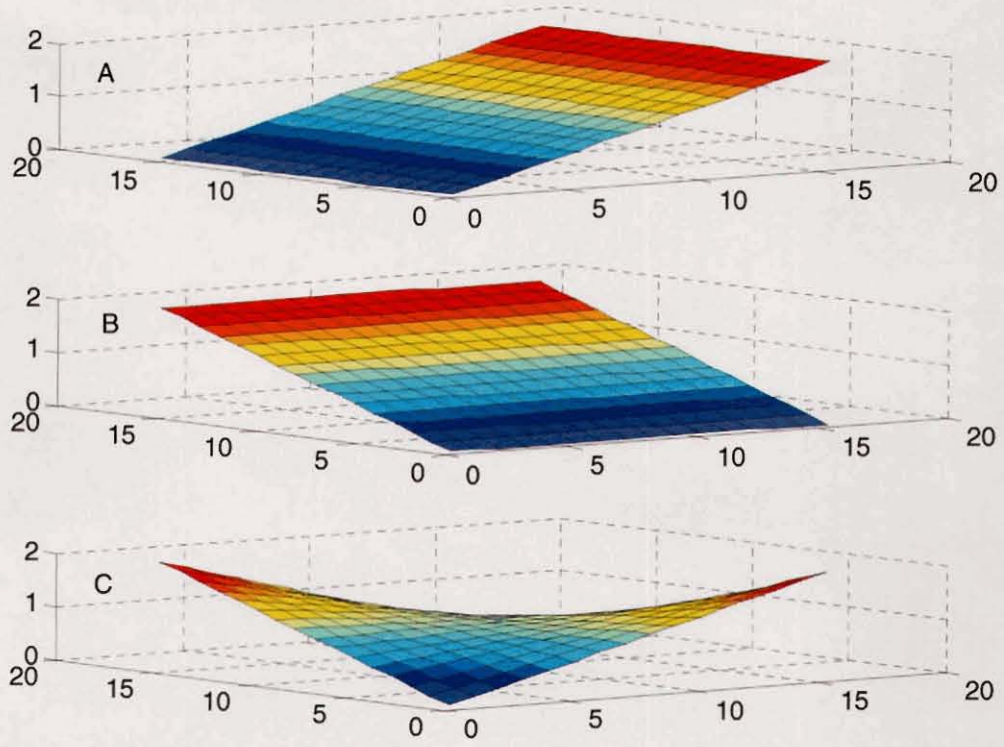

Figure 3 – Concentration Levels of Components (X_0) versus Space

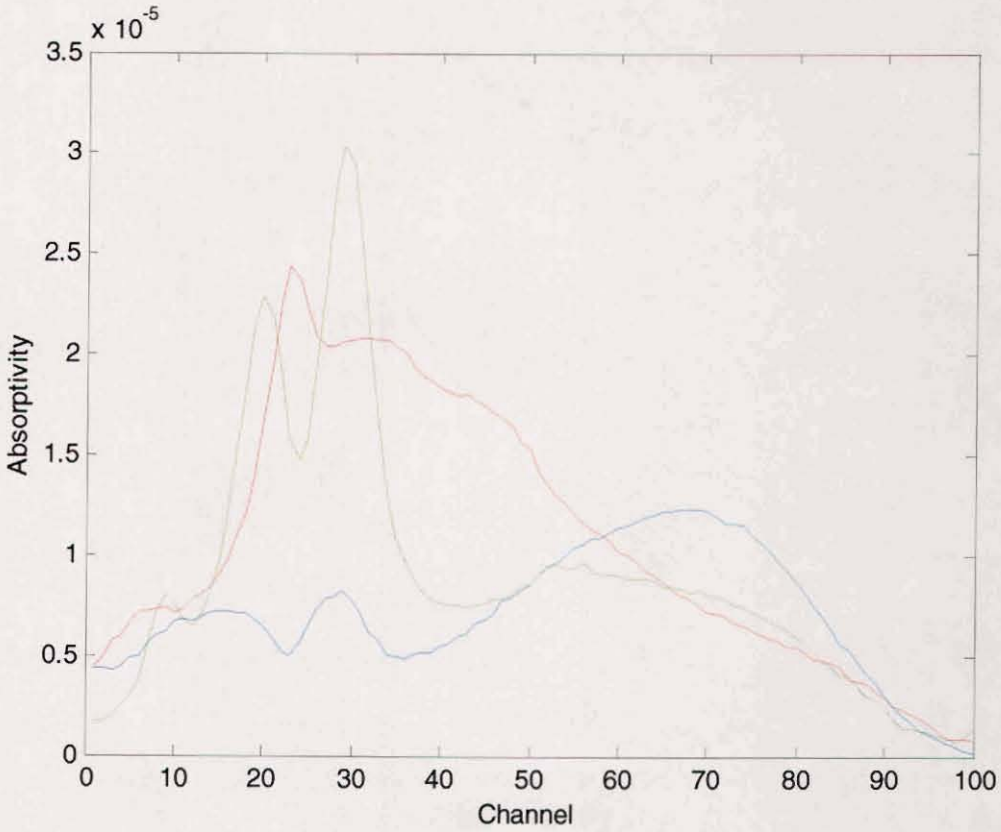

Figure 4 – Final Estimates of Pure Component Spectra

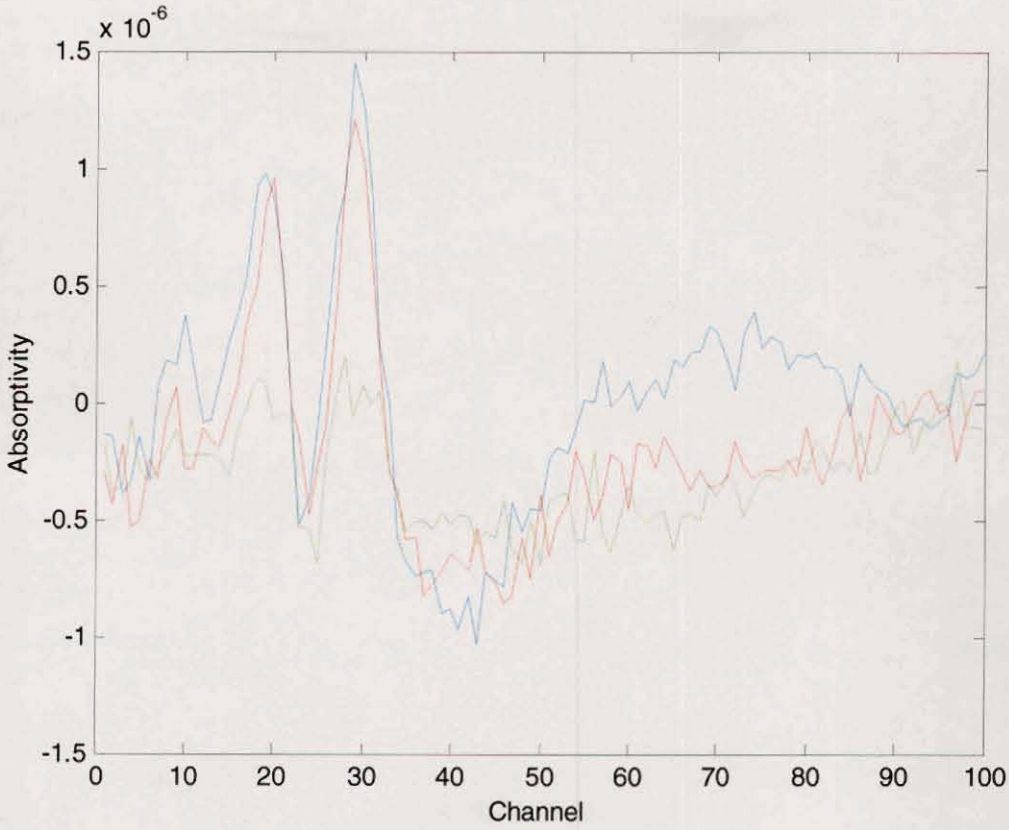

Figure 5 – Errors in Estimated Pure-Component Spectra

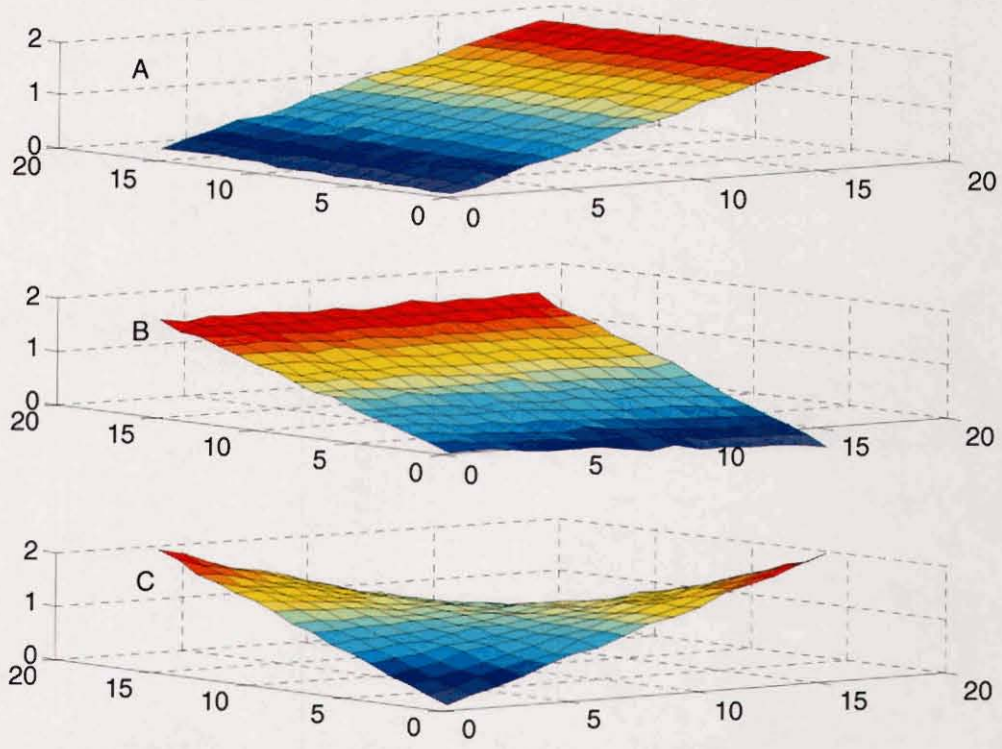

Figure 6 – Estimated Concentration Levels of Components versus Space

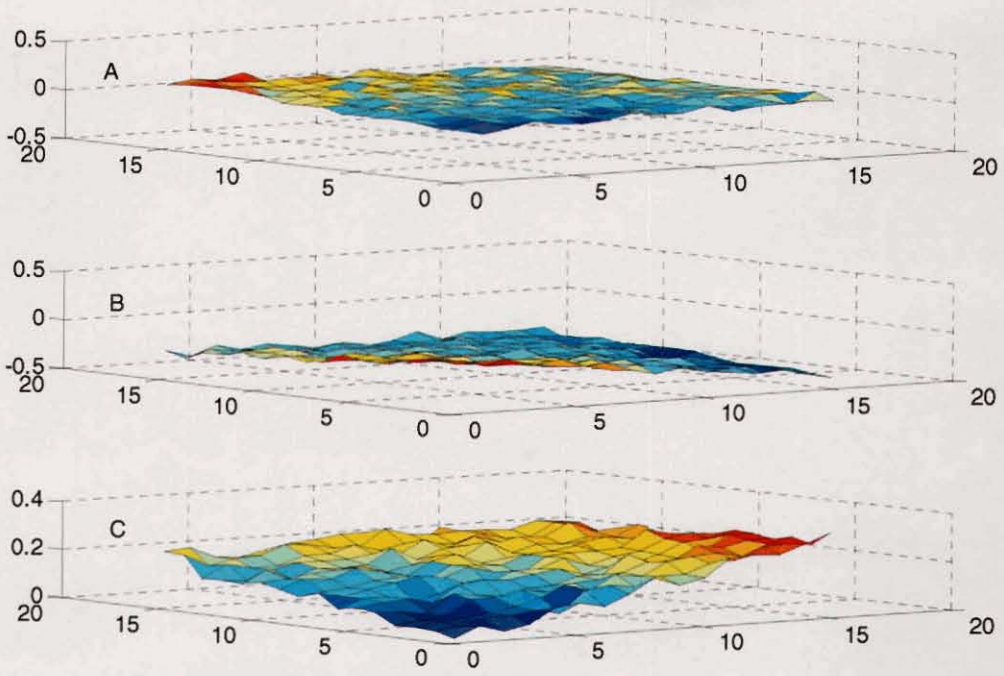

Figure 7 – Errors in Estimated Concentration versus Space

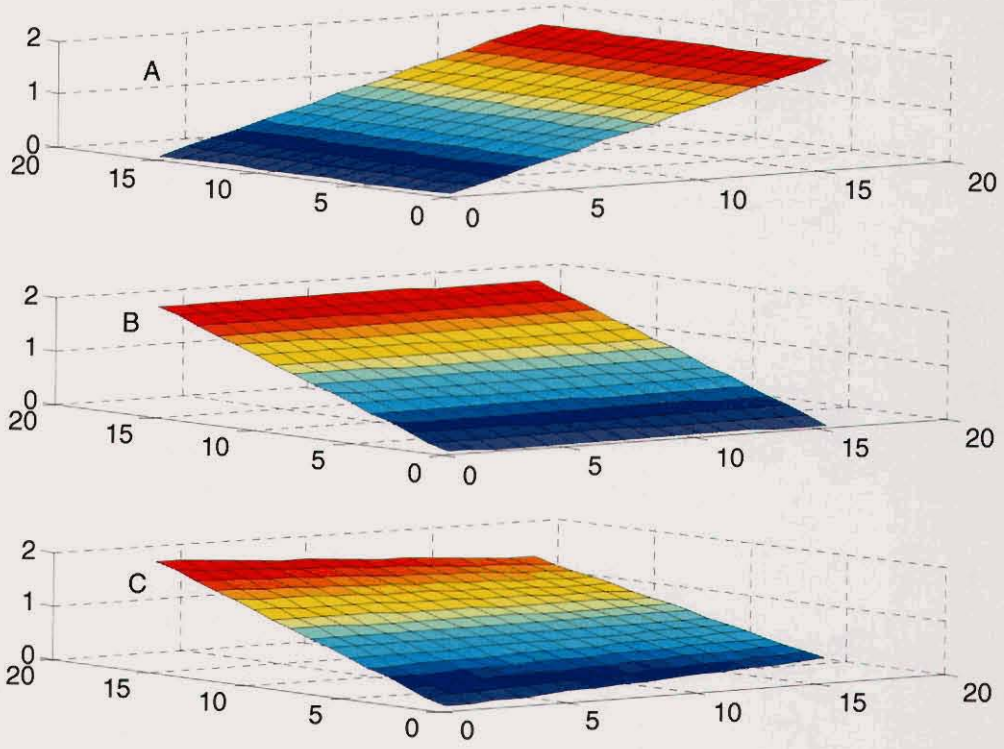

Figure 8 – Concentration of Components versus Space, Correlated Rows of X_0

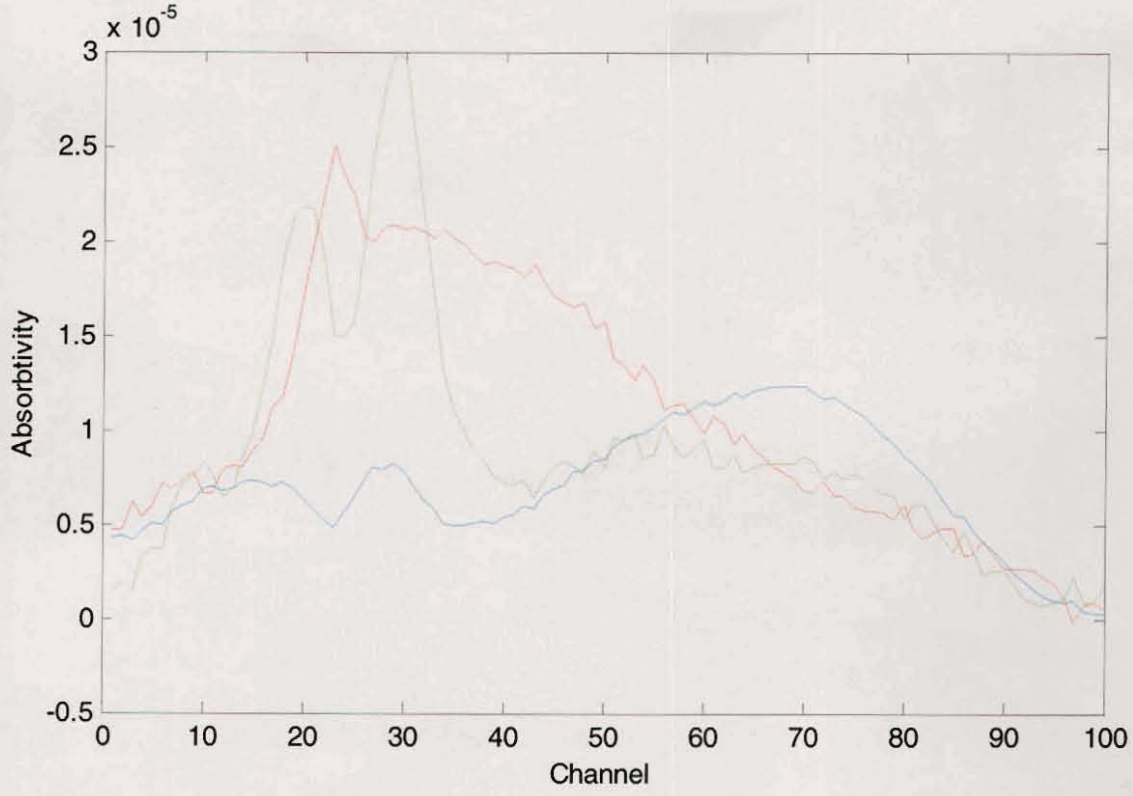

Figure 9 – Final Estimates of Pure Component Spectra, Correlated Rows of X_0

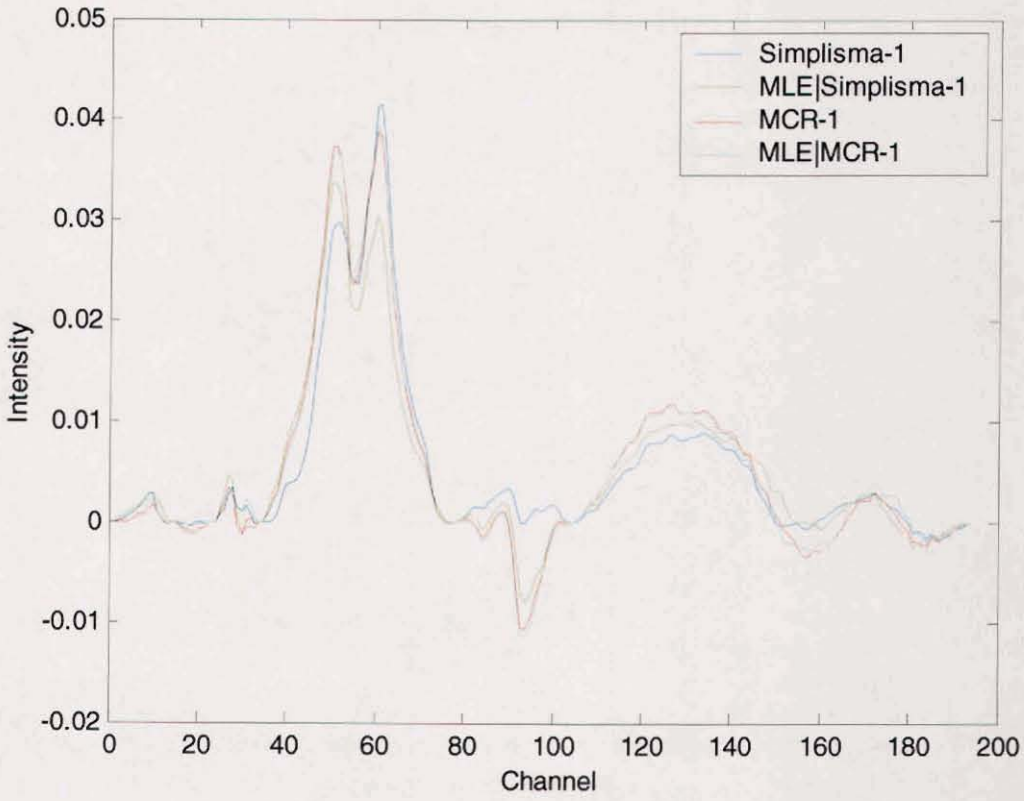

Figure 10 – Estimates of Spectrum of First Component: SIMPLISMA, MCR, MLE|SIMPLISMA, MLE|MCR|

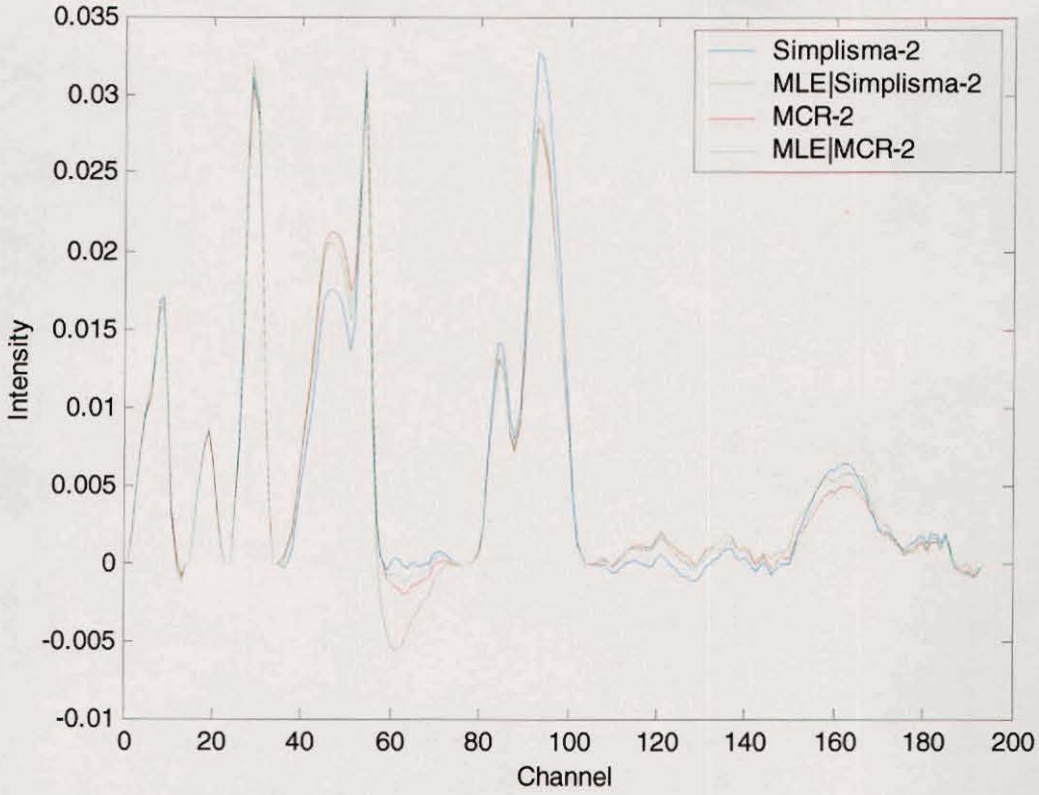

Figure 11 – Estimates of Spectrum of Second Component: SIMPLISMA, MCR, MLE|SIMPLISMA, MLE|MCR|

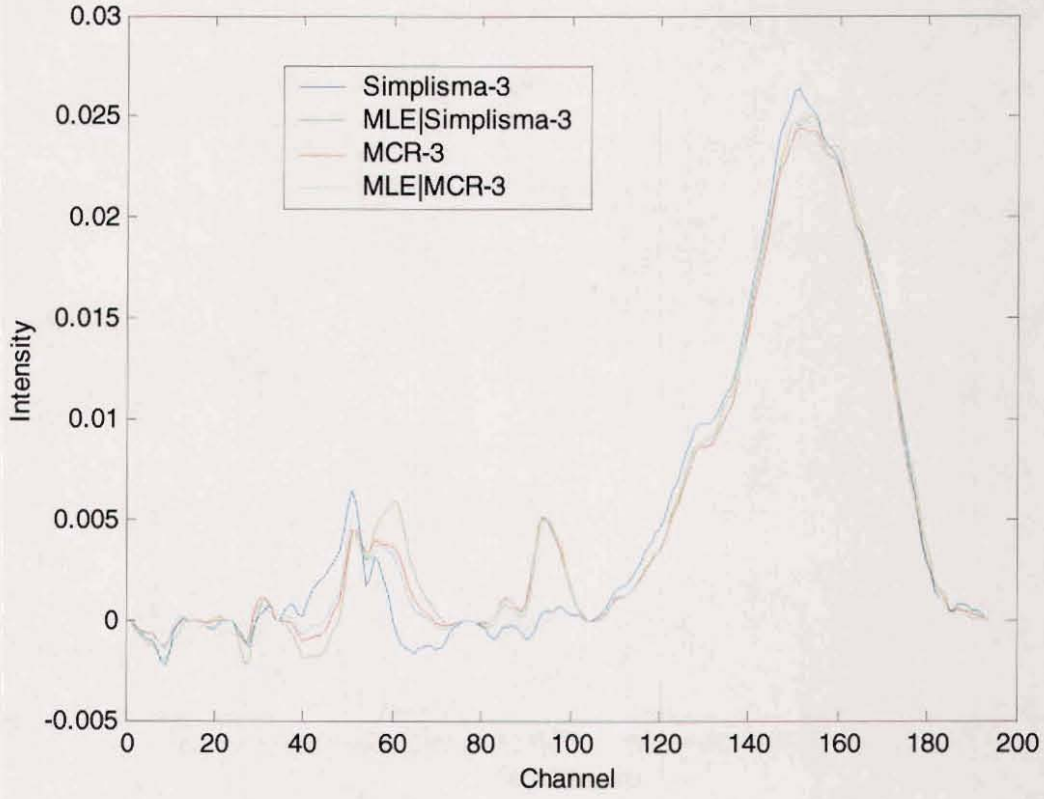

Figure 12 – Estimates of Spectrum of Third Component: SIMPLISMA, MCR, MLE|SIMPLISMA, MLE|MCR|

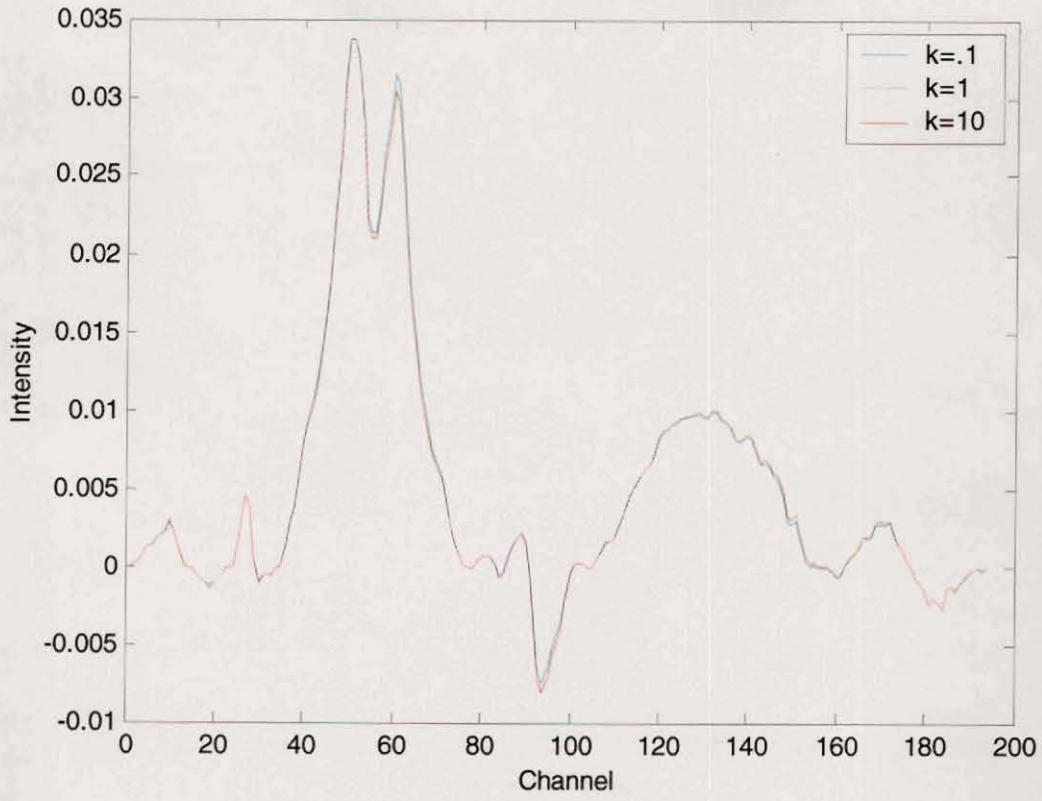

Figure 13 – MLE Estimates of Spectrum of 1st Component (SIMPLISMA Prior)
$k = .1, 1, 10$

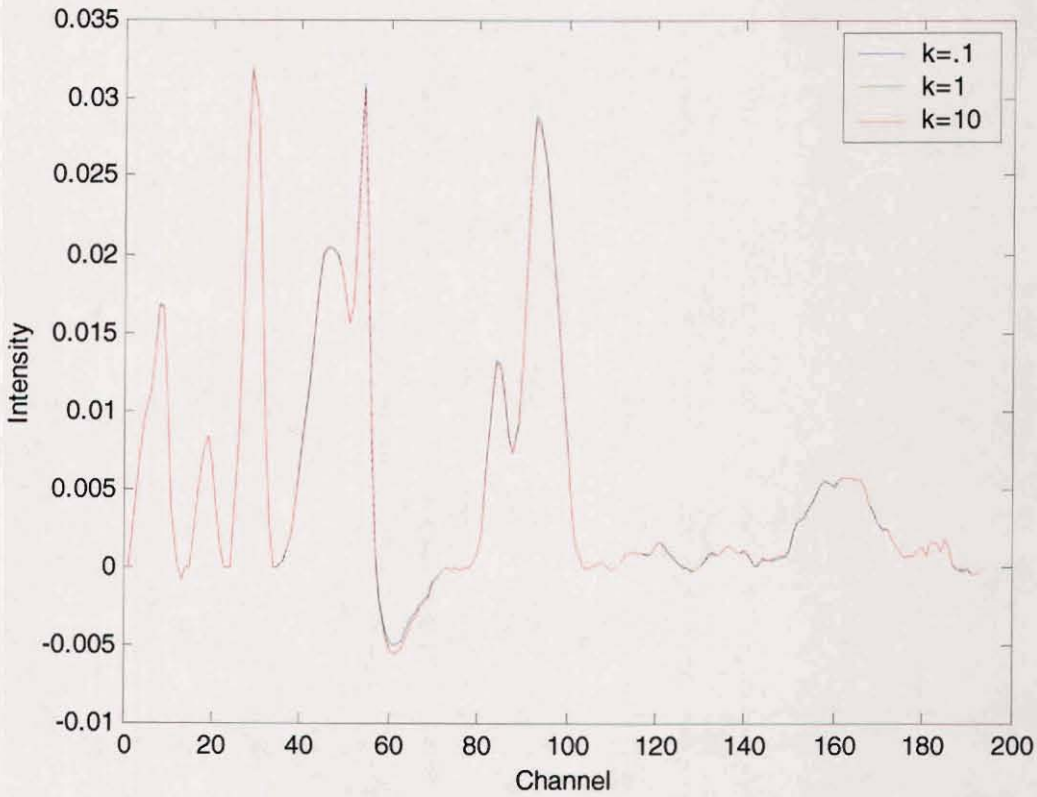

Figure 14 – MLE Estimates of Spectrum of 2nd Component (SIMPLISMA Prior)
$k = .1, 1, 10$

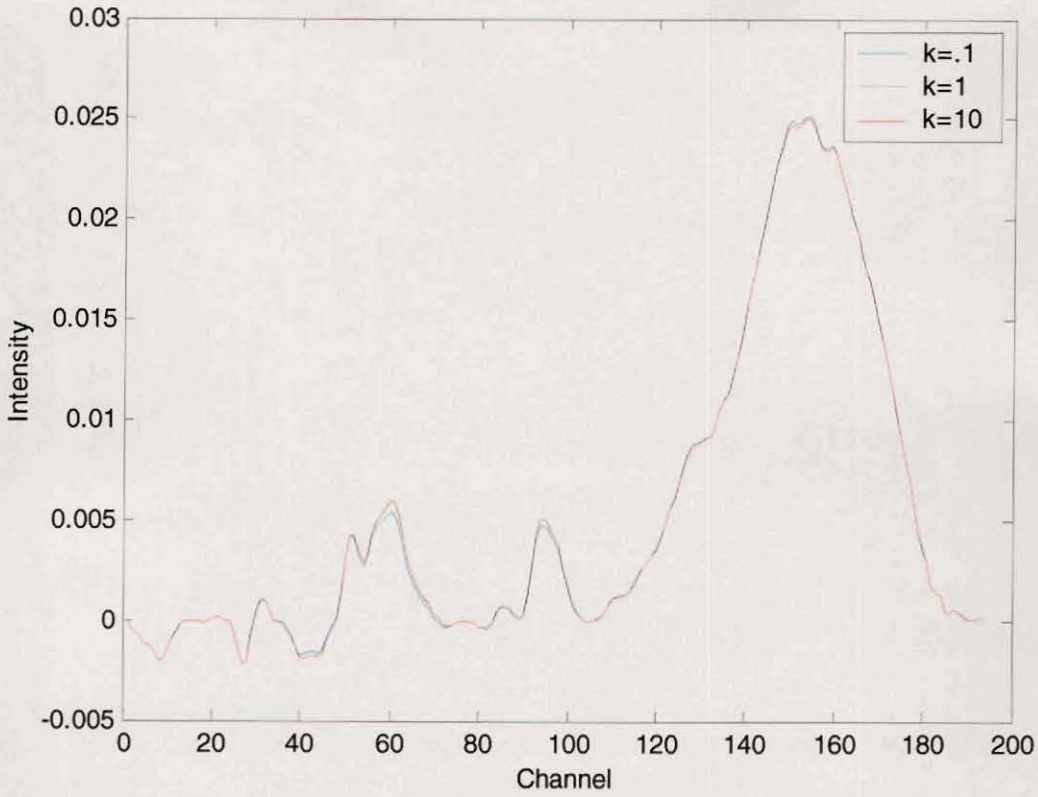

Figure 15 – MLE Estimates of Spectrum of 3rd Component (SIMPLISMA Prior)
$k = .1, 1, 10$

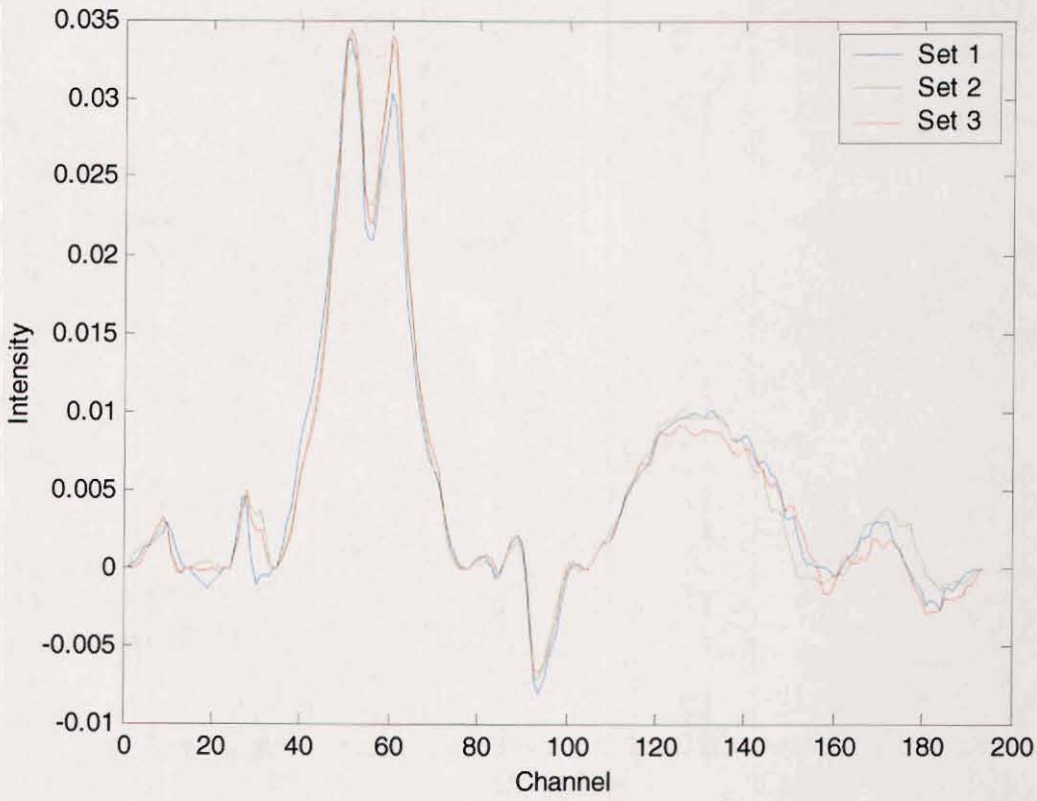

Figure 16 – MLE Estimates of Spectrum of 1st Component (SIMPLISMA Prior)
3 different sets of spectra, k=10

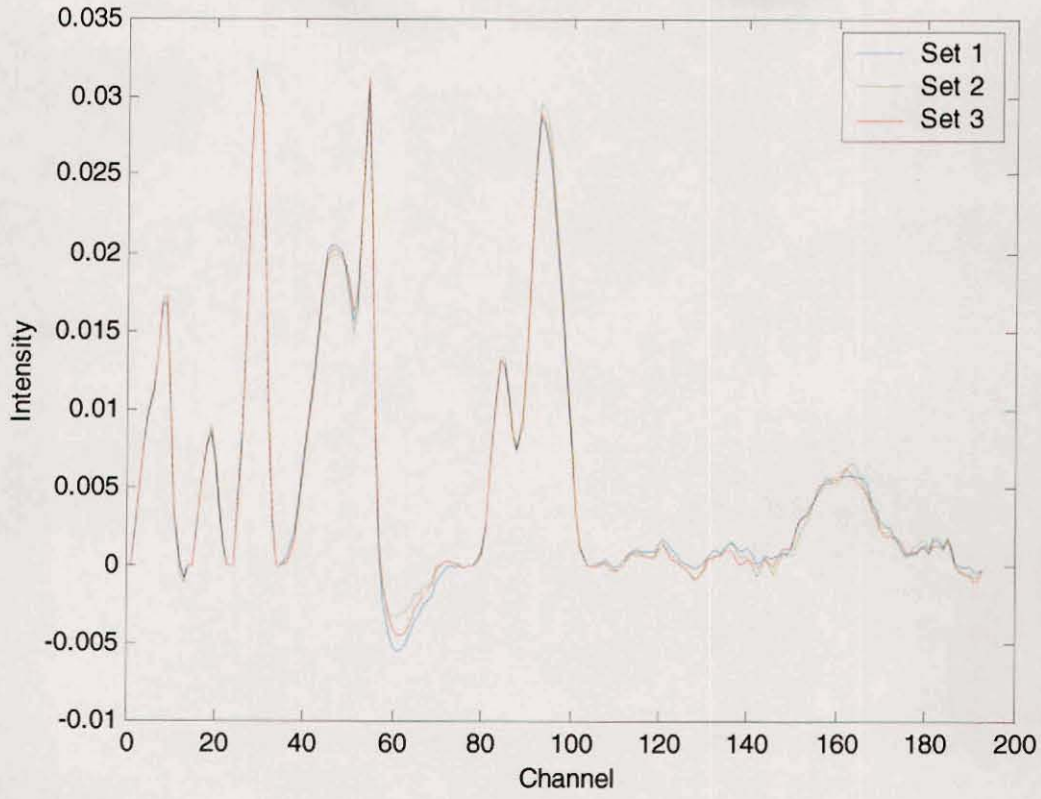

Figure 17 – MLE Estimates of Spectrum of 2nd Component (SIMPLISMA Prior)
3 different sets of spectra, k=10

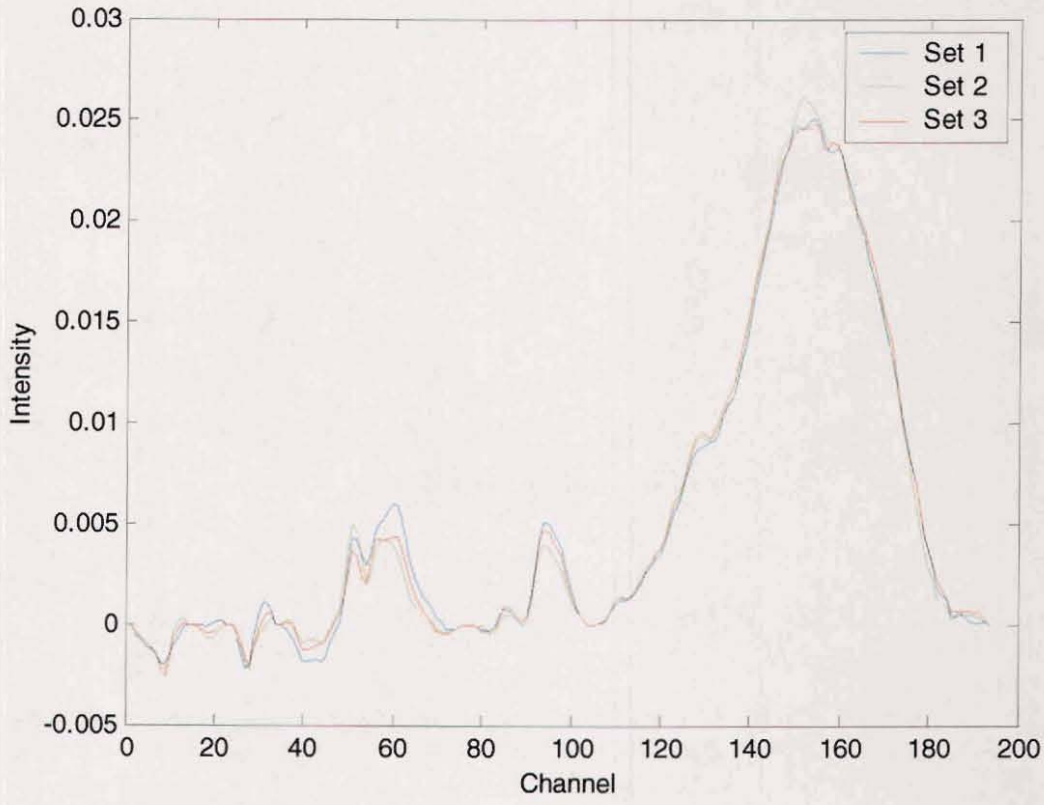

Figure 18 – MLE Estimates of Spectrum of 3rd Component (SIMPLISMA Prior)
3 different sets of spectra, k=10

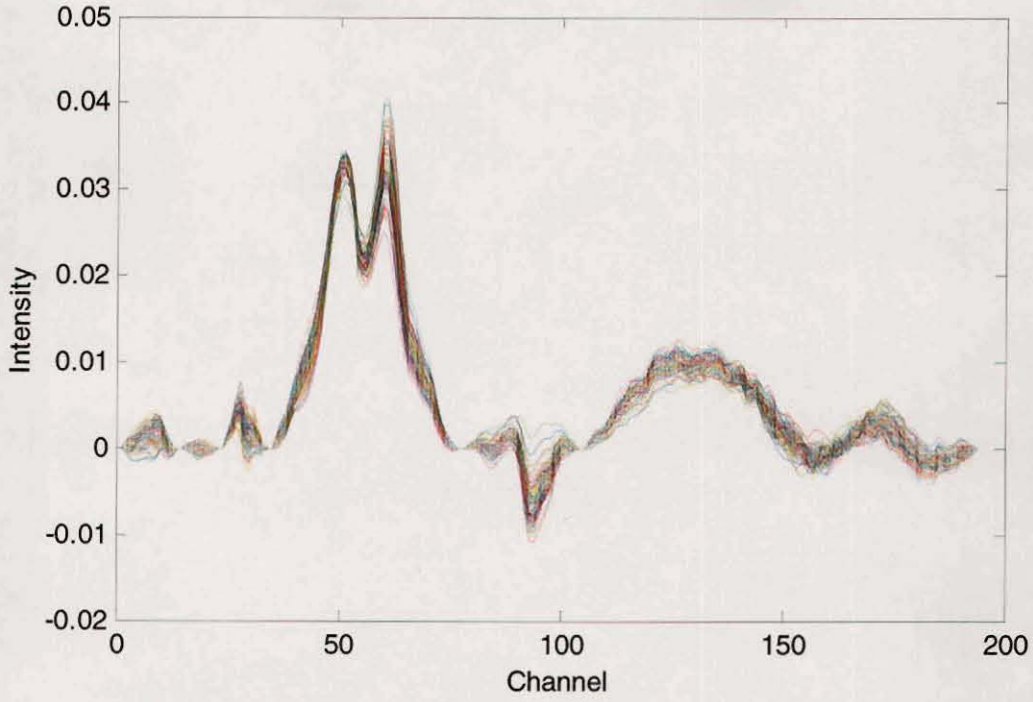

Figure 19 – MLE Estimates of Spectrum of 1st Component
100 different sets of spectra, k=10

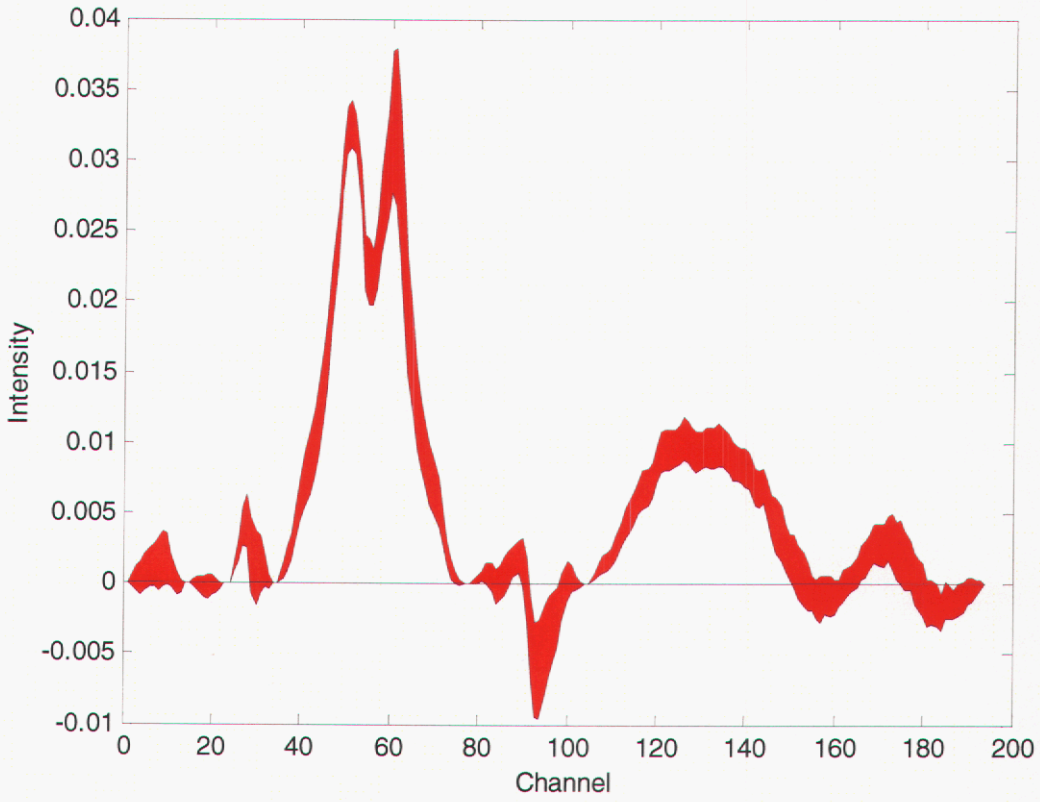

Figure 20 – Approximate 90% Confidence Interval for 1st Component

Appendix 1 – MATLAB SCRIPT for MLE-based Curve Resolution

```
function [conc_profile,newpcs_est]=mle(spectra,pcs_est,err_cov);
%
% Description: Obtain estimates of pure component spectra
%          via maximum likelihood
%
% Input
%    spectra = nxq matrix of spectra
%    pcs_est = pxq matrix of intial estimates of pure component spectra
%    err_cov = (n+p)x(n+p) covariance matrix of errors in [spectra|pcs_est]
%          (to within a scale factor)
% Output
%    conc_profile = nxp matrix of estimated conc associated with spectra
%    newpcs_est = pxq matrix of final estimates of pure component spectra
%
[n,q]=size(spectra);
[p,q]=size(pcs_est);
c=inv(sqrtm(err_cov));
z=[spectra; pcs_est]';
m=z'*z/q;
[ev,dd]=eig(c*m*c);
[lambda,k]=sort(diag(-dd));
g=ev(:,k);
% g contains eigenvectors sorted by associated e-value (small to large)
g2=g(:,(p+1):n+p);
% g2 contains eigenvectors associated with n smallest e-values
d=c*g2;
conc_profile=-d(n+1:n+p,1:n)*inv(d(1:n,1:n));
nw=z*(eye(n+p)-d*d'*err_cov);
newpcs_est=nw(:,n+1:n+p)';
```

APPENDIX D.

APPLICATION OF EQUALITY CONSTRAINTS ON VARIABLES DURING ALTERNATING LEAST SQUARES PROCEDURES

Mark H. Van Benthem, Michael R. Keenan and David M. Haaland

Sandia National Laboratories,
Albuquerque, NM 87185-0886

INTRODUCTION

The technique of alternating least squares (ALS) is frequently used in factor analysis of chemical data. Methods like PARAFAC[1-6] and multivariate curve resolution (MCR)[7-25] seek to identify components of a data set by iteratively obtaining solutions to least squares problems for each set of factors that putatively constitute the data. For example, one may have a data matrix composed of near infrared spectra collected for several mixtures of analytes at varying concentrations. The analytical objective may be to obtain the concentration profiles and spectra of the individual species or components of the mixture. Frequently these methods necessitate the use of constraints to achieve meaningful solutions.

One constraint often applied is nonnegativity,[7-15, 17-21, 23-31] since concentrations and measured spectral signals are positive or zero. Closure,[7, 9, 13, 14, 21, 25, 32, 33] having the sum of concentrations in a mixture equal to some value (often 1), for all solutions in a data set is another common constraint. Zero concentration[8-11, 13, 14] is a constraint that sets the concentration value to zero for species known to be absent in a mixture. Selectivity[13-15, 34] exists when there is a portion of the data that only contains contributions from a single component. In addition, one may find it necessary to apply equality constraints to accommodate a baseline offset, slope or curvature,[35-38] or the spectrum of a species known to be present in the data.[33]

The obvious approach to the equality constraint problem[39] is to estimate the coefficients in a least squares sense followed by substitution of the constrained value into the coefficients. This approach is similar to an oft-used method employed for nonnegativity, where all negative values from a least squares solution are set to zero. Direct substitution of the constraint is convenient and fast, but it fails to obtain a least squares solution to the problem as illustrated by Bro[40] for the nonnegativity constraint. Following Bro's example for nonnegativity, consider the equality constraint example below. The model for an $n \times l$ matrix of independent variables $\mathbf{Z}$, an $n \times 1$ vector of dependent variables $\mathbf{x}$, and an $l \times 1$ vector of unknown coefficients $\mathbf{d}$ is

$$\mathbf{x} = \mathbf{Z}\mathbf{d} \tag{1}$$

where

$$\mathbf{Z} = \begin{bmatrix} 73 & 71 & 52 \\ 87 & 74 & 46 \\ 72 & 2 & 7 \\ 80 & 89 & 71 \end{bmatrix} \quad \text{and} \quad \mathbf{x} = \begin{bmatrix} 49 \\ 67 \\ 68 \\ 20 \end{bmatrix}.$$

The least squares solution to (1) is

$$\mathbf{d} = \begin{bmatrix} 1.123 \\ 0.917 \\ -2.068 \end{bmatrix}.$$

This solution has a root mean square error (RMS), i.e., $\|\mathbf{x} - \mathbf{Zd}\|^2$, of 6. Suppose one knows that the value of the first coefficient in $\mathbf{d}$ is 2. Merely substituting this value in after least squares gives $\mathbf{d} = [2 \quad 0.917 \quad -2.068]^T$ and yields a RMS of 69. However, a true least squares estimate gives $\mathbf{d} = [2 \quad 1.139 \quad -3.606]^T$ and yields a RMS of 31. Just as in the nonnegative case, the solutions are substantially different and improperly derived solutions (by substitution) could cause undesirable behavior in ALS and yield erroneous results. Employing a least squares criterion on solutions in ALS techniques means that subsequent iterations of estimates will always improve (yield smaller RMS) or remain unchanged. This desired least squares behavior is not the case for substitution.

In order to obtain a least squares solution and retain the strength of the bilinear model, it is important to employ a least squares method while applying constraints. Fortunately, Lawson and Hanson[41] describe three techniques for applying equality constraints in least squares problems. Each of the three methods yields an identical least squares solution to the equality-constrained problem, and none is particularly onerous to use; although, one or another may be more advantageous to an individual user. We will briefly review these three techniques and discuss their application and some special cases of their use.

This note explains the theory and implementation of equality constrained least squares and gives a brief MCR example of its use. Notation is typical of this type of work: scalars are lowercase italics, vectors are lowercase bold, matrices are uppercase bold, transpose of vectors and matrices are indicated by a superscript T, *vide supra.*

GENERAL CASE OF EQUALITY CONSTRAINED LEAST SQUARES

Employing the basis vectors of the null space

In the example above, we sought to minimize

$$\|\mathbf{x} - \mathbf{Zd}\|^2$$

subject to the constraint

$$d_1 = 2.$$

We can write a constraint equation, following Lawson and Hanson, as

$$\mathbf{y} = \mathbf{Cd}, \tag{2}$$

where $\mathbf{y}$ is the $m \times 1$ vector of constrained values and $\mathbf{C}$ is the $m \times l$ constraint matrix, whose rank is $k(=m)$. For this example, $\mathbf{y}$ and $\mathbf{C}$ are equal to $[2]$ and $[1 \quad 0 \quad 0]$, respectively. Note that $m < l$, otherwise if $m = l$ the problem would be fully constrained with a trivial solution. The first

method described by Lawson and Hanson uses an orthogonal set of basis vectors that span the null space of the constraint matrix to transform **C** and **Z** to ensure a unique solution to the least squares problem. They recommend using this method if the problem to be solved is underdetermined.

An orthogonal decomposition of **C** can be performed using the familiar SVD. However, it is more computationally convenient to use another orthogonal decomposition of **C** such as the LQ factorization, which is given by

$$\mathbf{C} = \mathbf{L}\mathbf{Q}^{\mathrm{T}}, \tag{3}$$

where **L** is an $m \times m$ lower triangular matrix and **Q** is the $l \times l$ orthonormal basis set matrix.

Let $\tilde{\mathbf{C}}_m$ be the $m \times m$ transformation matrix of **C** that contains the first m columns of **CQ**. And let $\tilde{\mathbf{Z}}$ be the $n \times l$ transformation matrix of **Z**, which is computed from the product of **ZQ**. Then partition $\tilde{\mathbf{Z}}$ into two matrices $\tilde{\mathbf{Z}}_m$ and $\tilde{\mathbf{Z}}_l$, which are matrices composed of the first m columns of $\tilde{\mathbf{Z}}$ and the last $l - m$ columns of $\tilde{\mathbf{Z}}$, respectively. The equality constrained least squares solution for **x** is computed as follows.

Compute the least squares solution for the equation

$$\mathbf{y} = \tilde{\mathbf{C}}_m \tilde{\mathbf{d}}_m \tag{4}$$

for the vector $\hat{\tilde{\mathbf{d}}}_m$. Then use this result to calculate

$$\tilde{\mathbf{x}} = \mathbf{x} - \tilde{\mathbf{Z}}_m \hat{\tilde{\mathbf{d}}}_m, \tag{5}$$

and solve the least squares solution to

$$\tilde{\mathbf{x}} = \tilde{\mathbf{Z}}_l \tilde{\mathbf{d}}_l, \tag{6}$$

for the vector $\hat{\tilde{\mathbf{d}}}_l$. The solution for **d** is then accomplished by transformation of the augmented vector $\hat{\tilde{\mathbf{d}}} = \begin{bmatrix} \hat{\tilde{\mathbf{d}}}_m \\ \hat{\tilde{\mathbf{d}}}_l \end{bmatrix}$

$$\hat{\mathbf{d}} = \mathbf{Q}\hat{\tilde{\mathbf{d}}} \tag{7}$$

Direct elimination

The second method used by Lawson and Hanson is the method of direct elimination. Here like the null space method, the solution vector is obtained piecewise, however, orthogonal transformation is not necessary.

Let $\mathbf{C}_m$ be the $m \times m$ partition matrix that contains the first m linearly independent columns of **C** and let $\mathbf{C}_l$ be the $m \times l$ partition matrix that contains the last $l - m$ columns of **C**. Likewise, let

$\mathbf{d}_m$ and $\mathbf{d}_l$ be the conformable partitions of $\mathbf{d}$. We can separate Equation 2 and rewrite it as $\mathbf{y} = \mathbf{C}_m\mathbf{d}_m + \mathbf{C}_l\mathbf{d}_l$, and rearrange it as

$$\mathbf{d}_m = \mathbf{C}_m^{-1}(\mathbf{y} - \mathbf{C}_l\mathbf{d}_l). \tag{8}$$

Similarly partitioning $\mathbf{Z}$ and rewriting Equation 1 yields

$$\mathbf{x} = \mathbf{Z}_m\mathbf{d}_m + \mathbf{Z}_l\mathbf{d}_l. \tag{9}$$

Substituting Equation 8 into Equation 9 and rearranging gives

$$\mathbf{x} - \mathbf{Z}_m\mathbf{C}_m^{-1}\mathbf{y} = (\mathbf{Z}_l - \mathbf{Z}_m\mathbf{C}_m^{-1}\mathbf{C}_l)\mathbf{d}_l. \tag{10}$$

We can now define

$$\overline{\mathbf{Z}}_l = \mathbf{Z}_l - \mathbf{Z}_m\mathbf{C}_m^{-1}\mathbf{C}_l \tag{11}$$

and

$$\overline{\mathbf{x}} = \mathbf{x} - \mathbf{Z}_m\mathbf{C}_m^{-1}\mathbf{y}. \tag{12}$$

Now Equation 10 can be rewritten as a least squares problem for $\mathbf{d}_l$

$$\overline{\mathbf{x}} = \overline{\mathbf{Z}}_l\mathbf{d}_l. \tag{13}$$

After solving Equation 13, one can then solve Equation 8 for $\mathbf{d}_m$.

Weighting

The final method for applying equality constraints described by Lawson and Hanson is weighting. Here the augmented vector containing $\mathbf{y}$ and a heavily down weighted $\mathbf{x}$ is projected into the space of the augmented matrix containing $\mathbf{C}$ and an identically down weighted $\mathbf{Z}$. The model is written as

$$\begin{bmatrix} \mathbf{C} \\ \varepsilon\mathbf{E} \end{bmatrix}\mathbf{d} = \begin{bmatrix} \mathbf{y} \\ \varepsilon\mathbf{x} \end{bmatrix}$$

where ε is the weighting factor. Two important issues that must be addressed with this technique are how small to make ε and the method of solving the least squares problem above. First, ε must be small enough to ensure that the equality condition is met, but not so small that it is effectively zero in terms of computer precision. Second, because ε is very small this will lead to a poorly conditioned matrix in $\mathbf{C}$ and $\mathbf{E}$, so inversion will probably be inaccurate. These issues are fairly easy to deal with and make this method appealing for most ALS problems.

The choice of ε is based upon the machine precision and the magnitude of the data.[42] Hanson and Haskell suggest the following for the value of ε.

$$\varepsilon = \sqrt{\frac{10^{-4}\eta}{\gamma}}$$

Where η is the relative machine precision and γ is the infinity norm of the augmented matrix in **C** and **E**, which is the largest row sum in that matrix. Inversion of the poorly conditioned augmented and weighted matrix can be accomplished using an orthogonal factorization method to obtain a stable solution.

Using the weighting method allows a quick, direct computation of **d** without having to partition the matrices and vectors.

All three of these methods can be used for the variety of equality constraints found in ALS routines. These equality constraints include fixed values as demonstrated in our example, zero concentrations, and closure. The closure constraint application is exemplified in the appendix of this paper.

SPECIAL CASES OF EQUALITY CONSTRAINED LEAST SQUARES

Known concentration or spectral intensity

When one is faced with a known concentration (e.g., zero concentration) or spectral intensity (e.g., baseline offset and slope or a known spectral pure component present in the data) the equality constraint problem becomes identical to our example above with the exception that it represents a multivariate constraint. In this special case, the method of the basis of the null space and the method of direct elimination become identical. To illustrate the steps in the solutions to this problem, we will use the example presented earlier.

The first step in the null space basis method is to decompose the constraint matrix to obtain the orthonormal basis matrix, **Q**, in Equation 3. The resulting **Q** matrix in the case of our equality constraint **C** is the identity matrix

$$\mathbf{C} = \begin{bmatrix} 1 & 0 & 0 \end{bmatrix} = \mathbf{LQ} = \begin{bmatrix} 1 & 0 & 0 \end{bmatrix} \begin{bmatrix} 1 & 0 & 0 \\ 0 & 1 & 0 \\ 0 & 0 & 1 \end{bmatrix}$$

This formulation of the problem makes the remaining computations in the method trivial since the transformations are identity, hence $\tilde{\mathbf{C}} = \mathbf{C}$ and $\tilde{\mathbf{Z}} = \mathbf{Z}$. We can now write our partitioned *transformed* matrices

$$\tilde{\mathbf{C}}_m = [1], \quad \tilde{\mathbf{Z}}_m = \begin{bmatrix} 73 \\ 87 \\ 72 \\ 80 \end{bmatrix}, \text{ and, } \quad \tilde{\mathbf{Z}}_l = \begin{bmatrix} 71 & 52 \\ 74 & 46 \\ 2 & 7 \\ 89 & 71 \end{bmatrix}$$

and commence with our computations. Since the solution for Equation 4 is trivial, we now solve for Equation 5.

$$\tilde{\mathbf{x}} = \mathbf{x} - \mathbf{Z}_m \hat{\tilde{\mathbf{d}}} = \begin{bmatrix} 49 \\ 67 \\ 68 \\ 20 \end{bmatrix} - \begin{bmatrix} 73 \\ 87 \\ 72 \\ 80 \end{bmatrix} [2] = \begin{bmatrix} -97 \\ -107 \\ -76 \\ -140 \end{bmatrix}$$

Now we solve the least squares problem in Equation 6, which yields $\hat{\tilde{\mathbf{d}}}_l = [1.139 \quad -3.606]^T$ and finally, $\hat{\tilde{\mathbf{d}}} = [2 \quad 1.139 \quad -3.606]^T$. Again, the transformation in Equation 7 is trivial, and we have our result.

For this special case, the method of direct elimination reduces to an identical set of equations as the null space method because $\mathbf{C}_l$ is a zero matrix. Specifically, Equations 4 and 8 are identical, Equation 10 reduces to Equation 5, and Equation 6 and 13 are the only least squares problems that must be solved. In effect, one simply subtracts the product of the constrained components, whose coefficients are contained in $\mathbf{Z}_m$ and $\mathbf{y}$, from the data in $\mathbf{x}$ prior to the least squares step. These least squares equality constraint methods are simple to employ and actually reduce the time required for computation over the commonly used method of substitution. Here the least squares problem to be solved is smaller in rank by the number of constraints than the full rank problem one would solve using the substitution method. This is, in fact, the method that Gampp[33] employs in dealing with known spectral components for rank annihilation by evolving factor analysis. A graphical depiction of this method is presented in Figure 1.

In the event one also wants to apply nonnegativity constraints to the part of the solution that is not equality constrained, one simply applies the nonnegative least squares algorithm to solve Equation 13. This method should be used with caution since the nonnegative solution will apply only to the last l - m variables in $\mathbf{d}$ that are determined in Equation 13. Attempting to apply this method for closure constraints while simultaneously seeking a nonnegative solution is improper. See the Appendix on closure constraints for example.

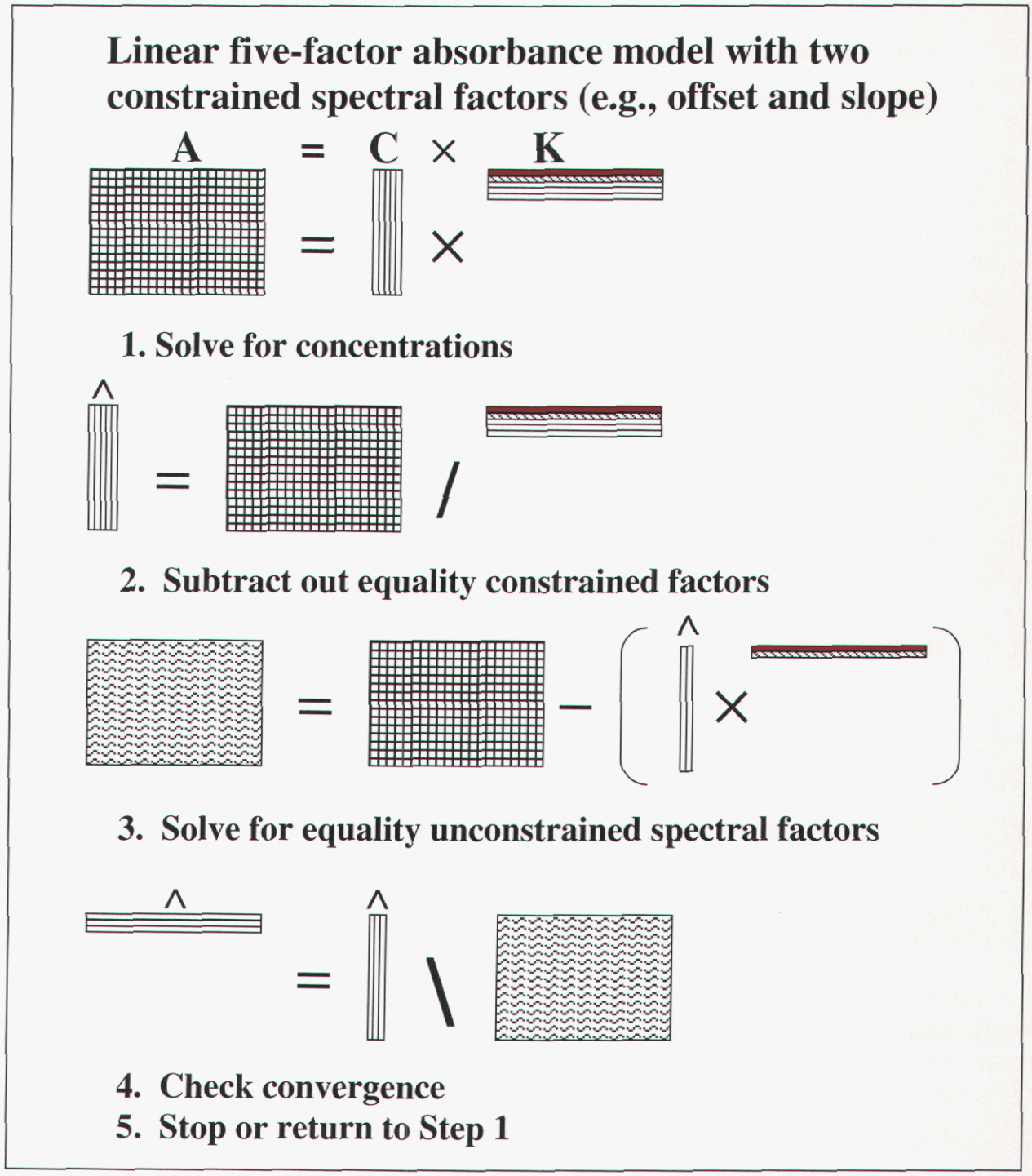

Figure 1. Application of direct elimination for equality constraints during ALS. Depicted here are two equality constrained spectral components represented by the dark ▬ and the hashed ▭ blocks. The '/' represents right matrix division and the '\' is left matrix division.

The closure constraint.

The closure constraint most frequently used is that for sum-to-one concentration. An example may be a set of mixtures containing several component species prepared by adding varying volumes of each component to fill a fixed volume. Of course, in order for the closure constraint to be unity, the behavior of the mixtures should approach ideality so the free energy of mixing

and the change in volume are both very small. In addition, for closure to exist in the case of spectral data, all species must be spectrally active in the spectral region analyzed. Consider our initial example for the closure constraint where the sum of the elements of **d** is one. Thus, the components of constraint equation are

$$\mathbf{C} = [1 \quad 1 \quad 1] \text{ and } \mathbf{y} = [1].$$

Equations 11 and 12 produce $\overline{\mathbf{Z}}_l$

$$\overline{\mathbf{Z}}_l = \mathbf{Z}_l - \mathbf{Z}_m \mathbf{C}_m^{-1} \mathbf{C}_l = \begin{bmatrix} 71 & 52 \\ 74 & 46 \\ 2 & 7 \\ 89 & 71 \end{bmatrix} - \begin{bmatrix} 73 \\ 87 \\ 72 \\ 80 \end{bmatrix} [1]^{-1} [1 \quad 1] = \begin{bmatrix} -2 & -212 \\ -13 & -41 \\ -70 & -65 \\ 9 & -9 \end{bmatrix}$$

and $\overline{\mathbf{x}}$

$$\overline{\mathbf{x}} = \mathbf{x} - \mathbf{Z}_m \mathbf{C}_m^{-1} \mathbf{y} = \begin{bmatrix} 49 \\ 67 \\ 68 \\ 20 \end{bmatrix} - \begin{bmatrix} 73 \\ 87 \\ 72 \\ 80 \end{bmatrix} [1]^{-1} [1] = \begin{bmatrix} -24 \\ -20 \\ -4 \\ -60 \end{bmatrix}.$$

Now Equation 13 yields

$$\mathbf{d}_l = \overline{\mathbf{Z}}_l^{+} \overline{\mathbf{x}} = \begin{bmatrix} -1.353 \\ 1.392 \end{bmatrix}$$

where $\overline{\mathbf{Z}}_l^{+}$ is the generalized inverse of $\overline{\mathbf{Z}}_l$. Finally, Equation 8 gives

$$\mathbf{d}_m = \mathbf{C}_m^{-1}(\mathbf{y} - \mathbf{C}_l \mathbf{d}_l) = [1]^{-1} \left([1] - [1 \quad 1] \begin{bmatrix} -1.353 \\ 1.392 \end{bmatrix} \right) = [0.961]$$

and $\mathbf{d} = [0.961 \quad -1.353 \quad 1.392]^{\mathrm{T}}$ whose column sum is 1, q.e.d. This is a substantially different result than one would get by normalizing to unit sum the unconstrained least-squares result.

One drawback of the direct elimination method for the closure constraint is that one cannot simply enforce a nonnegativity constraint on the solution *for all variables* using nonnegative least squares. One can use the nonnegative least-squares algorithm to solve Equation 13 and enforce nonnegativity on the l - m variables, but his does not guarantee that the first m variables will be nonnegativity. Instead, one must use an inequality condition that states that the l - m variables are nonnegative *and* that their sum is less than the closure condition. These conditions ensure that the solution to Equation 8 is greater than or equal to zero. A more flexible tool for obtaining the closure constraint (and other equality constraints) is to use weighted nonnegative least squares, WNNLS.[42, 43]

DEMONSTRATION ON SIMULATED DATA

The method of direct elimination for applying equality constraints to variables was compared to the more intuitive but flawed method of substitution. Three spectral pure components were generated using combinations of Gaussian-shaped curves (Figure 2). Each pure spectrum was

normalized to unit-vector length. A corresponding set of 600 pure component concentrations was generated from a uniform distribution of random numbers. The cross product of the random concentrations and the pure spectral components produce the 600 spectra used in the simulation. Random positive amounts of offset and random positive amounts of a sloping baseline were separately added to each spectrum. The sloping baseline was a unit length vector with positive and negative endpoints having identical absolute values and a zero midpoint. Three percent noise, based upon the maximum signal intensity of all samples, was added to each spectrum in the form of normally distributed homoscedastic errors.

The data were analyzed and the results compared using the rigorous method of applying equality constraints and the commonly applied method of substitution using code written by the authors. All processing and analysis was performed on Matlab® version 6.0 (The Mathworks, Natick MA).

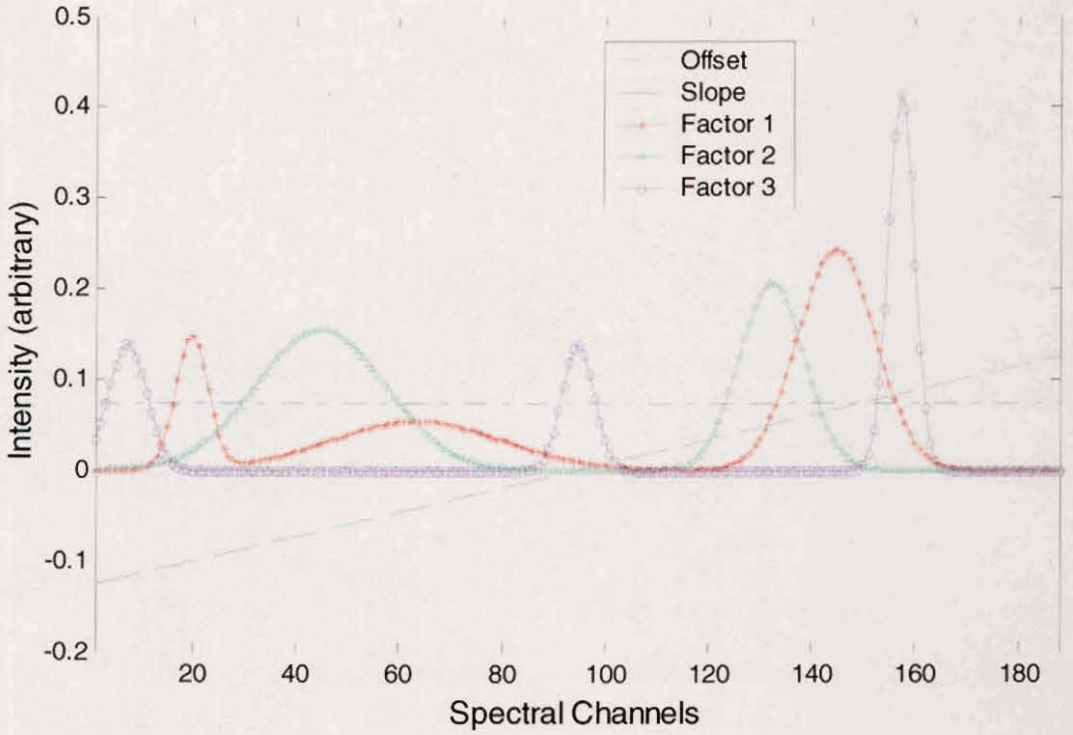

Figure 2. Pure spectral components with offset and slope used in simulation.

Starting points for MCR were chosen as three random vectors and an offset and a slope. We generated three spectral vectors using the Matlab® "rand" function, which produces elements of a vector chosen from a uniform distribution with values between zero and one. These vectors were normalized to unit length prior to analysis. Additionally, their corresponding spectral-mode solutions were normalized after each ALS iteration. The offset and slope were identical to those in the data described above. Equality constraints were applied to the offset and slope. The rigorous constrained least squares method we chose to apply was the method of direct elimination. Nonnegativity constraints were rigorously applied to the least squares solutions of the three spectral vectors, to their corresponding concentrations and to the magnitudes of the offset and slope. MCR was computed for 500 iterations.

The spectral component results for the rigorous method and substitution method are shown in Figure 3 and Figure 4, respectively.

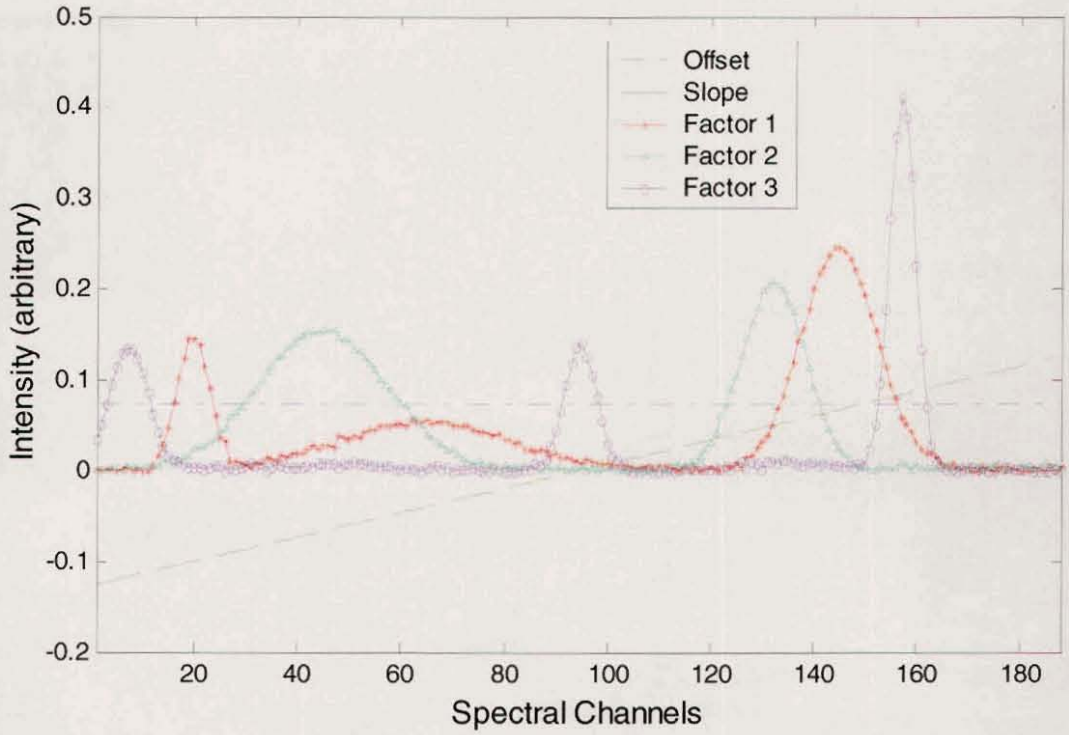

Figure 3. MCR-resolved spectral components for rigorously applied equality constraints. Broken lines are offset and slope, which were fixed throughout MCR.

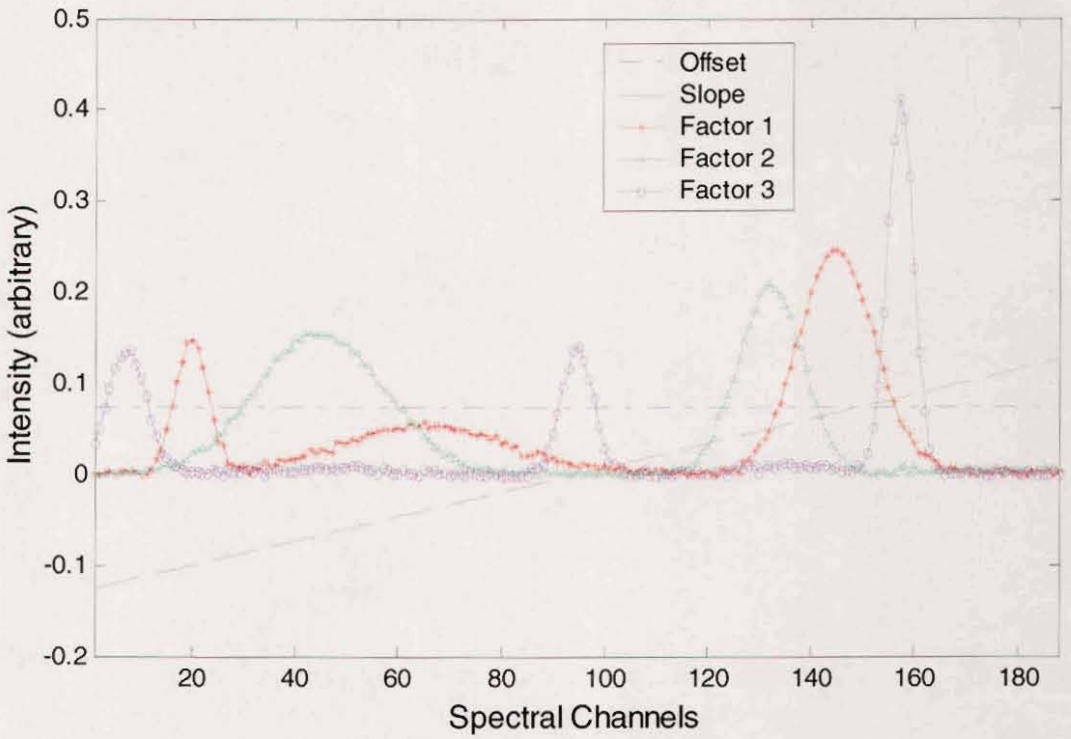

Figure 4. MCR-resolved spectral components for equality constraints applied by substitution. Broken lines are offset and slope, which were fixed throughout MCR.

The results for the spectral components from the two methods were very similar and matched well with the input pure components. Likewise, the concentrations for each were very similar and well matched. However, the RMS curves in Figure 5, in which RMS was determined after each iteration, provided a more telling result.

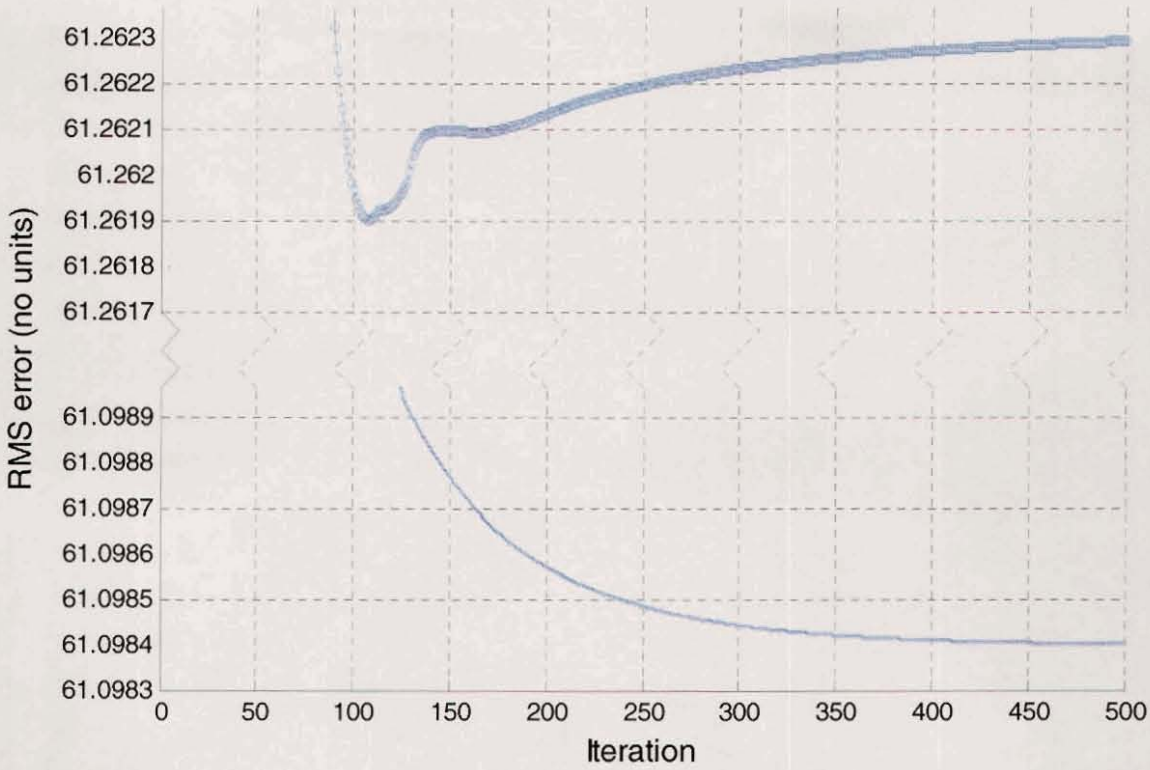

Figure 5. RMS for MCR using substitution method (top) and new method (bottom) of equality constraint. Note that ordinate is broken to expand scale.

Note first the RMS for the method of direct elimination for applying equality constraints on the bottom of Figure 5. The RMS curve displays the monotonically decreasing behavior one expects from the ALS procedure. This behavior was observed for all 500 iterations performed; indeed this behavior was found in all other simulations that we performed, even out to thousands of iterations. Conversely, the substitution method displayed on the top of Figure 5 does not exhibit a well-behaved least squares behavior. Unfortunately the RMS values from the substitution method reach a minimum and then increases briefly before finding another minimum and then increase for the remainder of the 500 iterations. This behavior in RMS error causes several problems. One must now choose which set of coefficients to use: the minimum in RMS or the last iteration. Also, one must wonder in what direction the minimization was proceeding at each iteration. Finally, the minimum for the substitution method does not indicate as good a fit to the data as the new method described here. Clearly, substitution is not the optimal way to obtain a least squares solution when applying equality constraints to variables.

CONCLUSION

We have presented mathematically correct ways of equality constraining or fixing variables during least squares procedures. Using simulated data, we have compared one of these methods to the simple and intuitive, but flawed technique of substitution that is commonly used today. The rigorous methods are easily implemented in ALS routines and have been demonstrated to provide lower RMS results with faster convergence. Therefore, we recommend the use of these true least squares methods of applying equality constraints to multivariate curve resolution problems.

ACKNOWLEDGEMENTS

This work was supported by Sandia National Laboratories and the Department of Energy. Sandia is a multi-program laboratory operated by Sandia Corporation, a Lockheed Martin Company, for the United States Department of Energy under Contract DE-ACO4-94AL85000.

APPENDIX

The closure constraint in ALS

The method of enforcing the closure constraint commonly used in ALS is that of normalization. In ALS one solves by the method of least squares for one set of factors, then uses that result to solve for the other set of factors. So, an $n \times p$ matrix of absorbance spectra, $\mathbf{X}$, composed of l factors, would be modeled by an $n \times l$ concentration matrix $\mathbf{Z}$ and an $l \times p$ pure-component spectra matrix $\mathbf{D}$. The sequence would proceed as follows:

The model is,

$$\mathbf{X} = \mathbf{ZD}.$$

Starting with initial guess for spectra (arbitrarily), one solves for concentrations

Step 1 $$\hat{\mathbf{Z}} = \mathbf{X}\mathbf{D}^{\mathrm{T}}\left(\mathbf{D}\mathbf{D}^{\mathrm{T}}\right)^{-1}$$

and then uses that result to solve for pure component spectra

Step 2 $$\hat{\mathbf{D}} = \left(\hat{\mathbf{Z}}^{\mathrm{T}}\hat{\mathbf{Z}}\right)^{-1}\hat{\mathbf{Z}}^{\mathrm{T}}\mathbf{X}.$$

Step 3 Check convergence, i.e., $\left\|\mathbf{X} - \mathbf{ZD}\right\|^2$

Step 4 Return to Step 1 *or* Stop if convergence obtained.

Closure is commonly accomplished by normalizing the rows of the concentration matrix to unit sum after Step 1. This is equivalent to left-multiplying the concentration matrix by a diagonal normalization matrix S, whose elements are the reciprocals of the row sums, thus

Step 1a $$\dot{\hat{\mathbf{Z}}} = \mathbf{S}\hat{\mathbf{Z}}$$

Here one has met the constraint for closure to unit concentration. However, if one now continues into Step 2 and solves for $\hat{\mathbf{D}}$, the least squares solution obtained in Step 1 is lost unless the data in $\mathbf{X}$ are also left-multiplied by $\mathbf{S}$, specifically,

Step 1b $$\dot{\mathbf{X}} = \mathbf{SX}$$

Finally, Step 2 is slightly modified for the correct solution for $\hat{\mathbf{D}}$.

Step 2 $$\hat{\mathbf{D}} = \left(\dot{\hat{\mathbf{Z}}}^{\mathrm{T}}\dot{\hat{\mathbf{Z}}}\right)^{-1}\dot{\hat{\mathbf{Z}}}^{\mathrm{T}}\dot{\mathbf{X}}$$

REFERENCES

1. Harshman, R. A., *UCLA Working Papers Phonetics*, **16** (1970) 1–84.

2. Kruskal, J. B., Harshman, R. A. and Lundy, M. E., In *Multiway Data Analysis*, ed. R. Coppi and S. Bolasco. North-Holland, Amsterdam, 1989, pp. 115-122.

3. Mitchell, B. C. and Burdick, D. S., *J. Chemom.*, **8** (1994) 155-168.

4. Hopke, P. K., Paatero, P., Jia, H., Ross, R. T. and Harshman, R. A., *Chemometrics Intell. Lab. Syst.*, **43** (1998) 25-42.

5. Kiers, H. A. L., TenBerge, J. M. F. and Bro, R., *J. Chemometrics*, **13** (1999) 275-294.

6. Bro, R., *Chemometrics Intell. Lab. Syst.*, **38** (1997) 149-171.

7. Tauler, R., Casassas, E. and Izquierdo-Ridorsa, A., *Anal. Chim. Acta*, **248** (1991) 447-458.

8. Tauler, R., Kowalski, B. and Fleming, S., *Anal. Chem.*, **65** (1993) 2040-2047.

9. Tauler, R., Izquierdo-Ridorsa, A. and Casassas, E., *Chemometrics Intell. Lab. Syst.*, **18** (1993) 293-300.

10. Tauler, R. and Barcelo, D., *Trends Anal. Chem.*, **12** (1993) 319-327.

11. Tauler, R., Smilde, A. K., Henshaw, J. M., Burgess, L. W. and Kowalski, B. R., *Anal. Chem.*, **66** (1994) 3337-3344.

12. Casassas, E., Marques, I. and Tauler, R., *Anal. Chim. Acta*, **310** (1995) 473-484.

13. Tauler, R., *Chemometrics Intell. Lab. Syst.*, **30** (1995) 133-146.

14. Tauler, R., Smilde, A. and Kowalski, B., *J. Chemometrics*, **9** (1995) 31-58.

15. Tauler, R., Lacorte, S. and Barcelo, D., *J. Chromatogr. A*, **730** (1996) 177-183.

16. deJuan, A., VanderHeyden, Y., Tauler, R. and Massart, D. L., *Anal. Chim. Acta*, **346** (1997) 307-318.

17. Andrew, J. J. and Hancewicz, T. M., *Applied Spectroscopy*, **52** (1998) 797-807.

18. Bro, R. and Sidiropoulos, N. D., *J. Chemometrics*, **12** (1998) 223-247.

19. Salau, J. S., Honing, M., Tauler, R. and Barcelo, D., *J. Chromatogr. A*, **795** (1998) 3-12.

20. DiazCruz, M. S., Mendieta, J., Tauler, R. and Esteban, M., *Analytical Chemistry*, **71** (1999) 4629-4636.

21. Vives, M., Gargallo, R. and Tauler, R., *Analytical Chemistry*, **71** (1999) 4328-4337.

22. Budevska, B. O., *Vibrational Spectroscopy*, **24** (2000) 37-45.

23. Cruz, B. H., DiazCruz, J. M., Arino, C., Tauler, R. and Esteban, M., *Anal. Chim. Acta*, **424** (2000) 203-209.

24. Saurina, J., Leal, C., Compano, R., Granados, M., Tauler, R. and Prat, M. D., *Anal. Chim. Acta*, **409** (2000) 237-245.

25. Vives, M., Gargallo, R. and Tauler, R., *Analytical Biochemistry*, **291** (2001) 1-10.

26. Lawton, W. H. and Sylvestre, E. A., *Technometrics*, **13** (1971) 617-633.

27. Borgen, O. S. and Kowalski, B. R., *Anal. Chim. Acta*, **174** (1985) 1-26.

28. Vandeginste, B. G. M., Derks, W. and Kateman, G., *Anal. Chim. Acta*, **173** (1985) 253-264.

29. Windig, W. and Guilment, J., *Analytical Chemistry*, **63** (1991) 1425-1432.

30. Tauler, R. and Casassas, E., *Anal. Chim. Acta*, **223** (1989) 257-268.

31. Spjotvoll, E., Martens, H. and Volden, R., *Technometrics*, **24** (1982) 173-180.

32. Gampp, H., Maeder, M., Meyer, C. J. and Zuberbuhler, A. D., *Talanta*, **32** (1985) 1133-1139.

33. Gampp, H., Maeder, M., Meyer, C. J. and Zuberbuehler, A. D., *Anal. Chim. Acta*, **193** (1987) 287-293.

34. Bro, R., Dissertation, University of Amsterdam, 1998.

35. Haaland, D. M. and Easterling, R. G., *Applied Spectroscopy*, **34** (1980) 539-548.

36. Haaland, D. M. and Easterling, R. G., *Applied Spectroscopy*, **36** (1982) 665-673.

37. Haaland, D. M., Easterling, R. G. and Vopicka, D. A., *Applied Spectroscopy*, **39** (1985) 73-84.

38. Salomaa, I. K. and Kauppinen, J. K., *Applied Spectroscopy*, **52** (1998) 579-586.

39. *PLS Toolbox Ver. 2.0*, Eigenvector Research, Inc., Manson, WA, 1998.

40. Bro, R. and DeJong, S., *J. Chemometrics*, **11** (1997) 393-401.

41. Lawson, C. L. and Hanson, R. J. *Solving Least Squares Problems*. Prentice-Hall, Inc., Englewood Cliffs, NJ, 1974.

42. Hanson, R. J. and Haskell, K. H., *ACM Trans. Math. Softw.*, **8** (1982) 323-333.

43. Haskell, K. H. and Hanson, R. J., *Mathematical Programming*, **21** (1981) 98-118.

DISTRIBUTION:

1 Dr. Mathias Celina
Queensland University of Technology
Faculty of Science
School of Physical Science
Brisbane, Australia

1 Fredrick W. Koehler IV
Spectral Dimensions, Inc.
3416 Olandwood Court
Suite 210
Olney, MD 20832

1	MS-0188	Donna L. Chavez	1030
1	MS-0829	Edward V. Thomas	12323
1	MS-0885	Duane Dimos	1802
1	MS-0886	Nancy B. Jackson	1812
1	MS-0886	Christine M. Wehlburg	1812
1	MS-0886	Laura E. Martin	1812
1	MS-0886	Mark H. Van Benthem	1812
1	MS-0886	Michael R. Keenan	1812
1	MS-0889	David K. Melgaard	1835
4	MS-0886	David M. Haaland	1812
1	MS-9018	Central Technical Files	8945-1
2	MS-0899	Technical Library	9616
1	MS-0612	Review & Approval Desk For DOE/OSTI	9612
1	MS-0161	Patent and Licensing Office	11500